DEVELOPMENT OF PHASE RETRIEVAL TECHNIQUES IN DISPLACEMENT AND DISPLACEMENT DERIVATIVES MEASUREMENT

DEEPAN BALAKRISHNAN

(B. Eng. Mechanical Engineering, Anna University Chennai, India)

A THESIS SUBMITTED

FOR THE DEGREE OF DOCTOR OF PHILOSOPHY
DEPARTMENT OF MECHANICAL ENGINEERING
NATIONAL UNIVERSITY OF SINGAPORE

2016

DECLARATION

I hereby declare that this thesis is my original work and it has been written by me in its entirety. I have duly acknowledged all the sources of information which have been used in the thesis.

This thesis has also not been submitted for any degree in any university previously.

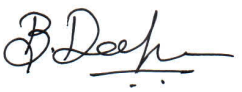

Deepan Balakrishnan
06 December 2016

ACKNOWLEDGEMENTS

I would like to express heartfelt gratitude to my supervisors **Assoc. Prof. Quan Chenggen** and **Assoc. Prof. Tay Cho Jui** for their support and guidance throughout my research. It is their constant encouragement and advice that enable me to complete this work.

Special thanks to Dr. Chen Wen, for his valuable advices and all staff members (Mr. Chiam Tow Jong, Mr. Low Chee Wah, Mr. Goh Tiong Lai and Mr. Abdul Malik) of the Experimental Mechanics, Impact Mechanics and Solid Mechanics Laboratory for their help and support.

In addition, I would like to thank Ms. Sravya Tekumalla (PhD Candidate), for providing material specimens and conducting experimental validations on the specimens.

I thank all my friends for their countless hours of fun and entertainment, which made my life during PhD more lively.

Finally, I thank my family for their understanding, tolerance and love.

TABLE OF CONTENTS

SUMMARY

This thesis proposes several novel techniques for full-field displacement and displacement derivatives measurement in both static and dynamic applications. A Teager-operator based algorithm is proposed to obtain high-quality higher-order unwrapped phase derivative maps from a complex exponential signal, which is obtained from a numerical reconstruction in digital holographic interferometry (DHI). An algorithm is further developed to extend the phase derivatives determination method in digital speckle pattern interferometry (DSPI) and digital speckle shearing interferometry (DSSI). This algorithm employs Huang filtering and Hilbert transform along with Teager operator to obtain complex field from a single fringe pattern.

In addition, a novel fringe analysis technique, which uses fringe orientation and fringe density map, is proposed to obtain phase derivatives directly from a single fringe pattern. Further, a derivative based simplified phase tracker model is proposed for phase demodulation from a single fringe pattern. The phase tracker utilizes predetermined phase gradients to overcome the limitations of existing phase tracker techniques.

In time-average speckle interferometry, a novel amplitude varied refreshing reference frame technique is proposed to improve the contrast and visibility of a Bessel fringe pattern without the need for a phase shifting process. A mathematical model for the fringes obtained from the technique is derived. Subsequently, the derivative based phase tracker model is modified to measure vibrational amplitude from a single fringe pattern. The proposed quantitative vibrational analysis method is useful for both mode shape visualization and vibrational amplitude measurement.

A novel ensemble of hybrid genetic algorithm for two-dimensional phase unwrapping method, is also proposed for phase unwrapping of a noisy phase map. The method performs better than the existing artificial intelligence based phase unwrapping techniques. A method to determine material properties of a small cantilever beam using DSPI is also developed which overcomes the influence of rigid body movement in the out of plane displacement measurement. All methods are verified with numerical simulations and validated by experiments.

A list of publications arising from this research project is shown in Appendix.

LIST OF TABLES

LIST OF FIGURES

LIST OF SYMBOLS

E	Electric field strength in the light wave propagation in vacuum and Young's modulus of a material
∇^2	Laplace operator
c	Speed of light wave in vacuum
t	Temporal coordinate and thickness of a circular disc
x	Spatial coordinate in horizontal direction
y	Spatial coordinate in vertical direction
z	Spatial coordinate in out of plane direction
A_w	Real amplitude of the light wave
f	Frequency of the light wave
$\vec{k}$	Wave vector
$\vec{r}$	Spatial vector
φ	Phase of the light wave
φ_0	Initial constant phase
j	$\sqrt{-1}$
a_o	Amplitude of object wave
a_r	Amplitude of reference wave
φ_o	Phase of object wave
φ_r	Phase of reference wave
I_o	Intensity of the recorded hologram
m	Pixel coordinate in x direction
n	Pixel coordinate in y direction
A_0	Real amplitude of a hologram
I_1	Intensity of a hologram recorded before deformation
I_2	Intensity of a hologram recorded after deformation

φ_1	Phase of a hologram recorded before deformation
φ_2	Phase of a hologram recorded after deformation
I_d	Intensity of a double exposure holographic interferometer
χ	Complex amplitude of a reconstructed hologram
H	Real amplitude of a hologram interference pattern
R	Reference light wave
λ	Wavelength of the light source
u	Horizontal spatial frequency coordinate and surface displacement in x direction
v	Vertical spatial frequency coordinate and surface displacement in y direction
I_h	Intensity of reconstructed hologram
ρ	The recording distance between two points
d	The axial recording distance
M	Pixel number along x direction in the CCD plane
N	Pixel number along y direction in the CCD plane and Number of fringes inside a window
Δu	Pixel size along x direction in the CCD plane
Δv	Pixel size along y direction in the CCD plane
Im	Imaginary part of complex amplitude
Re	Real part of complex amplitude
FFT	Two-dimensional Fourier transform
FFT^{-1}	Inverse two-dimensional Fourier transform
$\Delta\varphi$	Phase difference corresponding to the displacement distribution
$\Delta\Delta\varphi$	Phase difference corresponding to the first-order displacement derivative
φ_s	Phase of speckle caused by surface roughness
φ_i	Phase of incident wave
r	Position of a speckle and amplitude increment ratio
r_i	Position of incident wavefront curvature centre
r_o	Position of observation direction
k_i	Incident wave propagation vector

k_o	Observation direction vectore
I	Intensity of speckle pattern
V	Fringe contrast
ϕ	Phase of a speckle pattern
$\Delta\phi$	Phase difference
k	Sensitivity vector of a DSPI system
$\hat{i}$	Unit vector in x direction
$\hat{k}$	Unit vector in z direction
γ	Angle between incident and observation direction
w	Surface displacement in z direction
$\frac{\partial w}{\partial x}$	Out of plane displacement's derivative in x direction
δx	Amount of shearing in x direction in shearography
A	Background intensity of a fringe pattern
B	Amplitude modulation of a fringe pattern
$\Delta\phi_t$	Phase change in temporal domain
N_t	Number of temporally phase shifted fringe patterns
ϖ	Spiral phase operator
θ	Orientation map
ϕ_x	Phase derivative in x direction
ϕ_y	Phase derivative in y direction
U	Minimization function of a phase tracker model
M_w	Neighborhood region or a selected window in a fringe pattern
β_{reg}	Regularizing parameter to control smoothness of phase map in phase tracker
s	Status map to show pixels which are already solved for phase
A_v	Amplitude of a vibration
J_0	Zero order Bessel function of first kind
A_e	Amplitude of harmonic function
ς	Damping coefficient

ω	Vibration frequency
ω_n	n^{th} mode resonant frequency
I_{avg}	Intensity of time average frame
Ω	Fringe locus function
I_s	Intensity of speckle pattern of a stationary object
η	Speckle noise
I_r	Intensity of fringe pattern after normalized
g	intensity of a cosine signal
Ω_x	Frequency of a cosine signal in *x* direction
Ω_y	Frequency of a cosine signal in *y* direction
$\frac{\partial g}{\partial x}$	Discretized partial derivative of a cosine signal in *x* direction
$\frac{\partial g}{\partial y}$	Discretized partial derivative of a cosine signal in *y* direction
$\frac{\partial^2 g}{\partial x \partial y}$	Discretized second order partial derivative of a cosine signal
Ψ_2	Higher order Teager-Kaiser energy operator
CP	Complex amplitude obtained from complex phasor's method
w_{cx}	Carrier frequency in *x* direction
w_{cy}	Carrier frequency in *y* direction
$\dot{\varphi}_x$	Phase derivative in *x* direction
$\dot{\varphi}_y$	Phase derivative in *y* direction
$\ddot{\varphi}_{xx}$	Second order phase derivative in *x* direction
$\ddot{\varphi}_{yy}$	Second order phase derivative in *y* direction
$\ddot{\varphi}_{xy}$	Second order phase derivative in *xy* direction
$\dot{\varphi}_{xf}$	Phase derivative in *x* direction after filtering
$\dot{\varphi}_{yf}$	Phase derivative in *y* direction after filtering
F	Two-dimensional Fourier transform
F^{-1}	Inverse two-dimensional Fourier transform

VO	Vortex Operator
W	Window size in pixels
$\frac{\partial \varphi}{\partial x}$	Phase derivative in x direction
$\frac{\partial \varphi}{\partial y}$	Phase derivative in y direction
θ_g	Phase gradient angle
$\Delta\varphi$	Phase gradient
$\tilde{\Omega}$	Fringe locus function of a cosine fringe with conversion error
ε	Error caused by Bessel to cosine function conversion
$\Delta\tilde{\Omega}$	Change in fringe locus function introduced by a change in vibration amplitude
$\tilde{\Omega}'$	Modified fringe locus function
g_i^+	Positive residue
g_i^-	Negative residue
xg_i^+	x coordinate of a residue
yg_i^+	y coordinate of a residue
N_p	Number of residual pairs
Lm	Parameter which limits the selection process to repeat
Np	Number of population
Nc	Number of chromosomes
Pc	Probability of a chromosome to crossover
Pm	Probability of a chromosome to mutate
P	Load applied
L	Length of a cantilever beam
I_a	Area moment of inertia
w_d	Displacement sensed by DSPI system
θ_y	Rigid body rotation along y axis
T_z	Rigid body translation along z axis
υ	Poison's ratio

r_0	Radius of a specimen
r_p	Distance of a particular pixel from the centre of a specimen
D	Flexural rigidity of a plate
SNR	Signal to noise ratio

LIST OF ABBREVIATIONS

HI	Holographic interferometry
DHI	Digital holographic interferometry
TA-HI	Time average holographic interferometry
ESPI	Electronic speckle pattern interferometry
DSPI	Digital speckle pattern interferometry
TA-DSPI	Time average digital speckle pattern interferometry
DSSI	Digital speckle shearing interferometry
TA-DSSI	Time average digital speckle shearing interferometry
RPT	Regularized phase tracker
DRPT	Derivative based regularized phase tracker
GA	Genetic algorithm
HGA	Hybrid genetic algorithm
eHGA	Ensemble of hybrid genetic algorithm
EMD	Empirical mode decomposition
IMF	Intrinsic mode functions
EFEMD	Enhanced fast empirical mode decomposition
ASR	Automatic selective reconstruction
DESA	Discrete energy separation algorithm
TKEO	Teager-Kaiser energy operator
DHODA	Discrete higher order image demodulation algorithm

VO	Vortex operator
CCD	Charge-coupled device
NDT	Non-destructive testing
DPS	Digital Phase subtraction
STFT	Short term Fourier transform
SLM	Spatial light modulator
PZT	Piezo electric transducer
WFT	Window Fourier transform
CWT	Continuous wavelet transform
FFT	Fast Fourier transform
GRPT	Generalized regularized phase tracker
iGRPT	Improved generalized regularized phase tracker
SA	Simulated annealing
RSA	Reverse simulated annealing
dPSO	Discrete particle swarm optimization
AI	Artificial intelligence
2D	Two dimensional

CHAPTER ONE

INTRODUCTION

Light is electromagnetic radiation which exhibits properties of both waves and particles. Light as a wave, has wavelength, frequency, amplitude and phase. A typical human eye can detect light within a range of wavelength 390 nm to 700 nm. Though a human eye is sensitive to distinguish wavelength, frequency and amplitude, it is insensitive to phase values. Phase values of light wave would be significant and measuring phase along with amplitude would provide the complete wave-front of light. Phase difference between light beams of same wavelength causes either constructive or destructive interference. Hence interference phenomenon of light waves is exploited to determine the phase values and this technique is called as interferometry. Today, interferometry is widely used in many branches of physics and engineering and its application ranges from visualization of internal tissue microstructures to detection of gravitational waves.

Structures undergo deformation, when any kind of load applied on it. In mechanics, measuring these deformations and strains have many useful applications from structural monitoring to material characterization. Conventional deformation and strain measurement techniques such as extensometer and electric resistance strain gauges are compact, accurate, and inexpensive. However, they can only provide measurement data at a single point and these devices should be in contact with the specimen. Hence optical techniques for displacement and strain measurements were developed. They can provide full-field measurements with high accuracy and they are non-contact in nature. Hence there is no additional stiffness appended in the specimen.

These optical techniques are mainly classified under two categories, coherent and incoherent light based methods. Coherent techniques use wave properties of light such as interference and diffraction and incoherent techniques use geometrical properties of a light beam. In this thesis, novel methods to determine displacement and displacement derivatives such as strain, curvature, twist using coherent techniques such as holography, speckle interferometry and shearography are proposed.

1.1 Holography

Holography is a field of science which deals with the practice of making holograms. In 1948, Dennis Gabor invented holography unintentionally, during his research to improve the quality of electron microscope. The term holography comes from Greek words ‘holo’ which means whole and ‘graphe’ which means drawing. This term was coined by Dr. Gabor since holograms capture the whole wave front. Until the invention of lasers, making optical holograms was not practical as they need coherent light source. With the advent of the laser, full potential of holograms in various applications has been explored and Dennis Gabor was awarded with a Nobel Prize in 1971 for his invention and development of holographic method.

In holography, a coherent light beam is split into two beams. Reference beam reaches a photographic plate directly and the other beam is reflected from the object before reaching the photographic plate. The interference between these two beams are recorded in the photographic plate. In photography, a lens is used for image formation however in holographic recording the interference pattern is recorded directly on the photographic plate without any lens. After chemical processing of the photographic plate, a reference beam with same wavelength is used for reconstruction of the object wave. In Gabor’s holography, the reconstructed image has twin-image (real and virtual)

and zero-order term. Leith and Upatnieks suggested an off-axis holography technique, which provides solution to this zero-order and twin-image problem. Since then, it found applications in many fields from microscopy to data storage. Holographic interferometry is one such application. It is a technique to measure static and dynamic displacements of an object in sub-wavelength accuracy. Holograms of an object before and after deformation are recorded with the same photographic plate and the displacements are visible in the form of fringes in the reconstructed object wave as shown in Fig. 1.1.

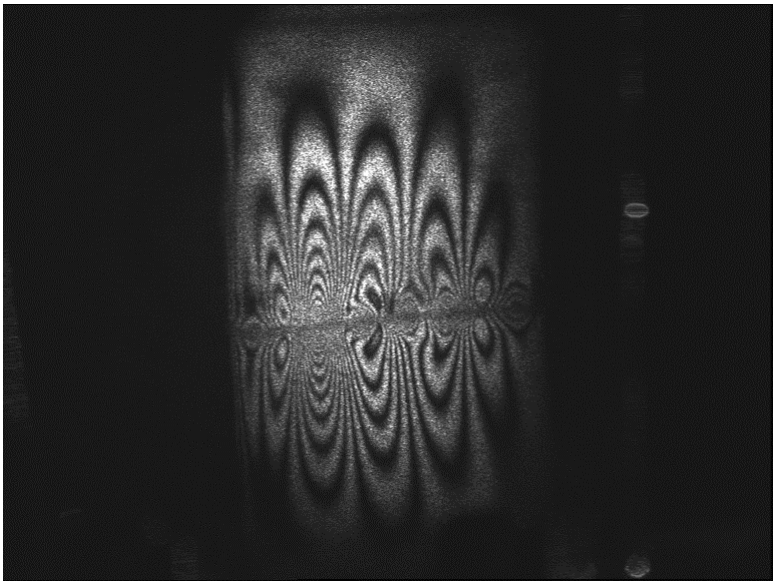

Figure 1.1 Holographic interferometric fringes.

After invention of electronic image capturing devices like charge-coupled device (CCD), photographic plates in holographic process are replaced and this provided a wide range of new capabilities. Digital holography records whole field information of an object using an electronic device (e.g. CCD), and the reconstruction of an object wave is carried out numerically. Several algorithms such as convolution method and pure Fourier transform have been proposed for reconstructing an object wave. Recording and reconstruction are integrated into one system, and processing of

holograms can be realized digitally without any intermediate photographic recording and wet chemical processing of photographic plates. In recent years, digital holographic technique has been successfully applied in various fields including holographic interferometry. In digital holographic interferometry (DHI), the numerical values of phase difference caused by the deformation is obtained. Hence it enables full field measurement of displacement and strain. However, holographic setup is highly sensitive to external disturbances, it can be applied only under laboratory conditions.

1.2 Speckle pattern interferometry

Speckle pattern interferometry is a technique, which uses correlation between speckle patterns to measure out of plane and in-plane displacements in components with optically rough surface. Speckle patterns, which typically occur in diffuse reflections of monochromatic light, are intensity patterns created by interference of many waves of same wavelength with different phase and amplitude. In holography, speckles are considered to be unwanted noise which reduces the resolution of the captured holograms.

Later it was realized that speckles can carry information about surface deformation. In 1971, Butters and Leendertz found that the direct recording of a two-beam interference pattern between a reference wave and a speckle wave carries the phase information of the speckle wave. A separate numerical reconstruction to get the complex amplitude is not necessary as in the case of DHI.

Speckle pattern interferometry requires a setup similar to holography where an interference pattern between a reference beam and an object beam is recorded. However speckle pattern interferometry uses TV camera with lens to capture subjective speckle pattern hence it is also called as ‘TV Holography’. Based on the capturing device used,

it is called as either electronic speckle pattern interferometry (ESPI) or digital speckle pattern interferometry (DSPI). Since this technique uses speckle correlation for measuring surface deformation, in-plane surface deformation measurement is also possible which is not the case with optical interferometry and holographic interferometry. This technique is less sensitive to ambient conditions than holography so it can be used outside laboratory conditions. However this technique is susceptible to rigid body motions and the reference beam should be coherent with object beam.

1.3 Shearography

Shearography or digital speckle pattern shearing interferometry (DSSI) is a coherent optical technique to measure surface displacement derivatives directly. Shearography is similar to DSPI except that it does not need a reference light wave to form speckle pattern but it uses the object itself as the known reference. The image would be sheared to obtain the displacement derivatives in the sheared direction. Since there is no separate reference wave, there is no need to maintain coherency between reference wave and object wave. Hence shearography requires simple experimental setup and does not require extreme stability. Due to these reasons, it is widely used in industries for in-situ measurements.

All these coherent optical techniques can be used for defect detection in nondestructive testing (NDT), however shearography is more useful for this application as it is only sensitive to surface deformation derivatives and insensitive to gross deformations (Hung, 1997; Yang and Hung 2004; Zhu et al, 2011). Hence among coherent optical techniques, only shearography setup can be made as portable units similar to existing NDT methods such as ultrasonic testing. Today, shearography is one

of the most robust NDT methods which is predominantly used in automotive and aerospace industries (Zhu et al, 2011).

1.4 Scope and outline of thesis

Although coherent optical techniques are widely used in all major branches of experimental mechanics such as material properties determination, structural analysis and NDT, there are still considerable limitations and improvements are required in these techniques to face today's challenges of unprecedented complexity. In coherent optical techniques, phase difference, which is caused by displacement and displacement derivatives, are retrieved from the captured frames. Most widely used phase retrieval techniques either require more than one frame at every deformation as in case of temporal phase shifting techniques or require complex experimental setup as in case of spatial phase shifting techniques. These limitations in phase retrieval methods prevent coherent optical techniques for real time dynamic deformation and strain measurements.

The specific limitations and challenges in DHI, DSPI and DSSI are summarized as follows: (1) In DHI, the quality of an extracted phase map is highly affected by speckle noise. Noise filtering methods require very high computational time and it is difficult to further measure high-quality higher-order displacement derivatives. (2) In speckle pattern interferometry and shearography, few studies have been carried out to evaluate the phase distributions from a single fringe pattern. Another issue is how to measure phase derivatives directly from the fringe pattern. (3) In some applications with coherent optical methods such as time-average vibration analysis, fringe quality of interferometers needs to be improved. Existing techniques require complex experimental setup for improving fringe quality and for determination of vibration amplitude values. (4) Phase and phase derivatives maps obtained from most of phase

retrieval techniques would be wrapped. Existing phase unwrapping methods cannot unwrap noisy phase maps effectively and they also require more computational time.

The objectives of this research work are to develop new phase and phase derivatives determination techniques in coherent optical techniques, and to overcome the existing problems in some applications with these techniques. These objectives are summarized as follows: (1) In DHI, a Teager operator based discrete higher order image demodulation algorithm is proposed to determine the phase derivatives maps. This method provides higher-order displacement derivatives, such as first-order and second-order displacement derivatives, and also a phase distribution of the test object is determined. (2) In speckle pattern interferometry and shearography, a novel method to determine phase derivatives maps directly from a fringe pattern is proposed. This method uses fringe orientation and fringe density maps to determine deformation derivatives. Furthermore, a novel derivative based regularized phase tracker method is proposed to obtain a phase map directly from a single DSPI or DSSI fringe patterns. (3) In time average vibration analysis, a method to improve fringe contrast is proposed. Furthermore, a method to determine vibration amplitude from single time average fringe pattern is proposed. (4) A phase unwrapping method to address noisy phase maps using an artificial intelligence method called ensemble of hybrid genetic algorithm is proposed. (5) A method to determine elastic modulus of a cantilever beam using DSPI is proposed. This method is able to reduce the influence of a small rigid body displacement in elastic modulus determination. A list of publications arising from this research work during the candidate's Ph.D. period is included in Appendix. Most of the results presented in this thesis are mainly from these publications, but an in-depth analyses and detailed descriptions of the methods and their applications are also included in this thesis. The research work in this thesis may contribute to a better

understanding of coherent optical techniques principles and their applications in the field of experimental mechanics. This may also shed some light on the further development of these techniques for some novel practical applications.

The thesis is organized into six chapters.

In Chapter 1, a brief introduction of coherent optical techniques is given. In addition, some challenges existing in these techniques are described, and the objectives and significance of this research work are also presented.

In Chapter 2, a literature review is conducted with five parts. In the first part, wave theory of light is presented. In the second part, principles of various coherent optical techniques such as holography, speckle pattern interferometry and shearography are presented. In the third part, different spatial and temporal phase evaluation techniques are reviewed. In the fourth part, review of optical techniques employed for vibrational analysis are presented and in the last part, a review of principles and classifications of phase unwrapping is presented.

In Chapter 3, the theories of the proposed displacement and displacement derivatives methods are presented, and the proposed theories to address the existing challenges in some applications with these techniques are also described.

In Chapter 4, experimental works which are carried out to validate the proposed methods are presented, and the descriptions about equipment and specimens are also included.

In Chapter 5, the simulation and experimental results of the proposed techniques are presented, and the results in the applications are demonstrated. The analyses to validate the accuracy and the influence of different parameters on the performance of the proposed methods are also presented. In addition, the advantages, disadvantages of the proposed techniques are analyzed in detail.

In Chapter 6, the research work is concluded, and the research directions for the further study are recommended.

CHAPTER TWO

LITERATURE REVIEW

2.1 The basics of light

The Maxwell equations which provides the electromagnetic wave theory, describes the propagation of a light wave in vacuum as shown below.

$$\nabla^2 E - \frac{1}{c^2}\frac{\partial^2 E}{\partial t^2} = 0 \tag{2.1}$$

where E is the electric field strength, ∇^2 represents Laplace operator which is described as

$$\nabla^2 = \frac{\partial^2}{\partial x^2} + \frac{\partial^2}{\partial y^2} + \frac{\partial^2}{\partial z^2}, \tag{2.2}$$

x, y and z represent the spatial coordinates, t represents the temporal coordinate, and c is the speed of the light wave in vacuum ($2.9979 \times 10^8\ \mathrm{m/s}$).

The electrical field E is a vector quantity, which represents that a light wave can vibrate in any direction perpendicular to the propagation. Light wave vibrating in a single plane is called linear polarized light and the above scalar wave equation can be rewritten as (Kreis, 2005; Schnars and Jueptner, 2005)

$$\frac{\partial^2 E}{\partial z^2} - \frac{1}{c^2}\frac{\partial^2 E}{\partial t^2} = 0 \tag{2.3}$$

where the propagation of the light is in the *z* direction. For a linearly polarized and harmonic plane wave, the important solution of Eq. (2.3) is described by

$$E(x, y, z; t) = A_w \cos(2\pi ft - \vec{k}\vec{r} + \varphi_0) \tag{2.4}$$

where A_w is the real amplitude of the light wave, f is the frequency of the light wave, $\vec{k}$ is the wave vector, $\vec{r}$ is the spatial vector [$\vec{r} = (x, y, z)$], and φ_0 is a constant phase. In this thesis, $\varphi = -\vec{k}\vec{r} + \varphi_0$ is defined as phase. The wave represented in a complex exponential form is often algebraically easier to deal with in the wave calculation and in derivations of optical principles. Hence the wave expression in the complex exponential form is written as

$$E(x, y, z; t) = A_w \exp\left[j(2\pi ft - \varphi)\right] \tag{2.5}$$

where $j = \sqrt{-1}$. The real part of this complex exponential alone represents the physical wave. In many cases, $2\pi ft$ term is ignored since the spatial part of the electrical field is of the most interest. Hence, in this thesis, a light wave is represented as:

$$E(x, y, z; t) = A_w \exp\left[-j\varphi\right] \tag{2.6}$$

2.2 Review of coherent optical techniques

2.2.1 Holographic interferometry

Dr. Gabor (1948) proposed in-line optical holographic setup as shown in Fig. 2.1. A coherent light source is split into two waves, i.e., reference and object waves. The angle between object and reference waves is small or close to zero (Xu et al., 2002,

2003; Sucerquia et al., 2006a, 2006b). An object is illuminated, and the object wave, which is a diffracted wavefront from the object, is then propagates towards a recording medium. The object and reference waves interfere before recording with a help of a beam splitter cube, and an interference pattern is captured on the surface of the recording medium. Without a loss of generality, only a given pixel (*m*, *n*) is considered. The recorded interference pattern is called hologram and the intensity $I_o(m,n)$ of a hologram recorded is given by:

$$E_o(m,n) = a_o(m,n)\exp\left[-j\,\varphi_o(m,n)\right] \tag{2.7}$$

$$E_r(m,n) = a_r(m,n)\exp\left[-j\,\varphi_r(m,n)\right] \tag{2.8}$$

$$\begin{aligned} I_o(m,n) &= a_0^2(m,n) + a_r^2(m,n) + E_0(m,n)E_r^*(m,n) + E_0^*(m,n)E_r(m,n) \\ &= a_0^2(m,n) + a_r^2(m,n) + 2a_0(m,n)a_r(m,n)\cos[\varphi_r(m,n) - \varphi_o(m,n)] \end{aligned} \tag{2.9}$$

where $a_o(m,n)$ and $a_r(m,n)$ are real amplitude of object wave and reference wave; $\varphi_o(m,n)$ and $\varphi_r(m,n)$ are the phase of object wave and reference wave.

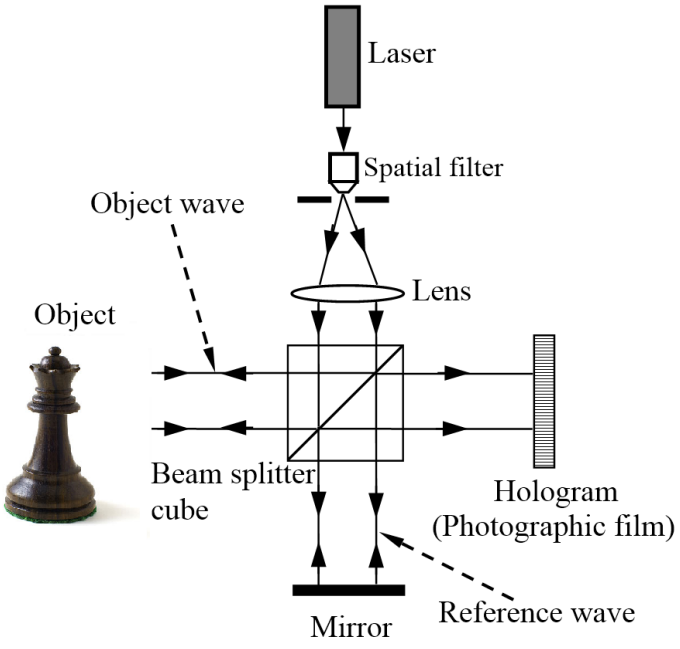

Figure 2.1 A typical in-line optical holographic experimental arrangement.

In Gabor's in-line optical holographic setup, the angle between the object and reference waves is almost zero. This causes superposition of zero order term, virtual and real terms during holographic reconstruction. An appropriate angle between object and reference waves was introduced by Leith and Upatnieks (1962, 1963) to overcome this problem. This off-axis experimental setup is shown in Fig. 2.2 (Schnars and Jueptner, 2005). The basic principles of wave propagation and interference are the same with those of the in-line optical holographic setup. However, in off-axis optical holographic setup, the angle between object and reference waves is larger than the in-line holographic setup.

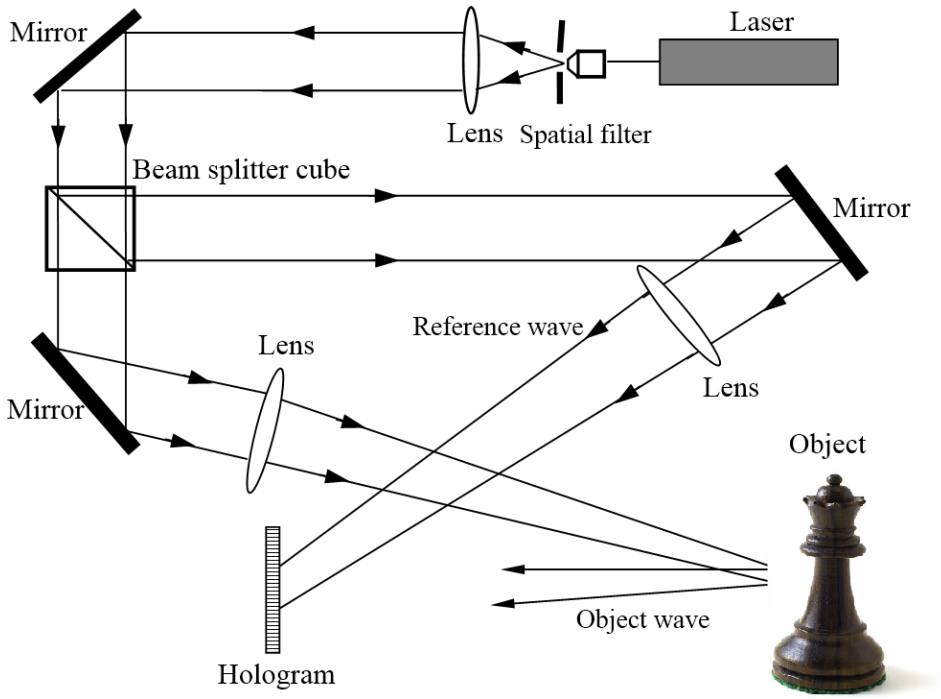

Figure 2.2 An off-axis optical holographic experimental arrangement.

In optical holography, a photographic plate is used as a recording device. To reconstruct a hologram recorded, a reference wave of the same wavelength as in the

recorded hologram is used to illuminate the hologram. The modulation procedure, when the reference wave illuminates the recorded hologram, can be described by

$$I_o(m,n)E_r(m,n) = \left[\left|E_o(m,n)\right|^2 + \left|E_r(m,n)\right|^2 \right] E_r(m,n) + E_o^*(m,n)E_r^2(m,n) + \left|E_r(m,n)\right|^2 E_o(m,n) \tag{2.10}$$

where the first term is a zero-order term or DC term, and the second and third terms form real and virtual images, respectively. In off-axis optical holographic setup, these three terms is effectively separated which was not the case in in-line holographic setup.

Holographic interferometry is one of the coherent optical techniques used in experimental mechanics. It is a non-contact and non-destructive technique which is used various applications, such as deformation measurement and object surface contouring (Schnars and Jueptner, 2005). There are two main types of holographic interferometry, i.e., double exposure and time-average methods. In double exposure method, a reference state of the object is first recorded in a recording medium, and a deformed state of the object is recorded in the same recording medium. In the optical reconstruction, interference fringes, which represents the deformation in the object are visible. In holographic interferometry, the wavefront of reference and deformed states of the object is given by

$$I_1(m,n) = A_0(m,n)\exp\left[j\varphi_1(m,n)\right] \tag{2.11}$$

$$I_2(m,n) = A_0(m,n)\exp\left[j\varphi_2(m,n)\right] \tag{2.12}$$

where $A_0(m,n)$ denotes the real amplitude which is assumed as constant, and $\varphi_1(m,n)$ and $\varphi_2(m,n)$ denote phase distributions of the object before and after deformation.

The phase value $\varphi_2(m,n)$ is described by $\varphi_2(m,n)=\varphi_1(m,n)+\Delta\varphi$, where $\Delta\varphi$ is the phase difference between the reference and deformed states, which is directly related to the measured physical quantities. Hence, when a recorded hologram is illuminated by a reference wave, both wave fields are reconstructed as shown in Fig. 1. The intensity distribution $I_d(m,n)$ is calculated by the square of the summation of the two reconstructed complex amplitudes.

$$\begin{aligned} I_d(m,n) &= \left[I_1(m,n)+I_2(m,n)\right]\left[I_1(m,n)+I_2(m,n)\right]^* \\ &= 2A^2\left[1+\cos(\Delta\varphi(m,n))\right] \end{aligned} \tag{2.13}$$

In optical holographic interferometry, quantitative phase measurement is difficult. A manual fringe counting can be employed for obtaining phase distribution in optical holographic interferometry but it is not accurate. Hence the phase is usually calculated from three or more phase-shifted holograms using a phase-shifting algorithm. This requires additional experimental effort and it is not suitable for dynamic measurements. Hence, it is important to develop digital approaches in order to quantitatively extract the phase distribution that is directly related to the measured physical quantity from a single interferogram.

The digital holography was developed, when CCD technology is employed in the holographic research field (Schnars and Jüptner, 1994; Cuche et al., 1999). The experimental setups for recording in digital holography are the same as those shown in Figs. 2.1 and 2.2 except that a CCD is used instead of a photographic plate. Hence, numerical recording in digital holography does not require a reconstruction setup and wavefronts are reconstructed numerically.

Digital holography has several advantages over conventional optical holographic technique: (1) The holograms are recorded digitally and no wet chemical processing of a photographic plate is required; (2) the holograms can be recorded in real time at a video frequency which is useful in dynamic measurements; (3) numerical reconstruction and phase evaluation can be integrated into a single system and quantitative phase measurement is easier and more accurate.

Numerical reconstruction process is based on the Fresnel–Kirchhoff integral since the wavefront is formed by a diffraction of the reconstructing wave at the micro-structure of a hologram. The diffraction of a light wave at an aperture, which is perpendicular to an incoming reference beam, is described by the Fresnel–Kirchhoff integral as shown below.

$$\chi(\xi',\eta') = \frac{j}{\lambda}\int_{-\infty}^{+\infty}\int_{-\infty}^{+\infty} H(u,v)R(u,v)\frac{1}{\rho}\exp\left(-j\frac{2\pi}{\lambda}\rho\right)\left(\frac{1+\cos\theta}{2}\right)dudv \tag{2.14}$$

where $H(u,v)$ is a hologram, $R(u,v)$ is a reference wave of wavelength λ and $\left[\rho = \sqrt{(u-\xi')^2 + (v-\eta')^2 + d^2}\right]$. The expression of ρ is approximated using Taylor series expansion and the discrete version of Eq. (2.14) after Fresnel approximation is given by:

$$\begin{aligned}\chi(m,n) = \frac{j}{\lambda d}\exp\left(-j\frac{2\pi}{\lambda}d\right)\exp\left[-j\pi\lambda d\left(\frac{m^2}{M^2\Delta u^2}+\frac{n^2}{N^2\Delta v^2}\right)\right]\sum_{k=0}^{M-1}\sum_{l=0}^{N-1}H(k,l)\\ \times R(k,l)\exp\left[-j\frac{\pi}{\lambda d}\left(k^2\Delta u^2 + l^2\Delta v^2\right)\right]\exp\left[j2\pi\left(\frac{mk}{M}+\frac{nl}{N}\right)\right]\end{aligned} \tag{2.15}$$

The intensity distribution $I_h(m,n)$ and the phase distribution $\varphi(m,n)$ can be directly extracted from the reconstructed complex amplitude.

$$I_h(m,n) = \left|\chi(m,n)\right|^2 \tag{2.16}$$

$$\varphi(m,n) = \arctan\frac{\mathrm{Im}\left[\chi(m,n)\right]}{\mathrm{Re}\left[\chi(m,n)\right]} \tag{2.17}$$

where Im and Re denote imaginary and real parts of a complex amplitude, respectively.

This numerical reconstruction requires more computation. It is demonstrated that numerical reconstruction using convolution method is better than Fresnel approximation method when the reconstruction distance is relatively small (Dakoff et al., 2003). Hence a convolution approach is proposed as described by (Schnars and Jueptner, 2005; Kreis et al., 1997)

$$\chi(\xi',\eta') = FFT^{-1}\left\{FFT\left[H(u,v)R(u,v)\right]FFT\left[g(u,v)\right]\right\} \tag{2.18}$$

where FFT and FFT^{-1} denote a two-dimensional (2D) Fourier transform and an inverse 2D Fourier transform, respectively. A fast Fourier transform can be implemented to increase the computation speed. Additionally, pixel size in the image plane is independent of the reconstruction distance and the wavelength, and the pixel size is equivalent to the pixel size of CCD camera.

When a point source of the reference wave is located at the same plane of the object, numerical reconstruction process can be simplified as a pure Fourier transform (Wagner et al., 1999). A schematic digital lensless Fourier holographic recording setup is shown in Fig. 2.3. The spherical reference wave can be simplified as

$$R(u,v) \approx \frac{1}{d}\exp\left(-j\frac{2\pi}{\lambda}d\right)\exp\left[-j\frac{\pi}{\lambda d}\left(u^2+v^2\right)\right] \tag{2.19}$$

Hence, the reconstructed complex amplitude can be described by

$$\chi(\xi',\eta') = C\ \exp\left[\ j\frac{\pi}{\lambda d}\left(\xi'^2+\eta'^2\right)\right] FFT^{-1}\left[H(u,v)\right] \tag{2.20}$$

where *C* denotes a constant complex value.

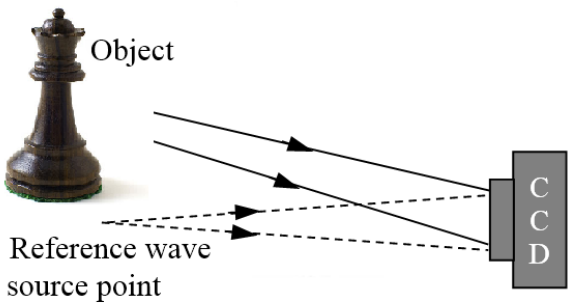

Figure 2.3 Digital lensless Fourier holography.

In optical holographic interferometry, two light waves scattered from an object in different states are superimposed. However, as mentioned earlier, the phase distribution cannot be determined from a single interferogram. In DHI, quantitative phase measurement from a single hologram is possible. Hence, in each state of the object a digital hologram is recorded. Instead of superimposing more than one hologram as in conventional HI using photographic plates, the digital holograms are reconstructed separately. Difference between the reconstructed phase maps provides the change between the states (Schnars and Jueptner, 2005). This digital phase subtraction method (DPS) provides noisy wrapped deformation map. Since the wrapped phase map extracted is highly contaminated by speckle noise, the subsequent

phase unwrapping operation may not succeed. One strategy to overcome this problem is to process the original wrapped phase map to filter noise before phase unwrapping. However, in many practical applications, the direct filtering of the wrapped phase map is difficult due to high fringe density and low signal to noise (SNR) ratio. It is well known that phase itself is not a signal but rather a property of the signal (Ghiglia and Pritt, 1998). Hence, a complex phasors method which reduces speckle noise in the wrapped phase map was proposed (Chen et al., 2008; Quan et al., 2009). A complex phasor $CP(m,n)$ is calculated by multiplying complex amplitude signal $\chi(m,n,2)$, reconstructed from the hologram at the second (or deformed) state with the conjugate of complex amplitude signal $\chi^*(m,n,1)$, reconstructed from the hologram captured at the initial state. Without a loss of generality, only a given pixel (m, n) is considered.

$$\begin{aligned} CP(m,n) &= \chi(m,n,2)\chi^*(m,n,1) \\ &= a'(m,n)\exp\{j[\Delta\varphi(m,n)]\} \end{aligned} \tag{2.21}$$

$$\Delta\varphi(m,n) = \arctan\frac{\sum \mathrm{Im}[CP(m,n)]}{\sum \mathrm{Re}[CP(m,n)]} \tag{2.22}$$

where $\Delta\varphi$ is the phase difference caused by the deformation.

The complex field obtained $CP(m,n)$ is then virtual sheared and product of sheared complex field $CP'(m,n)$ and conjugate of complex field CP^* provides phase derivatives as shown in Eq. (2.23) and Eq. (2.24).

$$\begin{aligned} \Gamma(m,n) &= CP'(m,n)CP^*(m,n) \\ &= a''(m,n)\exp\{j[\Delta\Delta\varphi(m,n)]\} \end{aligned} \tag{2.23}$$

$$\Delta\Delta\varphi(m,n) = \arctan\frac{\sum \mathrm{Im}[\Gamma(m,n)]}{\sum \mathrm{Re}[\Gamma(m,n)]} \tag{2.24}$$

where $\Gamma(m,n)$ is a complex field of the phase derivative and $\Delta\Delta\varphi(m,n)$ is the slope in the sheared direction. The phase derivatives maps obtained from this method are affected by speckle noise, hence a sin-cos filtering or short time Fourier transform (STFT) filtering is applied to process the phase derivative maps (Chen et al., 2008; Quan et al., 2009). The phase and phase derivative maps obtained from this method are wrapped and a separate phase unwrapping technique is necessary to obtain unwrapped displacement, slope and curvature maps.

A different approach of modeling the DHI reconstructed interference field as a piecewise polynomial phase was developed (Gorthi and Rastogi, 2009a; Gorthi and Rastogi, 2009b). The derivative maps were determined by computing polynomial coefficients of different segments of the interference field using high order instantaneous moments of the signal. This method is more suitable for determining the first order derivative than determining the higher order derivatives hence the complex lag moment method for the determination of high quality higher order derivatives was proposed (Rajshekhar and Rastogi, 2011; Cornu et al., 2007). Determination of cross derivative map like twist map is not possible in complex lag moment method because this method is only useful for the determination of any nth order derivative in a given direction. This method requires very high computation time as it requires as many Fourier transforms as the row or column size of the reconstructed hologram.

2.2.2 Speckle pattern interferometry

Speckle pattern interferometry refers to a wide range of speckle metrology techniques such as TV holography (Butters and Leendertz, 1971), electronic speckle pattern interferometry (ESPI) (Butters et al, 1978), and digital speckle shearing interferometry (DSSI) (Ganesan et al, 1988; Hung, 1979; Hung, 1989). These optical techniques are employed to measure a various physical quantities, including in-plane and out-of-plane displacement, strain, twist, curvature, and 3-D profile.

Speckle patterns that are created by scattered coherent light from an optically rough surface can be classified into two types, depending on the optical systems used to observe them. If the speckle size depends on the size of area of illumination and the distance between the rough surface and the screen but does not depend on the optical system used to observe it, it is called objective speckle (Rastogi, 2011; Rastogi, 2015). If the speckle size depends on the aperture of the optical system used to observe it, it is called subjective speckle pattern. Subjective speckle pattern is used in speckle pattern interferometry setups such as TV Holography, digital speckle pattern interferometry (DSPI) and shearography.

Speckle patterns can be modified by displacements in the rough surface which scatters coherent light, changes in wavelength of coherent light source and changes in illumination or observation geometry. The phase value of a speckle pattern is influenced by all these factors as given by:

$$\varphi = \varphi_s + \varphi_i + \vec{k}_i.(\vec{r} - \vec{r}_i) + \vec{k}_o.(\vec{r}_o - \vec{r}) \tag{2.25}$$

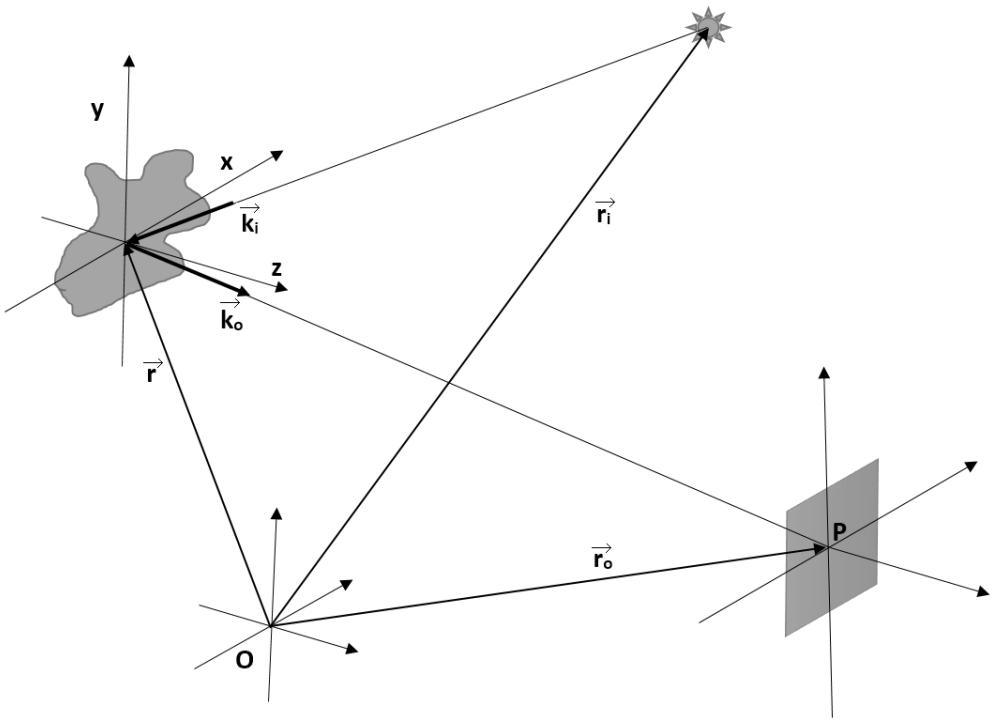

Figure 2.4 Geometry for the sensitivity of the phase of a speckle

where φ is the phase of a speckle, φ_s is the random component caused due to roughness of the object, φ_i is the actual phase of the beam from the light source, $\vec{r}$ is the position vector, $\vec{r}_i$ is the incident wavefront's curvature center, $\vec{r}_o$ is observation point's position vector and $\vec{k}_i$ and $\vec{k}_o$ are the wave propagation vectors of incident and observation directions, respectively (Rastogi, 2015).

In DSPI, an interference pattern produced between two speckle patterns one from an object and another from a reference plate is captured using a CCD camera. The intensity I of a speckle pattern interferogram which is helpful in measuring physical quantities is given by:

$$I = \left[I_r + I_o\right] + 2\sqrt{I_r I_o}\cos(\varphi_r - \varphi_o) \tag{2.26}$$

where I_r and I_o are the intensities of the reference and object beams and φ_r and φ_o are the phase of reference and object beams respectively. The above equation can be simplified as

$$I = I_0(1+V\cos\phi) \tag{2.27}$$

$$I_0 = I_r + I_o \tag{2.28}$$

$$V = \frac{2\sqrt{I_r I_o}}{I_r + I_o} \tag{2.29}$$

where I_0 is the background intensity, V is the fringe contrast or fringe visibility and ϕ is the phase difference between reference and object beam. This interference pattern alone would not be enough to record a physical event as the phase ϕ is influenced by random speckle phase caused by surface roughness of object and reference plate. Interferograms at different states of an object have to be recorded, then a change in phase value would be due to a physical event. An interferogram recorded after such deformation is given by:

$$I(m,n,t) = I_0[1+V(m,n)\cos\{\phi(m,n,t)\}] \tag{2.30}$$

$$\phi(m,n,t) = \phi(m,n,0) + \Delta\phi(m,n,t) \tag{2.31}$$

where $\Delta\phi$ is the phase difference due to a physical event at t. t denotes either time in dynamic measurement or different states in a static measurement. Since phase difference $\Delta\phi$ is directly proportional to a physical quantity, various phase retrieval methods were suggested in last few decades. These phase retrieval techniques are discussed in detail later in this chapter.

Unlike, holographic interferometry, DSPI does not capture the entire wavefront but an interference of speckle patterns. Hence this technique is not as sensitive as holographic interferometry. In addition, as mentioned earlier phases in a speckle pattern are influenced by displacements of an object in all directions. Hence this method can be employed for both in-plane and out of plane displacement measurement where holographic interferometry can only be employed for out of plane displacement measurement.

In Fig. 2.5, a schematic diagram of an out of plane displacement measurement DSPI system is shown. The sensitivity vector $\vec{k}$ of a DSPI setup is given by:

$$\vec{k} = \vec{k}_i - \vec{k}_o = \frac{-2\pi}{\lambda}[(\sin\gamma)\vec{i} + (1+\cos\gamma)\vec{k}] \tag{2.32}$$

where $\vec{i}$ and $\vec{k}$ are unit vectors in the x and z directions respectively, γ is the angle between an illumination beam and an observation direction and λ is the wavelength of the laser source. The illumination and observation directions are coincident in an out of plane displacement sensitive interferometer and γ is close to zero. Hence in this configuration, phase difference $\Delta\phi$, which is highly sensitive to the displacement of the object in z direction is given by:

$$\Delta\phi = \frac{-4\pi w}{\lambda} \tag{2.33}$$

where w is the surface displacement of the object in the z direction.

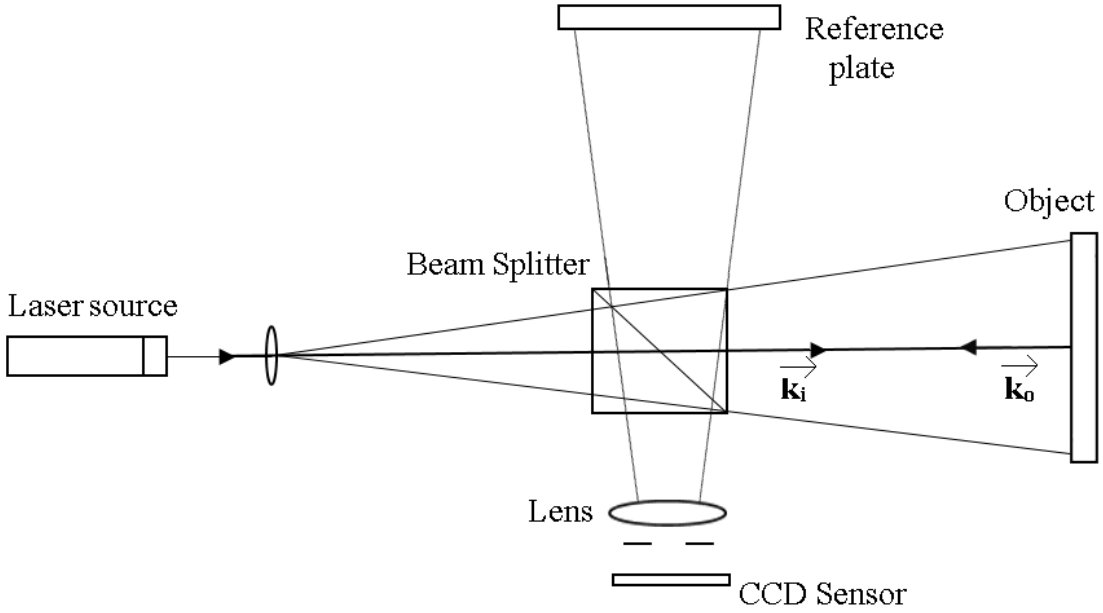

Figure 2.5 Out of plane interferometer

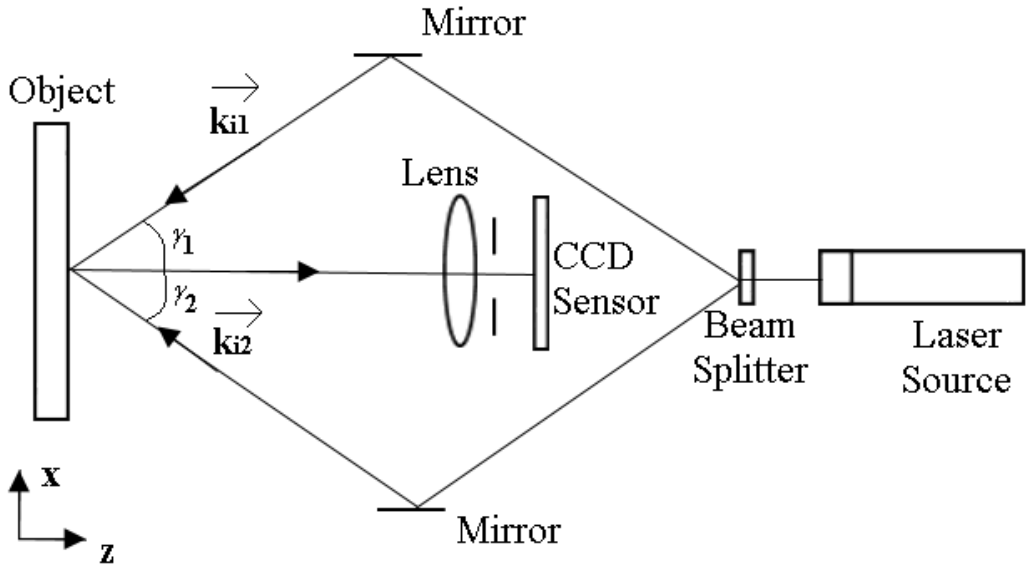

Figure 2.6 In-plane interferometer

In Fig. 2.6, a schematic diagram of an in-plane displacement measuring DSPI setup is shown. In this setup, two expanded collimated beams from opposite directions $\vec{k}_{i1}$ and $\vec{k}_{i2}$ illuminate the object. The angle between the directions of the illumination beams with the observation direction are γ_1 and γ_2. Since these angles are approximately equal, it is assumed that $\gamma_1 = \gamma_2 = \gamma$. There is no reference plate used in in-plane displacement sensitive interferometer since the interference of speckle pattern occurs between the speckle patterns created by two illumination beams. This setup is sensitive to the surface displacement of the object in x direction and phase difference $\Delta\phi$ is given by:

$$\Delta\phi = \frac{-4\pi}{\lambda} u \sin\gamma \tag{2.33}$$

where u is the surface displacement of the object in x direction. Hence the sensitivity of this setup is maximum when $\gamma = \frac{\pi}{2}$ and the sensitivity is zero when $\gamma = 0$. In other words, the sensitivity of in-plane displacement component would become zero when illumination beam and observation direction coincides, which is the case for an out of plane displacement setup.

Since DSPI can measure in-plane and out of plane displacements, various methods to measure three dimensional (3D) displacements of an object have been suggested (Yang et al, 2014). These 3D displacement measurement setups are combination of both in-plane and out of plane displacement measurement setups, which either use different channels or different wavelength for measuring displacement components in all three directions.

2.2.3 Shearography

Digital shearography or DSSI is used to measure displacement derivatives of an object, which is carried out by optical shearing. The displacement derivative in a particular direction can be obtained in shearing the speckle pattern in that particular direction. Due to the shearing, every point in the image plane receives signals from two different points from the object and vice versa as shown in Fig. 2.7. In DSSI, an optically rough object is illuminated by a coherent source, the speckle pattern created on the object surface would interfere with a sheared speckle pattern. Since this method does not involve interference between two different beams, this method is less sensitive to environmental conditions.

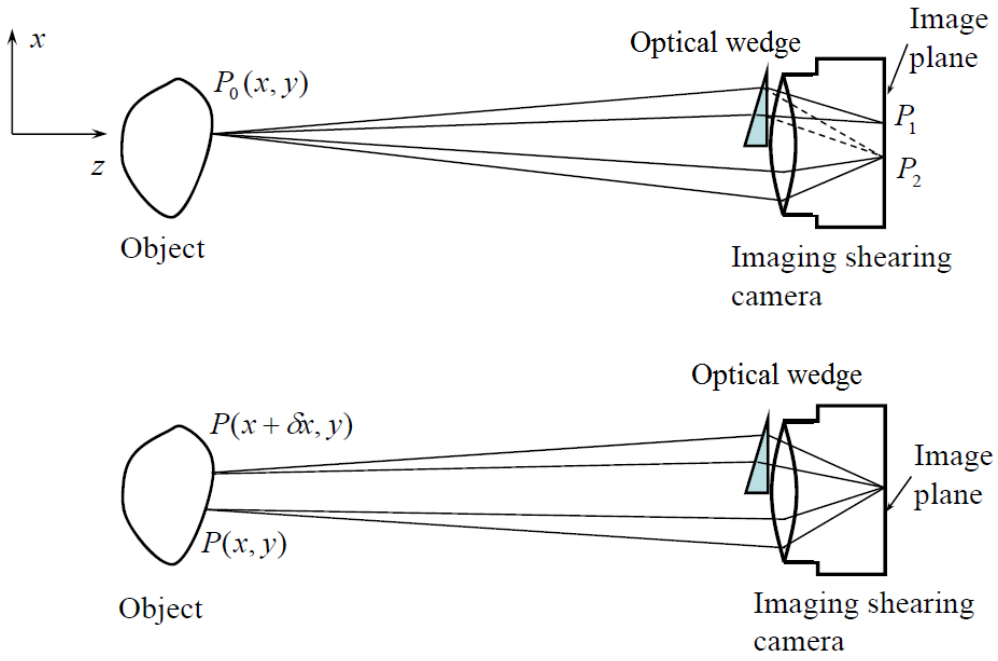

Figure 2.7 Shearography principle

The intensity I recorded after interference between two speckle patterns is given by:

$$I(m,n) = I_0[1+V(m,n)\cos\{\phi(m,n)\}] \tag{2.34}$$

where ϕ is the phase difference caused by shearing. Similarly, an interference pattern obtained after loading is given by:

$$I(m,n,t) = I_0[1+V(m,n)\cos\{\phi(m,n,0)+\Delta\phi(m,n,t)\}] \tag{2.35}$$

where $\Delta\phi$ is the phase difference caused by loading and it is given by:

$$\Delta\phi = \frac{2\pi}{\lambda}[\sin\alpha\frac{\partial u}{\partial x}+\sin\beta\frac{\partial v}{\partial x}+(1+\cos\alpha)\frac{\partial w}{\partial x}]\delta x \tag{2.36}$$

where α is the angle between illumination and observation direction in xz plane, β is the angle between illumination and observation direction in yz plane, δx is the amount of shearing in the x direction and u , v and w are components of surface displacement in x , y and z directions respectively. For a near normal illumination and observation condition, $\alpha \approx \beta \approx 0$. Hence the phase difference for such condition is given by:

$$\Delta\phi = \frac{4\pi\delta x}{\lambda}\frac{\partial w}{\partial x} \tag{2.37}$$

Different methods were proposed to introduce this shearing effect. Introducing an optical wedge is one such method as shown in Fig. 2.7. Since it does not contain any movable parts, this kind of system is more robust and compact. However, such an optical wedge can provide a fixed amount of shearing, hence this method is not

flexible (Leendertz and Butters, 1973; Hung, 1989; Rastogi, 2015). A shearography setup which uses a modified Michelson's interferometer with a tilting mirror to introduce sharing is shown in Fig. 2.8. Since this contains an adjustable mirror tilt, it is possible to control the amount of shearing introduced. Hence this configuration is more flexible and compact (Rastogi, 2015). Utilizing the birefringence properties of a liquid crystal spatial light modulators (SLM) to introduce shearing in DSSI setup were also suggested (Falldorf et al, 2009). Since SLM based shearing does not have movable parts and also the amount of shearing is adjustable, this kind of setup has advantages of both optical wedge method and tilting mirror method (Falldorf et al, 2009; Rastogi, 2015).

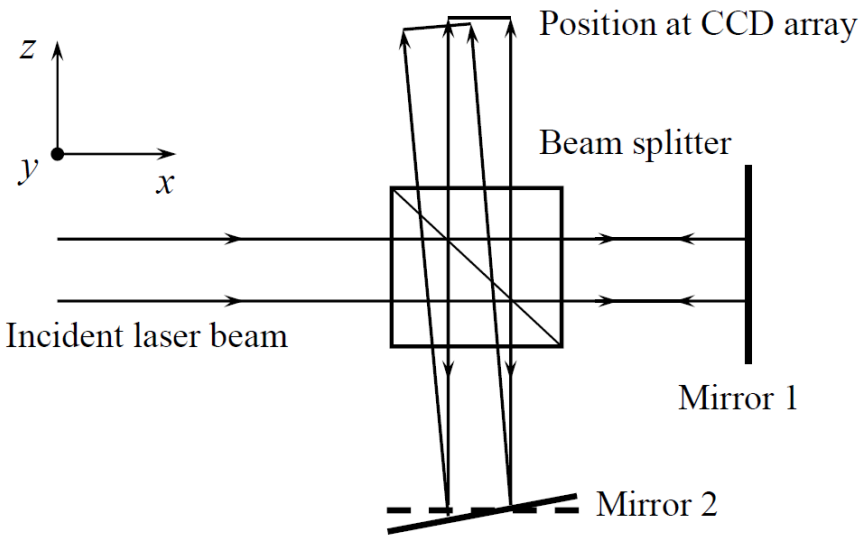

Figure 2.8 Michelson's interferometer for shearography

In general, both DSPI and DSSI both are using laser source and based on speckle pattern interferometers, hybrid dual experimental setups which can be switched between DSPI and DSSI setup were proposed (Bhaduri, 2006). In addition, both methods, provide physical measurements in terms of phase differences. Hence

such hybrid setups also contain features which facilitates easy phase retrieval such as piezoelectric transducers (PZT).

2.3 Review of phase retrieval techniques

2.3.1 Temporal phase retrieval techniques

In interferometry, a physical entity is encoded in the form phase differences due to the difference between optical path lengths of interfering beams. Hence phase retrieval from the recorded intensities, provides quantitative values of the physical entity which cause this phase difference. An intensity map of an interferogram is given by:

$$I(m,n) = A(m,n) + B(m,n)\cos\{\phi(m,n)\} \tag{2.38}$$

where A is the background intensity, B is the amplitude modulation and ϕ is the phase value. These three unknown values especially phase ϕ have fast variations in spatial domain. Hence a slow variation can be introduced along the time t to deduce values for these unknowns. This temporal phase shifting, provides N_t number of phase shifted frames as shown below.

$$I(m,n,t) = A(m,n) + B(m,n)\cos\{\phi(m,n) + \Delta\phi_t\} \tag{2.39}$$

where $\Delta\phi_t$ is the known phase shift that is a constant for all pixels and t represents different phase shifted frames.

There are many such phase retrieval methods available in the literature which use temporal phase shifting, hence only the most common methods are discussed in this review. These temporal phase shifting methods employ phase analysis for each pixel independently. Hence the representation of pixel coordinates is omitted for the

following equations in this section. Since there are three unknowns (A, B and ϕ) in the interferometric equation, we need at least three phase shifted frames to obtain the phase value as in the case of the three frame method (Malacara, 2007; Rastogi, 2015). One of the simplest temporal phase shifting algorithm, called four frame method captures four phase shifted frames with a known phase shift $\Delta\phi_t = \frac{\pi}{2}$ (Malacara, 2007; Rastogi, 2015). The intensity maps for the four frame method is given by:

$$I(0) = A + B\cos\phi \tag{2.41}$$

$$I(1) = A + B\cos(\phi + \pi/2) = A - B\sin\phi \tag{2.42}$$

$$I(2) = A + B\cos(\phi + \pi) = A - B\cos\phi \tag{2.43}$$

$$I(3) = A + B\cos(\phi + 3\pi/2) = A + B\sin\phi \tag{2.44}$$

$$\phi = \arctan\{\frac{I(3) - I(1)}{I(0) - I(2)}\} \tag{2.45}$$

The phase shift between each frame is introduced by a PZT. The phase shifters are prone to calibration errors so the phase shift may contain discrepancies. Hence a five frame method which is less susceptible to the calibration errors is proposed (Schwider, 1983; Rastogi, 2015). The phase shift for the five frame method is also introduced by a PZT and phase retrieval is carried out using the Eq. (2.46):

$$\phi = \arctan\{\frac{2[I(3) - I(1)]}{I(4) + I(0) - 2I(2)}\} \tag{2.46}$$

In addition, Carré's method is proposed to eliminate the influence of calibration error completely using an unknown phase shifting value (Carré, 1966;

Malacara, 2007; Rastogi, 2015). Hence including phase shift, there are four unknowns for four frames of constant phase shift $\Delta\phi_t = \Delta\phi(2t-3)/2$ and the recorded phase is given by the following Eq.:

$$\phi + \frac{3\Delta\phi}{2} = \arctan\left[\frac{s_f\sqrt{[I(0)-I(3)+I(1)-I(2)]\{3[I(1)-I(2)]-I(0)+I(3)\}}}{I(1)+I(2)-I(0)-I(3)}\right] \qquad (2.47)$$

where $s_f = \text{sign}[I(1)-I(2)]$.

In speckle interferometry, we can either record speklegrams before and after loading or we can subtract them to record the correlation fringes. The temporal phase shifting methods which are explained above are called the difference of phases in speckle interferometry as the phase shifted frames are captured before and after loading separately. Furthermore, the difference between the phase values would give the phase difference caused by a physical change. Alternatively, four phase shifted frames before loading can be captured and only one frame at every transient position is captured. The subtraction of a transient frame with four phase shifted reference frames provides four correlated fringe patterns at every transient position. Further processing would provide the phase difference values for each transient position as shown in Fig. 2.9. This method is called the phase difference method and it is most suitable for dynamic measurement as it requires only one frame for each transient position. However, the quality of the phase map obtained from this method is highly affected by speckle noise as is the case for any speckle correlated fringe patterns (Huntley, 2001; Rastogi 2015).

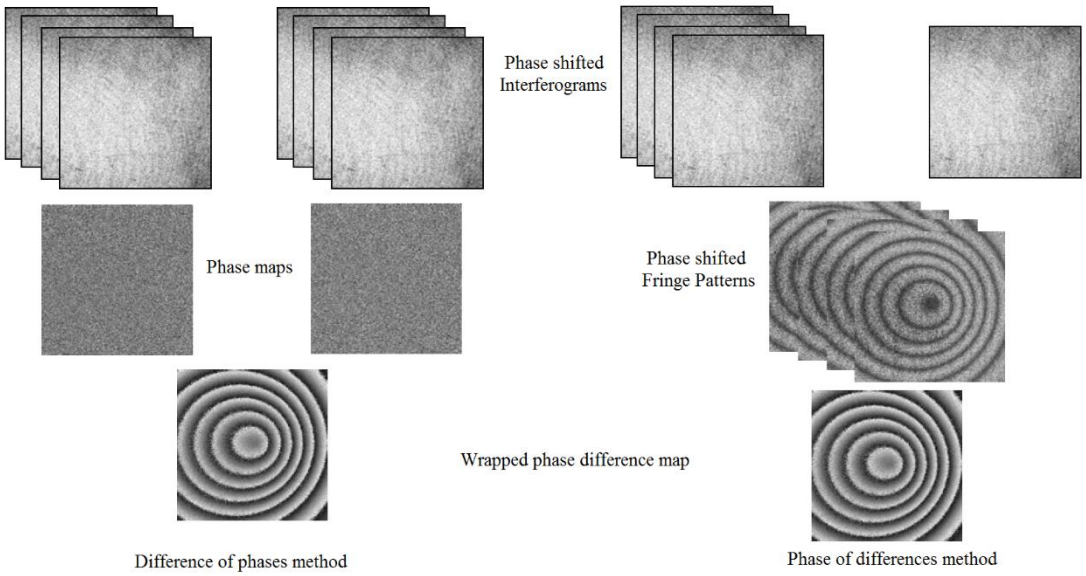

Figure 2.9 Different phase-retrieval methods in phase shifted speckle interferometry

2.3.2 Spatial phase retrieval techniques

In temporal phase retrieval techniques, the phase change that occurs at a single pixel with respect to time or at various states are considered for phase analysis but phase changes that occurred between neighboring pixels are not considered. Hence temporal phase shifting method need more than one frame for phase retrieval which makes the method not suitable for many real time dynamic applications. Spatial phase retrieval method requires only one frame hence they are more suitable for both dynamic and static applications.

Since phase shifting method is widely used for phase retrieval, there are many methods suggested to capture phase shifting within a single frame (Novak et al, 2005; Xie et al, 2013; Wang et al, 2016). These techniques are called spatial phase shifting techniques and in the methods, phase shifted images are recorded simultaneously in a CCD sensor in different quarters of an image plane (Novak et al, 2005; Rastogi, 2015). A conventional phase shifting algorithms are then employed for phase retrieval. Novel

methods, which combine both displacement and displacement derivative measurements are suggested (Xie et al, 2013; Wang et al, 2016). The displacement and displacement derivative information are spatially separated in an image plane using spatial phase shifting technique. The main drawbacks of the spatial phase shifting method are that the spatial resolution of the interferograms is less than temporal phase shifting method and it also requires complex experimental setups to achieve spatial phase shifting.

2.3.3 Phase retrieval using spatial fringe analysis techniques

In many applications, phase difference values in a single fringe pattern vary slowly and continuously since the phase difference vales correspond to a physical entity. Spatial phase retrieval techniques which are applicable only to fringe patterns and utilizes the spatial continuity of phase values are called fringe analysis techniques.

2.3.3.1 Transform based fringe analysis techniques

Fourier analysis method is one of the most famous fringe analysis methods (Takeda et al, 1982). Fourier analysis is simple and effective for sinusoidal open fringes which are space-invariant in nature. However, the fringes obtained from real applications are space-varying and non-stationary. Fourier analysis on such a nonstationary signal results in huge error in the phase values. To overcome this error, researchers proposed various spatial fringe analysis methods such as short time Fourier transform (STFT) also called as window Fourier transform (WFT), continuous wavelet transform (CWT) and Hilbert transform.

In WFT, it has been shown that the use of local windows instead of applying Fourier transform globally can reduce this error to some extent (Qian, 2004; Qian, 2007). The window size in this method is fixed. As fixed window size causes

invariable spatial resolution, it still provides a phase error in non-stationary signals. It is well established that the window size is inversely proportional to the spatial resolution (Zhong and Weng, 2004). Hence a large window should be chosen for a low frequency fringes and a small window should be chosen for a high frequency fringes to obtain more accurate phase values. A dilating Gabor transform with changeable window size is introduced to overcome the phase error issue in non-stationary signals (Zhong and Weng, 2004).

Quan et al, proposed a fringe density estimation method based on continuous wavelet transform and it is used for estimating the variable window size in WFT (Quan et al, 2005; Zhong et al, 2007;). This method combines both CWT and WFT to provide more precise phase values. As WFT methods require high computation time and the accuracy of the phase values are influence by the boundary effects, a modified windows Fourier transform has been suggested (Quan et al, 2010;) This technique employs Gerchberg method to extrapolate the fringe pattern boundaries to reduce boundary effects and employs fast Fourier transform (FFT) instead of convolution method to improve computational speed. A comparison of various spatial fringe analysis techniques using Fourier transform, WFT and CWT are investigated by Huang et al. The effect of noise on all these methods are studied. It has been shown that 2D transform methods has better robustness against noise than their 1D counterparts (Huang et al, 2010).

A common limitation of these methods is that they require a spatial carrier frequency to be introduced into the fringe pattern to overcome sign ambiguity problem in closed fringe patterns. In Fourier domain, fast varying carrier frequencies and slow varying frequencies which represent phase data can be separated easily and the inverse Fourier transform of low frequency data provides the required phase

values. Applying carrier frequency in a fringe pattern is difficult and it requires a complex experimental setup (Takeda et al, 1982; Malacara et al, 1998).

A continuous wavelet transform method which does not require carrier frequency is proposed (Tay et al, 2007). In this method, ridge detection followed by tracking inflexion points is used to determine wrapped phase maps. However, this methods requires prior knowledge of the sign of the surface of the slopes to overcome the sign ambiguity problem. Ma et al, proposed a phase retrieval method based on 2D CWT which overcomes sign ambiguity problem. Ambiguous phase map is determined first using a 2D CWT as they are insensitive to noise and robust to frequency change in fringes. A phase determination rule based on phase continuity and frequency guidance is imposed to obtain accurate phase maps (Ma et al, 2011).

Hilbert transform has also been employed for phase retrieval from a fringe pattern but 1D Hilbert transform still suffers with the sign ambiguity problem (Nakajima, 1988). A novel quadrature transform method which provides 2D Hilbert transform was proposed for phase demodulation of single fringe pattern (Larkin, 2001a; Larkin, 2001b). This method uses vortex operator which is based on a spiral phase operator and a phase orientation map. Vortex operator provides Hilbert transform to determine a complex image from a fringe intensity distribution. Spiral phase operator $\varpi(m,n)$ is a phase only function which is applied to fringes in the Fourier domain while orientational phase operator, which is obtained from an orientation map $\theta(m,n)$, is applied in the spatial domain. Applying spiral phase function in the Fourier domain on a fringe pattern $I(m,n)$ results in fringes which include data of a unique orientation angle map $\theta(m,n)$ and is given by

$$I(m,n) = B(m,n)\cos\{\phi(m,n)\} \tag{2.48}$$

$$F^{-1}[\exp\{j\varpi(m,n)\}F[I(m,n)]] \approx j\exp\{j\theta(m,n)\}B(m,n)\sin\{\phi(m,n)\} \quad (2.49)$$

$$\exp\{-j\theta(m,n)\}F^{-1}[\exp\{j\varpi(m,n)\}F[I(m,n)]] \approx jB(m,n)\sin\{\phi(m,n)\} \quad (2.50)$$

where $j=\sqrt{-1}$. The vortex operator based 2D quadrature transform solves effectively without any need for carrier frequency. However, orientation map of the fringe pattern has to be determined for phase retrieval.

2.3.3.2 Image processing based fringe analysis techniques

Apart from the transform based fringe analysis techniques, image processing based fringe analysis techniques such as fringe tracking method, extreme map based method, sign map based method, phase tracker method, etc. are suggested for phase demodulation. These methods do not require more than one fringe pattern or carrier frequency or complex experimental setup for phase retrieval.

Fringe tracking method or skeleton method retrieves phase by detecting the local maxima and minima of the fringe intensities which corresponds to 2π periodic function's maxima and minima. This method is focused on reproducing the manual fringe counting method. Various methods for 2D tracking of these local extrema are proposed (Malacara et al, 1998; Sharpe, 2008). Quan et al suggested a method which uses adaptive weighted filters which reduces the noise and enhances the contrast for determining extreme maps. This method does not require fringe ordering and interpolating fractional fringe order (Quan et al, 2005). Local directional computing windows has been suggested to overcome high speckle noise problem in fringe tracking (Yang et al, 2009). This method calculates the gradient map from the filtered

image, from which the sign map and skeleton can be obtained robustly. Sign map helps to overcome the sign ambiguity problem.

All the phase retrieval techniques, discussed in this review thus far from temporal phase shifting to image processing based fringe analysis techniques have one common limitation, they can only provide a wrapped phase map. A separate phase unwrapping algorithm is necessary to determine actual phase values (Malacara, 2007; Rastogi 2015). Detailed analysis of various phase unwrapping techniques are discussed later in this chapter.

Regularized phase tracking (RPT) method is also an image processing based fringe analysis technique which can provide unwrapped phase and phase derivative maps directly from a single fringe pattern (Servin et al, 1997). This method retrieves phase from single open and closed fringe patterns without any need for carrier frequency. As the name suggests, this method tracks phase continuously in the fringe pattern and phase maps with discontinuity cannot be solved using this method. In RPT, phase demodulation is carried out by minimizing a cost function with respect to phase $\phi'(m,n)$, and phase derivatives $\phi_x(m,n)$ and $\phi_y(m,n)$ as shown in the equations below.

$$U(m,n) = \sum_{(\varepsilon,\eta)\in M_w} \{[\bar{I}(\varepsilon,\eta) - \cos\{p(m,n,\varepsilon,\eta)\}]^2 + \beta_{reg}[\phi'(\varepsilon,\eta) - p(m,n,\varepsilon,\eta)]^2 s(m,n)\} \tag{2.51}$$

$$p(m,n,\varepsilon,\eta) = \phi'(m,n) + \phi_x(m,n)\{m-\varepsilon\} + \phi_y(m,n)\{n-\eta\} \tag{2.52}$$

where $M_w(m,n)$ is a neighborhood region or a selected window, $s(m,n)$ is a status map to indicate whether a phase at a particular pixel has been determined and β_{reg} is a

constant regularizing parameter to control the smoothness of the estimated phase map $\phi'(m,n)$; $\phi_x(m,n)$ and $\phi_y(m,n)$ are estimated local frequencies along the x and y directions respectively. These local frequencies represent the phase derivatives in the x and y direction respectively. In the RPT method, phase derivatives are also determined along with phase values. Hence the minimization of the cost function requires more computation time (Kai et al, 2013). Conventional RPT method's phase reconstruction accuracy drops around the saddle points of the fringe pattern. Techniques such as fringe-following regularized phase tracker, path independent regularized phase tracker, generalized regularized phase tracker and improved generalized regularized phase tracker have been proposed to overcome RPT's limitations (Servin et al, 1997; Servin et al, 2001; Tian et al, 2010; Kai et al, 2012; Kai et al 2013).

In fringe follower RPT, a scanning strategy is employed to improve the robustness of the phase tracker method. The bright regions of the fringe patterns are solved first for phase values to improve the accuracy of the detected phase values. It is shown that powerful combination of fringe following and RPT enables this technique to demodulate complex single interferograms successfully (Servin et al, 2001). As fringe follower method is a path dependent, path independent phase demodulation methods are proposed (Estrada et al, 2006; Tian et al, 2010). In these methods, phase demodulation is carried out with estimations within function space C(2) i.e., estimations where the curvature is continuous. This method estimates the frequency and second order potential regularizer to force demodulation to look into curvature space (Estrada et al, 2006). A variant of this method which uses paraboloid phase model to obtain the smoothest second order derivative is proposed (Tian et al, 2010).

These path independent methods provide better robustness against noise and complexity of the interferograms than the conventional RPT.

As the conventional, fringe follower and path independent RPT methods require normalized fringe pattern for phase demodulation, pre-processing of fringe patterns is necessary. Generalized regularized phase tracker (GRPT) method is proposed to demodulate any fringe pattern without preprocessing (Kai et al, 2012). In this method, the cost function of the RPT is modified to include linear background, linear modulation and a quadrature phase to obtain general local fringe model and number of iterations for minimizing the cost function is determined based on the fringe quality. These two modifications provide better robustness against noise and guides the phase demodulation process near saddle points. An improvement on GRPT (iGRPT) method is proposed which employs changeable window size based on fringe frequency (Kai et al, 2014). It is shown that iGRPT improves the demodulation capabilities of GRPT by incorporating a background regularization tern and modulation regularization term in cost function. In general RPT methods are the most famous and robust methods among fringe analysis methods but they require more computation time than other fringe analysis techniques. The RPT variants are proposed to address various limitations of conventional RPT such as robustness against noise, dealing with frequency change and saddle points. However they all increase computation time further.

2.3.4 Phase derivative determination techniques

Phase derivatives determination is also an important task in experimental mechanics, since displacement derivatives such as slope, curvature and twist maps are directly related to physical entities strain, flexural rigidity and torsional rigidity of the

object respectively. Hence phase derivatives too have lot of applications such as material characterization, quality assessment, fault identification etc. In many applications, the phase values can be determined and subsequent differentiation can be employed for phase derivatives determination. However, this direct differentiation method is not preferred as it is susceptible to the phase unwrapping and numerical differentiation methods are highly sensitive to noise.

Phase tracker methods (RPT) are one of the very few phase retrieval techniques available in the literature which provides phase derivatives as a byproduct from the phase demodulation of a single fringe pattern. As mentioned in section 2.2.1, many methods for phase derivatives determination have been suggested in DHI from a complex amplitude field. However, for other interferometric techniques, a phase retrieval technique such as phase shifting or carrier frequency method has to be implemented so that these phase determination methods can be employed (Qian et al, 2003; Rajshekhar et al, 2009).

There are few direct phase derivatives methods suggested in the literature, which determines the phase derivatives from single fringe patterns. Sciammerella et al proposed direct strain or frequency modulations from fringe patterns (Sciammerella et al, 2003; Sciammerella et al, 2005). It is shown that the space-frequency representation of a fringe signal can be used to obtain the instantaneous frequency of the fringe patterns. The method showed extracting strain from fringe patterns using STFT or wavelets (Sciammerella et al, 2003). An extension of the method to two dimension transforms is proposed to improve robustness against noise (Sciammerella et al, 2005). It is shown that accuracy of phase derivatives estimation can be improved by employing Wigner-Ville distribution with smoothing Gaussian kernels than using continuous wavelets (Federico et al, 2003). Similarly, Tay et al suggested phase

derivative determination using wavelet ridges directly from a single fringe pattern (Tay et al, 2007). Recently, Kalman filter based phase derivatives determination algorithms from a single fringe pattern has been proposed (Kulkarni et al, 2016).

2.4 Review of optical techniques in vibration analysis

2.4.1 Mode shape visualization

Modal analysis provides natural frequencies and frequency modes of a structure and is helpful in safe design and in determining material properties such as stiffness and damping coefficients. Traditionally mode shape visualization is carried out by Chladni patterns, which is a simple and cost effective method. However in certain cases like curved surfaces, this technique is not effective (Molin, 2007). Optical techniques such as holographic interferometry, DSPI and DSSI are employed for experimental modal analysis since they are highly sensitive non-contact full field measurements (Løkberg, 1984). Especially the time average methods which record interference patterns at a lower frequency than the vibrating object can provide real time mode visualization even for objects vibrating at very high frequencies. Time average holographic interferometry (TA-HI) and time average digital speckle pattern interferometry (TA-DSPI) methods can provide both the mode shape and quantitative amplitude measurement. Time average digital speckle shearing interferometry (TA-DSSI) is used to obtain the vibration strains of an object from fringe patterns.

One of the major problems in time average method is the poor quality of the fringes obtained and consequently, it affects both the mode shape visualization and amplitude measurement. The equation for time average interferometer intensity is given by:

$$I_{avg} = I_0[1+V\cos\phi_r J_0\{\phi\}] \tag{2.53}$$

$$\phi = A_v \frac{4\pi}{\lambda} \tag{2.54}$$

where ϕ_r is the speckle phase, ϕ is the phase caused by vibrational amplitude A_v and J_0 is a zero order Bessel function of the first kind. As mentioned above, the Bessel function is not visible due to the influence of the bias intensity, visibility and speckle.

Various techniques have been reported to improve the fringe contrast by subtracting a time-average frame from a stationary reference frame (conventional subtraction method), a time-average phase shifted reference frame, a time-average force varied reference frame, and a refreshing reference frame (Nakadate, 1986; Pryputniewicz and Stetson, 1989; Wong et al, 1997; Wong et al, 1998; Davies et al, 1987). Phase shifting technique requires a phase shifter to produce a high contrast fringe pattern (Nakadate, 1986). Wong et al, have shown that the subtraction of two time-average frames with different force levels of harmonic excitation improves the fringe contrast (Wong et al, 1997). In the refreshing reference frame technique, each frame is phase shifted and subtracted with a previous frame (Davies et al, 1987). This real time subtraction further improves the visibility of the recorded fringe pattern since ambient disturbances are suppressed. However, the method also requires a phase shifter to improve the fringe contrast.

2.4.2 Vibration amplitude measurement

A phase retrieval method provides quantitative vibration amplitude using TA-DSPI interferograms. However, the existing phase retrieval techniques are only suitable for cosine fringe patterns with good fringe contrast. Hence most of the methods suggested for vibration amplitude measurement assume Bessel fringes as cosine fringes.

Pryputniewicz et al, proposed a method which introduces a vibration in an illuminating beam to obtain a good contrast fringe pattern and phase shifting method is used to determine the vibration amplitude (Pryputniewicz and Stetson, 1989). This technique requires more than one fringe pattern and a complex experimental setup. Wong et al also proposed a method to measure the amplitude based on Hilbert transform but due to sign ambiguity, the method is only applicable to open fringe patterns (Wong et al, 1998). A novel method is proposed to overcome the limitation as it uses predetermined mask to correct sign ambiguity problem (Kumar et al, 2010). The technique is difficult to apply to a complex mode shape and also requires a phase shifter. Fringe analysis technique can be employed for phase retrieval from a single fringe pattern as discussed earlier. However, the technique requires good fringe contrast and a high computation time.

2.5 Phase unwrapping

Phase maps obtained from most phase retrieval techniques are wrapped between $-\pi$ to π. The process of determining a continuous phase map which represents a physical parameter from a 2π-modulo phase map is called phase unwrapping. To obtain the phase values from the wrapped signal, 2π value is either added or subtracted from the pixels adjacent to a phase jump. However due to the presence of noise, discontinuities and under sampled data (violation of Shannon's law), this process is not as straight forward as simple addition or subtraction at phase jumps. Numerous phase unwrapping techniques have been proposed (Ghiglia et al, 1998) and all the methods have their own advantages and disadvantages. Hence there is no one solution that fits all the phase unwrapping problems (Robinson et al, 1993). Phase unwrapping

methods are mainly classified into three different groups such as minimum norm, branch-cut and network flow methods.

The minimum-norm method formulates a phase unwrapping problem into a minimization problem. A least square approach is used to minimize the fitting error where the algorithm seeks a phase function with path independent continuous unwrapped phase derivatives which has values close to the wrapped phase gradient (Servin et al, 1998).

Branch-cut and network flow methods use residues created due to noise and physical discontinuities for phase unwrapping. A positive and negative residue pair mark a region having a phase discontinuity. Integrating the phase values through the region provides erroneous phase maps (Goldstein et al, 1988; Buckland et al, 1995). The network flow method also uses the residue approach. In this method a high cost is assigned to regions marked by the residuals. The method calculates a flow with the minimal cost to find a path which crosses the least amount of discontinuities. Further, a flood-fill method i.e. an integration of phase values guided by the obtained path is carried out for phase unwrapping (Buckland et al, 1995).

The branch-cut is one of the most simplistic and effective phase unwrapping approach. It uses barriers or branch-cuts to prevent integration through those barriers during the unwrapping process instead of assigning cost for the discontinuities as in the case of the network flow method. The branch cuts cover the noisy and discontinuous regions in a phase map where a straight forward unwrapping should not be employed. Hence the determination of branch cuts becomes an important step in this method. Goldstein branch-cut algorithm is a classic branch-cut algorithm which determines the minimum cut length to prevent path integration from crossing these cuts (Goldstein et al, 1988). Subsequently, many branch-cut algorithms have been

proposed to find the global optimum in minimization of total cut length such as the Nearest Neighbor Algorithm, the Modified Nearest Neighbor Algorithm, Hybrid Genetic Algorithm (HGA), Simulated Annealing (SA), Reverse Simulated Annealing (RSA) and discrete Particle Swarm Optimization method (dPSO) (Karout et al, 2007; Gutmann and Weber, 2000; Gutmann and Weber, 1999; He et al, 2012). The nearest neighbor and modified nearest neighbor algorithms are local heuristic search algorithms. They are effective but will not find the global optimum. This gives long branch-cuts and less smooth unwrapped phase map. Other artificial intelligence (AI) methods used for solving phase unwrapping such as SA and RSA are slow compared to local heuristic search. Genetic algorithm (GA) outscores all AI methods due to memory factor (chromosomes). HGA is faster than GA since it uses local search for the population initialization (Karout et al, 2007).

2.6 Summary

Various optical techniques from DHI to DSSI have been employed to extract the surface displacement and its derivatives measurement. The optical hardware of these techniques are well evolved and innumerous experimental variants are suggested to overcome different limitations in different applications. Recent improvements in optical hardware for improving measurement accuracy and robustness against noise require highly sophisticated equipment. Hence they are more expensive, complicated and extremely difficult to employ outside laboratory conditions.

In last two decades, due to comprehensive improvement in computation facilities, many researchers are developing algorithmic solutions to enhance and to overcome classical challenges in optical techniques. These algorithmic improvements facilitate

experimentalists to minimize the complexity in the hardware employed and provides ease in carrying out experiments even outside laboratory conditions.

In DHI, a complex field is obtained directly from a single hologram and phase maps can be easily determined from the complex field. However, the phase derivatives determination is not straight forward in DHI. Phase derivatives determination methods suggested in literature are highly sensitive to speckle noise, requires more computation time and they also can only provide wrapped phase derivatives maps.

In speckle pattern interferometry techniques, the optical hardware is less sensitive to environmental disturbances which make them an ideal candidate for real applications from stress, strain measurement to defect detection. The phase shifting methods are the most famous and robust techniques for the full field phase measurement, but they need more than one fringe pattern. In dynamic measurements, only one fringe pattern can be captured for every deformation state and it is necessary to retrieve phase values from single fringe patterns. Spatial fringe analysis techniques provides solution to this problem. However, most of the transform based fringe analysis techniques require carrier frequency for solving the sign ambiguity problem in phase retrieval. Image processing based fringe analysis techniques neither need carrier frequency nor more than one fringe pattern for phase retrieval. Regularized phase tracker methods are more robust and famous fringe analysis techniques which also have an additional advantage that they provides unwrapped phase maps directly. However, they take high computation time and have limited accuracy near saddle points. Variants of RPT methods provide solution for improving phase accuracy but they require even more computation time than conventional RPT.

Direct phase derivatives determination from single fringe pattern provides valuable physical measurements such as strain, flexural and torsional rigidity. Space-frequency analysis on fringe patterns to obtain instantaneous frequencies are suggested for strain measurement. Comparatively, very little research have been carried out in direct phase derivatives measurement from single fringe pattern and there is a lot of scope for further exploration.

Time average methods are proved to be an excellent choice for experimental modal analysis. The mode shape visualization and natural frequency determination are carried out simultaneously using time average methods. However, complex experimental setups and phase shifters are required to obtain good quality fringes. In phase unwrapping methods, various techniques are proposed in literature for solving various challenges in different applications. Recently, many AI based solutions for phase unwrapping problems are investigated. It is shown that these methods are more robust against noise than conventional phase unwrapping methods.

CHAPTER THREE

DEVELOPMENT OF THEORY

Theoretical development of the proposed methods are organized in five sections corresponding to chronological order of the various stages of optical measurements. The first step of any optical measurement method is to obtain high quality interferograms or fringe patterns from an experimental setup. Hence in the first section of this chapter, a theoretical development of an experimental approach to improve the fringe contrast in TA-DSPI is presented. An empirical mode decomposition method for pre-processing of fringe pattern in a fringe analysis is also discussed. In section 2, fringe analysis techniques for determination of phase derivatives such as a phase derivative measurement from a complex amplitude signal using Teager operator and a direct phase derivative from a single fringe pattern are presented. In section 3, development of a derivative based regularized phase tracker (DRPT) method and its advantages over conventional regularized phase tracker (RPT) method is presented. A derivation for quantitative amplitude measurement from a TA-DSPI fringe, which is obtained from the proposed experimental approach, is presented as well. In section 4, a phase unwrapping technique for unwrapping noisy fringe pattern using an artificial intelligence technique called ensemble of hybrid genetic algorithm is presented. In section 5, a method to determine material properties of a cantilever beam using DSPI is presented.

3.1 Fringe quality improvement

3.1.1 Amplitude-varied refreshing reference frame technique in TA-DSPI

The amplitude A_v of a harmonically excited vibrating object is related to the amplitude A_e of the harmonic excitation, which excites the object is given by

$$A_v = \frac{A_e\sqrt{\{1+(2\varsigma\omega/\omega_n)^2\}}}{\sqrt{\{(1-\omega^2/\omega_n^2)^2+(2\varsigma\omega/\omega_n)^2\}}} \tag{3.1}$$

where ς, ω and ω_n are the damping coefficient, vibrating frequency and nth mode resonant frequency. Hence an increase in the amplitude A_e of the harmonic function increases the amplitude A_v and the relation is influenced by dynamic properties of the structure.

In the time average method, an interference pattern is captured at a lower frequency than the vibrating object and the equation of the recorded intensity I_{avg} is given by

$$I_{avg} = I_0(1+V\cos(\phi_0-\phi_r)J_0(\Omega)) \tag{3.2}$$

where I_0 is the bias intensity, V is the visibility and J_0 is a zero order Bessel function of the first kind and Ω is a fringe locus function given by $\Omega = A_v\left(\frac{4\pi}{\lambda}\right)$. The phase difference $(\phi_0-\phi_r)$ between the reference and object waves results in a speckle pattern. As mentioned above, the Bessel function is not visible due to the influence of the bias intensity, visibility and speckle. In the stationary reference phase method, a time average frame is subtracted with a reference frame when the object is in rest. The intensity of the reference frame is given by

$$I_s = I_0(1+V\cos(\phi_0 - \phi_r)) \tag{3.3}$$

Subtracting Eq. (3.2) from Eq. (3.3):

$$I_s - I_{avg} = I_0 V\cos(\phi_0 - \phi_r)[1 - J_0(\Omega)] \tag{3.4}$$

Since the Eq. (3.4) is purely modulated by a Bessel function, the fringe pattern is visible but with a poor fringe contrast for high phase values. Any ambient disturbances will also affect the quality of the fringes. The present study attempts to address these two problems using an amplitude-varied refreshing reference frame. Refreshing reference frame techniques, which are suggested previously, require a phase shifting between every other frame to achieve better contrast. However, in the proposed method, a phase shift is not necessary. A small amplitude change between every other frame provides a good fringe contrast. This could be easily achieved by slowly varying the amplitude of harmonic excitation with a function generator because an amplitude variation in harmonic excitation causes an amplitude change in vibrating object. The intensity of the fringe pattern recorded is given by

$$I_{avg0} - I_{avg1} = I_0 V\cos(\phi_0 - \phi_r)[J_0(\Omega) - J_0(\Omega+\Delta\Omega)] \tag{3.5}$$

where $\Delta\Omega$ is a small change in fringe locus function triggered by a small change in the harmonic excitation. The increment in the amplitude $\Delta\Omega$ is given as a factor of the original amplitude Ω i.e. $\Delta\Omega = r \cdot \Omega$, where r is the factor of the increment. This is achieved by increasing the amplitude of the harmonic excitation A_e by the factor r. The value for the factor r should be small enough to not distort the fringe pattern. A detailed discussion for selecting

the proper value for r after analyzing the influence of r in the improvement of fringe contrast is presented in section 5.1.1.

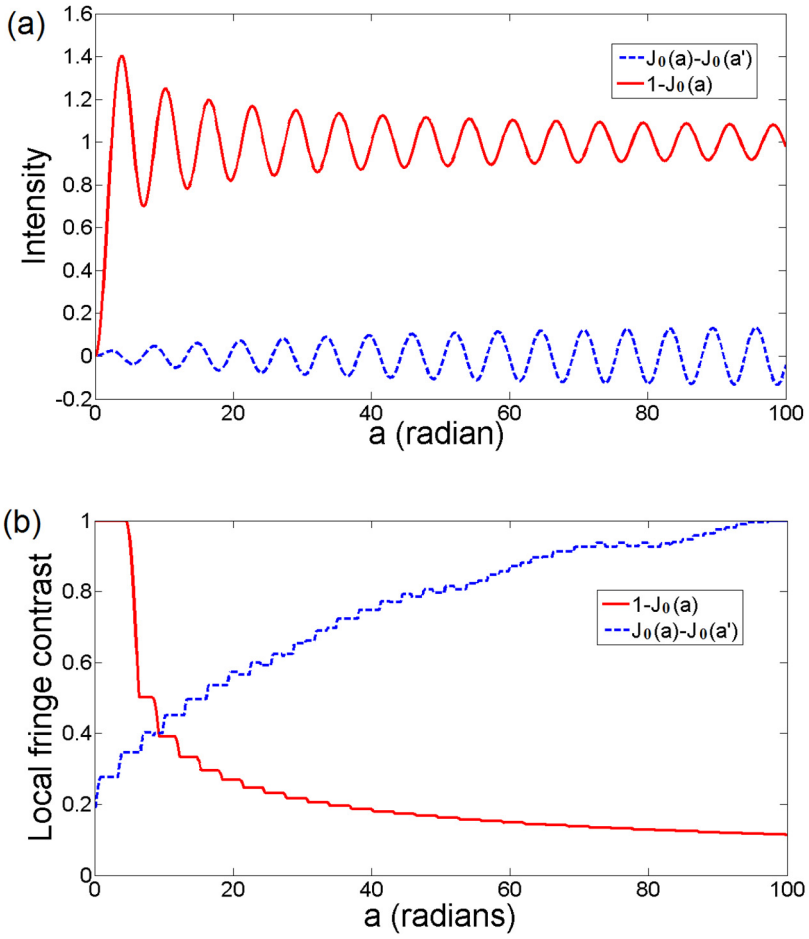

Figure 3.1(a) Comparison of fringe intensity between the conventional and proposed method; (b) Comparison of fringe contrasts between the conventional and proposed method.

Figure 3.1(a) illustrates a comparison between intensity of a one dimensional (1D) fringe pattern obtained from conventional subtraction method and intensity of a 1D fringe pattern obtained from the proposed method with r value of 5%. Figure 3.1(b) shows the variation in fringe contrast of the fringe patterns. The contrast of the fringes obtained from conventional subtraction method decreases significantly for the first few fringes. The last fringe has just one tenth of the fringe contrast of the first fringe. The contrast of the fringes obtained from the proposed method increases steadily with the phase values and the fluctuation between

two adjacent fringes is small. As seen in Fig. 3.1(b) each fringe pattern has better contrast and is more visible especially at higher phase compared to the conventional subtraction method.

3.1.2 Empirical mode decomposition for fringe normalization

Huang et al. proposed an empirical mode decomposition method (EMD) for analyzing non-linear and non-stationary signals (Huang et al, 1998). The signals are decomposed into intrinsic mode functions (IMF), which provide instantaneous frequencies and amplitudes with either a Hilbert or Teager spectrum (Huang et al, 1998; Boudraa et al, 2004). The empirical mode decomposition utilizes signal data more effectively and is adaptive. Hence the method is more effective than wavelet transform (WT). In addition to this advantage, the method also eliminates the DC term from the signal. Trusiak et al. proposed another novel 2D EMD method called enhanced fast empirical mode decomposition (EFEMD). It is based on an automatic selective reconstruction (ASR) to normalize the fringe pattern and requires little computation time for decomposition of the fringes (Trusiak et al, 2014).

Empirical mode decomposition is a technique used to decompose a signal into a collection of intrinsic mode functions (IMFs). Decomposition of the signals is carried out by a process called sifting. In the sifting process, an upper and lower envelope of the signal is first determined by fitting all its local maxima and minima. The mean of the envelopes provides the first IMF of the signal. The difference between the original signal and the first IMF provides the residue signal and further IMFs are obtained from the residue signal by iterations. The sifting process continues till the residue becomes a monotonic function from which no IMF could be retrieved. Once all the IMFs are obtained, the instantaneous frequency of each IMF is easily obtained in either Hilbert or Teager spectrum. Unlike Fourier or Wavelet analysis, this technique does not have any predefined decomposition basis and is purely adaptive.

Enhanced fast empirical mode decomposition is a two dimensional EMD for normalizing a fringe pattern. In EFEMD, envelopes are determined using morphological operations instead of surface fitting to reduce computation time. Some Intrinsic mode functions obtained by decomposition, contain useful signals while others contain unwanted data such as carrier, noise, etc. Hence to normalize a fringe pattern, IMFs which contains background variation and speckle noise need to be discarded. It is also possible that high contrast fringe data are present together with low contrast noises. Automated selective reconstruction (ASR) is employed to separate the signal from the noises before reconstruction. The ASR process determines the intensity modulation distribution pixel by pixel and a weighted map is assigned on each selected IMF for reconstruction. Since the process is completely automated, the computation time is greatly reduced (Trusiak et al, 2014).

A fringe pattern's intensity field $I(m,n)$ can be expressed by:

$$I(m,n) = \left| A(m,n) + B(m,n)\cos\{\phi(m,n)\} + \eta(m,n) \right| \tag{3.6}$$

where $A(m,n)$ is a background variation, $B(m,n)$ is a local amplitude, $\phi(m,n)$ is a phase value and $\eta(m,n)$ is a speckle noise. ASR-EFEMD process is used to normalize the fringe pattern to remove the background variation (DC term), local amplitudes and speckle noise. The EFEMD decomposes the fringe pattern into K number of intrinsic mode frequencies (IMF).

$$I(m,n) = \sum_{i=1}^{K} IMF_i + Residue \tag{3.7}$$

As mentioned earlier, these IMFs represent image features at various spatial scales. General strategy for normalization of the fringes is carrying out a band pass filtering i.e., first

few IMFs which represent high frequency speckle noise and several last IMFs along with the residue which represent low frequency background noise and bias term are removed before reconstruction. Manually selecting IMFs for reconstruction takes more time and is prone to error. Apart from that, each IMF contains two regions, sharply extracted fringes and noise, which makes IMFs selection more complex.

In ASR method, amplitude modulation maps for each IMF is determined using Hilbert spiral phase transform and these amplitude modulation maps have values from 0 to 1, which represents the weightage of signal quality. Performing weighted averaging on IMFs with modulation maps as weights provides a normalized fringe pattern. The fringe pattern I_r after reconstruction is given by:

$$I_r(m,n) = \cos\{2\phi(m,n)\} \tag{3.8}$$

Since the fringe pattern's intensity $I(m,n)$ is the magnitude of a cosine signal, after normalization using ASR-EFEMD, the phase value of the cosine signal would be doubled as shown in Eq. (3.8).

3.2 Phase derivatives determination

3.2.1 Phase derivatives from complex amplitude using Teager operator

In digital holographic interferometry (DHI), complex phasors method provides high quality wrapped phase maps (Chen et al, 2008). However this method requires filtering techniques such as sine-cosine filter and short time Fourier transform (STFT) for determining high quality phase derivative maps. Hence it takes high computational time

and can provide only wrapped derivative maps. Since the strain, curvature and twist measurements are of more interest than displacement measurement, various phase derivatives measurement methods are proposed (Quan et al, 2009; Rajshekhar and Rastogi, 2011; Kulkarni and Rastogi, 2014).

3.2.1.1 Instantaneous frequency determination from a 2D signal

Maragos et al. proposed a discrete energy separation algorithm (DESA) based on Teager-Kaiser energy operator (TKEO) which provides instantaneous frequencies of a nonlinear and non-stationary signal (Maragos et al, 1993). The instantaneous frequency of a signal at a given point is equal to the phase derivative and it is obtained using amplitude-frequency demodulation methods (Huang et al, 1998; Boudraa et al, 2004; Kulkarni and Rastogi, 2014). Diop et al. proposed a discrete higher order image demodulation algorithm (DHODA) based on higher order TKEO for amplitude-frequency estimation (Diop et al, 2009). It is shown that the DHODA is more efficient in tracking the most significant part of the images so DHODA outperforms DESA by achieving lower error values than DESA (Diop et al, 2009).

Higher order image demodulation algorithm is based on 2D higher order TKEO, which tracks energy and identify instantaneous amplitude and frequency in an image. In general, the amplitude component indicates texture contrast and frequency component indicates texture orientation. However, instantaneous frequency also represents the phase derivative of a fringe pattern. In the proposed method, DHODA is used to estimate phase derivatives from a 2D cosine fringe pattern. A 2D discrete cosine signal $g(m,n)$ with amplitude $A_c(m,n)$ and frequencies $\Omega_x(m,n)$ and $\Omega_y(m,n)$ w.r.t. x and y direction is shown in Eq. (3.9) and a higher order TKEO for the discrete signal is shown in Eq. (3.10).

$$g(m,n) = A_c(m,n)\cos\{m\Omega_x(m,n) + n\Omega_y(m,n)\} \tag{3.9}$$

$$\begin{aligned}\Psi_2\{g(m,n)\} = [2\cdot\{g(m,n)\}^2 - g(m-1,n)g(m+1,n) \\ - g(m,n-1)g(m,n+1)] + 2[g_1(m,n)g_2(m,n) - g(m,n)g_{12}(m,n)]\end{aligned} \tag{3.10}$$

where $g_1(m,n)$, $g_2(m,n)$ and $g_{12}(m,n)$ represents discretized partial derivatives $\frac{\partial g}{\partial x}$, $\frac{\partial g}{\partial y}$ and $\frac{\partial^2 g}{\partial x \partial y}$ in the x, y and xy directions respectively. In Eq. (3.10), the first term represents the 2D extension of TKEO. This term is just a 1D TKEO extended to horizontal and vertical axes and it does not consider the other directions, such as diagonals. Hence Boudraa et al, included the second term in this 2D higher energy TKEO operator (Boudraa et al, 2005). Diop et al, derived DHODA algorithm for obtaining amplitude and frequency modulations (AM & FM) estimates based on this 2D higher energy TKEO operator (Diop et al, 2009). In DHODA, the instantaneous frequency Ω_x in the horizontal direction, which is the partial derivative of phase $(m\Omega_x(m,n) + n\Omega_y(m,n))$ in the x direction, is given by:

$$\Omega_x(m,n) = \arccos(1 - \sqrt{\Psi_2\{g_{12}(m,n)\} / \Psi_2\{g_2(m,n)\}}) \tag{3.11}$$

Similarly, the instantaneous frequency Ω_y in the vertical direction, which is the partial derivative of phase $(m\Omega_x(m,n) + n\Omega_y(m,n))$ in the y direction, is given by:

$$\Omega_y(m,n) = \arccos(1 - \sqrt{\Psi_2\{g_{12}(m,n)\} / \Psi_2\{g_1(m,n)\}}) \tag{3.12}$$

Since TKEO uses a few samples for the energy calculation, it has a better time resolution than the Hilbert transform and also requires relatively less computation time.

3.2.1.2 Phase derivatives determination in DHI

Instantaneous frequency determination methods requires high frequency carriers in the signal. To implement DHODA method for phase derivatives retrieval for optical coherent techniques, a carrier frequency should be introduced into the interferograms captured. However, introducing a high frequency carrier needs a complex experimental setup. To achieve this with a simple experimental setup, a high frequency carrier is introduced carried out digitally (Kulkarni and Rastogi, 2014) and it requires a complex amplitude of the signal. Since it is difficult to add phase to a cosine function, this cannot be done directly on a cosine fringe pattern.

In DHI, the complex phasor method provides the complex amplitude of the phase difference map. Hence this method can be employed directly in DHI. A complex amplitude signal obtained from the complex phasor method is given by

$$CP(m,n) = a'(m,n)\exp\{j[\varphi(m,n)]\} \tag{3.13}$$

where $CP(m,n)$ is a complex amplitude and a' is a slow varying amplitude which can be removed by high pass filtering.

$$CP_f(m,n) = \exp\{j[\varphi(m,n)]\} \tag{3.14}$$

Carrier frequencies w_{cx} and w_{cy} are then added to the complex signal CP_f .

$$CP_{cf}(m,n) = CP_f(m,n)\exp[j\{mw_{cx} + nw_{cy}\}] \tag{3.15}$$

$$CP_{cf}(m,n) = \exp[j\{\varphi(m,n) + mw_{cx} + nw_{cy}\}] \tag{3.16}$$

$$CP_{cf}(m,n) = \exp\{j\Phi(m,n)\} \tag{3.17}$$

$$\Phi(m,n) = (\varphi(m,n) + mw_{cx} + nw_{cy}) \tag{3.18}$$

The real part of the complex image CP_{cf} would give the required cosine fringes with a carrier frequency.

$$g(m,n) = \mathrm{Re}\{CP_{cf}(m,n)\} = \cos\{\Phi(m,n)\} \tag{3.19}$$

To obtain phase derivatives in both directions, DHODA is applied on the cosine fringes as shown below.

$$g(m,n) = \cos\{\Phi(m,n)\} \tag{3.20}$$

The following equations show instantaneous frequencies in the horizontal and vertical directions of the cosine signals and are obtained by DHODA using 2D higher order TKEO:

$$\dot{\Phi}_x(m,n) = \arccos[1 - \sqrt{\frac{\Psi_2\{g_{12}(m,n)\}}{\Psi_2\{g_2(m,n)\}}}] \tag{3.21}$$

$$\dot{\Phi}_y(m,n) = \arccos[1 - \sqrt{\frac{\Psi_2\{g_{12}(m,n)\}}{\Psi_2\{g_1(m,n)\}}}] \tag{3.22}$$

$$g_1(m,n) = \frac{g(m+1,n) - g(m-1,n)}{2} \tag{3.23}$$

$$g_2(m,n) = \frac{g(m,n+1) - g(m,n-1)}{2} \tag{3.24}$$

$$g_{12}(m,n) = \frac{g_2(m+1,n) - g_2(m-1,n)}{2} \tag{3.25}$$

$$\dot{\varphi}_x(m,n) = \{\dot{\Phi}_x(m,n) - w_{cx}\} \tag{3.26}$$

$$\dot{\varphi}_y(m,n) = \{\dot{\Phi}_y(m,n) - w_{cy}\} \tag{3.27}$$

Equations (3.26) and (3.27) provide the first derivatives of the phase map $\varphi(m,n)$ in both *x* and *y* directions. Since Eqs. (3.21) and (3.22) contain a square root and an arccosine function, the first derivatives $\dot{\Phi}_x$ and $\dot{\Phi}_y$ are valid only for values between 0 and $\pi/2$. It is assumed that the phase $\varphi(m,n)$ is slow varying compared to carrier frequencies so at each pixel the value of $\dot{\varphi}_x(m,n)$ and $\dot{\varphi}_y(m,n)$ are less than w_{cx} and w_{cy} respectively. Hence the values of the carrier frequencies w_{cx} and w_{cy} are set at $\pi/4$.

Due to the high noise sensitivity of DHODA, even a very small amount of noise would affect the phase derivative values. A 2D median low pass filter is thus applied on the phase derivatives to smoothen out large deviations caused by DHODA. A median filter is chosen to remove the spikes in the phase derivatives without affecting the adjacent pixels and a least square B-spline fitting interpolation function is subsequently applied to smoothen the phase derivatives map $\dot{\varphi}_{xf}$ and $\dot{\varphi}_{yf}$. Furthermore, the second order phase derivatives $\ddot{\varphi}_{xx}$, $\ddot{\varphi}_{yy}$ and $\ddot{\varphi}_{xy}$ can be obtained by employing DHODA using the previously determined first derivatives as shown below.

$$CP_x(m,n) = \exp\{j\dot{\varphi}_{xf}(m,n)\} \tag{3.26}$$

$$CP_y(m,n) = \exp\{j\dot{\varphi}_{yf}(m,n)\} \tag{3.27}$$

3.2.1.3 Phase derivatives determination using DHODA in DSPI

As mentioned previously, DHODA cannot be applied directly on a cosine fringe and it is also highly sensitive to noise. Since a fringe pattern captured from speckle pattern interferometry is a cosine fringe pattern and highly affected by speckle noise, employing DHODA for phase derivatives determination from speckle fringe patterns is not a straight forward process. Hence a novel sequential algorithm called Teager Hilbert Huang transform based method for obtaining unwrapped first and second order phase derivatives directly from a single speckle fringe pattern is proposed. The method uses EFEMD (Huang transform), vortex operator (Hilbert transform) and DHODA (Teager operator) for phase derivatives estimation. Enhanced fast empirical mode decomposition is used to normalize a fringe pattern in order to remove background variations and speckle noises. Vortex operator (VO) is used to obtain a complex image from a cosine fringe. Discrete higher order image demodulation algorithm provides the instantaneous frequency i.e., phase derivatives of the fringe pattern. In the proposed method, the phase derivatives obtained could be integrated directly to obtain a phase map.

In DSPI, an intensity field of fringe pattern recorded is given by:

$$I(m,n) = \left| A(m,n) + B(m,n)\cos\{\varphi(m,n)\} + \eta(m,n) \right| \tag{3.28}$$

where $A(m,n)$ is the background variation, $B(m,n)$ is a local amplitude and $\phi(m,n)$ is a phase value. As mentioned earlier, the fringe pattern I_r after EFEMD normalization is given by:

$$I_r(m,n) = \cos\{2\varphi(m,n)\} \tag{3.29}$$

Fringe pattern I_r is a pure cosine signal with phase $\varphi(m,n)$ and vortex operator is used to obtain a complex image from the cosine signal. A combined plane fit and gradient method for obtaining an orientation map was employed (Yang et al, 2007). This method provides a π modulo map with a high accuracy irrespective of speckle noise level. Since the π modulo map causes sign ambiguity it is unwrapped into a 2π modulo map. Once the orientation map is obtained, VO is employed to convert the cosine signals into a complex amplitude signal as shown below.

$$VO\{I_{r(m,n)}\} = \exp\{-j\theta(m,n)\}FFT^{-1}[\exp\{j\varpi(m,n)\}FFT[I_r(m,n)]] \tag{3.30}$$

$$CP_s(m,n) = I_r(m,n) - jVO\{I_r(m,n)\} \tag{3.31}$$

$$CP_s(m,n) = \exp\{j\varphi(m,n)\} \tag{3.32}$$

Any fringe pattern can be converted into a complex amplitude signal in this way and DHODA can be employed for phase derivatives determination from this complex amplitude signal, similarly as it is employed on the complex amplitude signal from DHI. The schematic flowchart of the proposed Teager Hilbert Huang transform for determination of high quality unwrapped phase derivatives from a single fringe pattern is shown in Fig. 3.2. The proposed method can determine high quality slope, curvature and twist maps from a single fringe pattern obtained from an out of plane displacement measuring DSPI setup. This method can also be employed for determining curvature and twist maps from shearography fringe patterns.

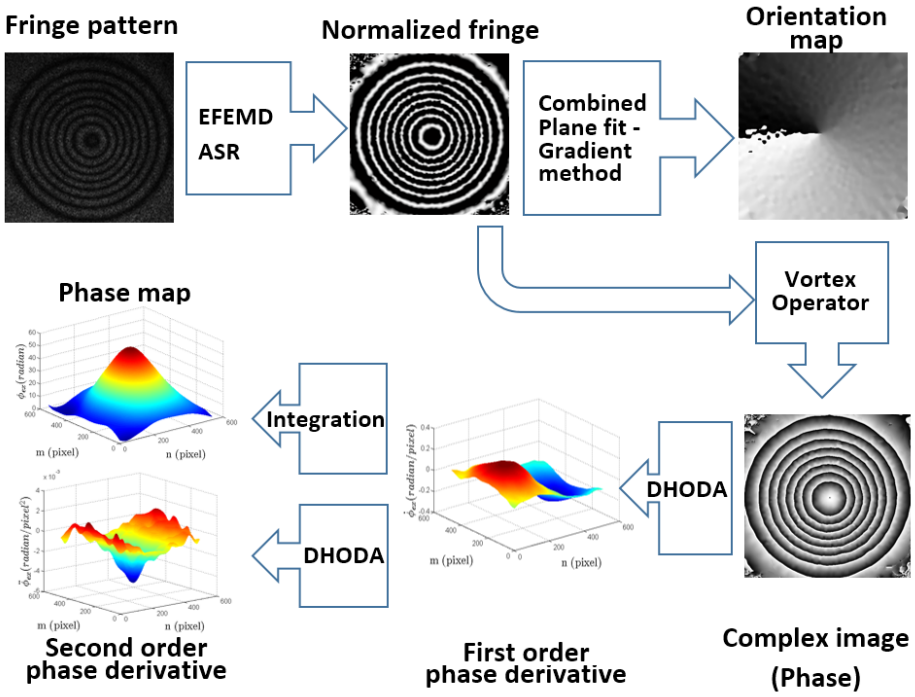

Figure 3.2 Schematic diagram of Teager-Hilbert-Huang transform algorithm.

3.2.2 Phase derivatives determination using fringe orientation and density maps

In Teager-Hilbert-Huang transform method, a sequential algorithm is proposed to obtain phase derivatives from a fringe pattern. In this section, a direct first order phase derivative determination method is proposed. The proposed method uses fringe orientation and density maps to determine phase derivatives from a single fringe pattern. Since this method requires a normalized fringe pattern, ASR-EFEMD is employed as discussed in previous sections. Figure 3.3 shows a pictorial representation of a fringe pattern with a selected window, fringe orientation and phase gradient directions. In the selected window, the directional difference of a fringe is minimum along a fringe tangential direction (fringe orientation direction) and maximum along a direction normal to the fringe (phase gradient direction). From the fringe density and phase gradient direction, the phase derivatives $\frac{\partial \varphi}{\partial x}(m,n)$ and $\frac{\partial \varphi}{\partial y}(m,n)$ at each pixel in the x and y directions can be obtained using the following equations.

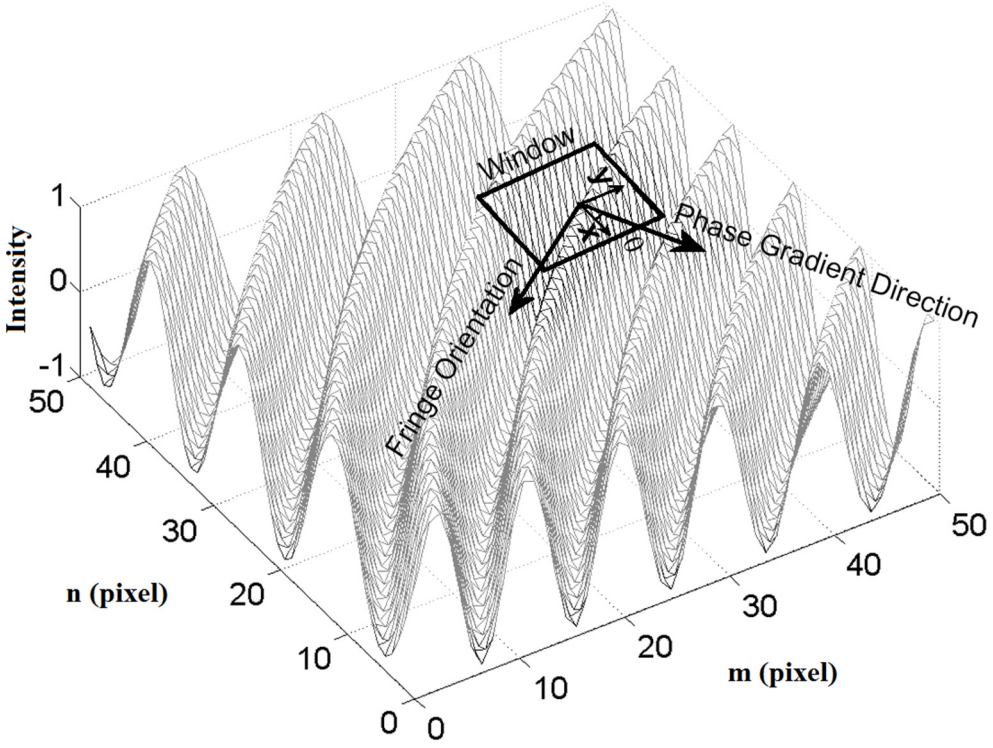

Figure 3.3 A Fringe map.

$$\frac{\partial \varphi}{\partial x}(m,n) = 2\pi \frac{|N|}{W} \cos\{\theta_g(m,n)\} \tag{3.33}$$

$$\frac{\partial \varphi}{\partial y}(m,n) = 2\pi \frac{|N|}{W} \sin\{\theta_g(m,n)\} \tag{3.34}$$

where $\theta_g(m,n)$ is the phase gradient angle (with respect to the x axis), N is the number of fringes along the phase gradient direction and W is the length of the window in pixels. The phase gradient per pixel $\Delta\varphi(m,n)$ (radians/pixel) along the phase gradient direction is obtained by multiplying the fringe number N with 2π and dividing it by the window length W. Subsequently, multiplying the phase gradient per pixel $\Delta\varphi(m,n)$ by $\cos\{\theta(m,n)\}$ and $\sin\{\theta(m,n)\}$, we obtain the phase derivatives $\frac{\partial \varphi}{\partial x}(m,n)$ and $\frac{\partial \varphi}{\partial y}(m,n)$ along the x and y directions respectively.

Yang et al suggested an accumulated difference method to determine the fringe orientation and density simultaneously from a fringe map (Yang et al, 2007). The fringe density is calculated from the maximum directional difference while the fringe orientation is obtained from the minimum fringe difference direction. The π modulo fringe orientation is then unwrapped to obtain 2π modulo fringe orientation. As the influence of the window size is minimal compared to the plane-fit method, this method is more robust in determining the fringe orientation/phase gradient direction (Yang et al, 2007). Though the fringe density is susceptible to noises, the effect can be reduced by using EFEMD in the preprocessing. Furthermore a low pass medium filter can be applied on the fringe density to remove spikes caused by residual noises. The phase derivatives obtained using Eqs. (3.33) and (3.34) are biased due to noise sensitivity of the fringe density. Hence they are smoothened out by least square B-spline fitting interpolation. In the proposed method, though Yang's method is discussed for the determination of fringe orientation and density, any other method could also be used.

3.3 Phase retrieval

3.3.1 Derivative based regularized phase tracker

In dynamic fringe measurement, phase values at every transient position are required and it is difficult to capture more than one fringe pattern at each transient position. Hence phase extraction from a single fringe pattern is one of the most important and difficult tasks in dynamic measurement interferometry. As mentioned in the literature review, Fourier transform and other spatial phase shifting methods require a complex experimental setup to introduce a carrier frequency into a closed-fringe pattern. Phase demodulation methods provide phase values from a single closed-fringe interferogram and do not require a complex experimental setup. RPT method is one of the most robust phase demodulation methods but its phase

reconstruction accuracy drops around the saddle points of the fringe pattern. In this section, a novel RPT method called derivative based regularized phase tracker (DRPT) is proposed. The method can successfully demodulate single closed fringe patterns with less computation time than existing RPT methods and also can provide better accuracy around saddle points than conventional RPT.

The phase values can be obtained by integrating the phase derivatives that are calculated from the previous sections but even a small deviation in the phase derivatives would cause a large error in the phase values. As we know, in RPT, the phase demodulation is carried out by minimizing a cost function with respect to phase $\phi'(m,n)$, and phase derivatives $\phi_x(m,n)$ and $\phi_y(m,n)$ as given below.

$$U(m,n) = \sum_{(\varepsilon,\eta)\in M_w} \{[\overline{I}(\varepsilon,\eta) - \cos\{p(m,n,\varepsilon,\eta)\}]^2 + \beta_{reg}[\phi'(\varepsilon,\eta) - p(m,n,\varepsilon,\eta)]^2 s(m,n)\} \tag{3.35}$$

$$p(m,n,\varepsilon,\eta) = \phi'(m,n) + \phi_x(m,n)\{m-\varepsilon\} + \phi_y(m,n)\{n-\eta\} \tag{3.36}$$

where ε & η represent the local indices of the neighborhood window M_w and m & n represent the indices of the entire fringe map. Since, local frequencies $\phi_x(m,n)$ and $\phi_y(m,n)$ are also determined along with phase values, the minimization of the cost function requires more computation time.

In the proposed method, we suggest a novel derivative based phase tracking demodulation method which utilizes predetermined phase derivatives and a simplified cost function to estimate the phase values. The phase derivatives calculated from Eqs. (3.33) and

(3.34) also represent the local frequencies $\phi_x(m,n)$ and $\phi_y(m,n)$. Hence the cost function in Eq. (3.35) is minimized with respect to the phase value $\phi'_{(m,n)}$ to obtain:

$$p(m,n,\varepsilon,\eta) = \phi'(m,n) + \frac{\partial\varphi}{\partial x}(m,n)\{m-\varepsilon\} + \frac{\partial\varphi}{\partial y}(m,n)\{n-\eta\} \tag{3.37}$$

In the proposed method, the computation time is considerably reduced due to a reduction in the number of variables, which in turn reduces the complexity of the minimization function. In addition to this advantage, RPT phase demodulation requires a fringe following technique to avoid saddle points but the proposed method utilizes predetermined local frequencies which guides the phase demodulation around the saddle points to achieve better accuracy than conventional RPT. Hence the proposed DRPT method is able to outperform the RPT phase demodulation method in terms of both accuracy and computing time.

3.3.2 Vibration amplitude measurement in TA-DSPI

As mentioned in the literature, quantitative vibration amplitude measurement requires good fringe contrast and higher computational time. In previous section, an amplitude-varied refreshing reference frame fringe pattern is presented for improvement of TA-DSPI fringe pattern. In this section, a quantitative amplitude measurement from a single TA-DSPI fringe pattern that is obtained from amplitude-varied refreshing reference frame technique is proposed.

As mentioned before, phase values can be retrieved from a single fringe pattern using DRPT method. The proposed model is based on cosine fringes so it is necessary to device a new model for fringes obtained using Eq. (3.5). Pryputniewicz et al proposed

a method, in which zero order Bessel fringes of the first kind are analyzed as they are cosine fringes and after phase retrieval a look up table is used to compensate the conversion from Bessel to cosine (Pryputniewicz and Stetson, 1989). Similar approach can be used for phase demodulation of fringe patterns obtained in this method. In Eq. (3.5), cosine functions replace Bessel functions as shown below.

$$I_{avg0} - I_{avg1} = B[\cos(\tilde{\Omega}) - \cos(\tilde{\Omega} + \Delta\tilde{\Omega})] \tag{3.38}$$

$$\tilde{\Omega}(m,n) = \Omega(m,n) + \varepsilon(m,n) \tag{3.39}$$

where $B = I_0 V \cos(\phi_0 - \phi_r)$ and ε is an error introduced by the conversion from Bessel to cosine. From trigonometry the two cosine terms are rewritten as:

$$I_{avg0} - I_{avg1} = 2B[\sin(\frac{2\tilde{\Omega} + \Delta\tilde{\Omega}}{2})\sin(\frac{\Delta\tilde{\Omega}}{2})] \tag{3.40}$$

Since the change in the fringe locus function $\Delta\tilde{\Omega}$ is small compared to $2\tilde{\Omega}$ and $\sin(\Delta\tilde{\Omega})$ is a slow varying background function. Equation (3.40) is reduced to:

$$I_{avg0} - I_{avg1} = \bar{B}[\sin(\tilde{\Omega}')] \tag{3.41}$$

where $\bar{B} = 2B\sin(\frac{\Delta\tilde{\Omega}}{2})$ and $\tilde{\Omega}' = \tilde{\Omega} + \frac{\Delta\tilde{\Omega}}{2}$ i.e., $\tilde{\Omega}' = \tilde{\Omega}(1 + \frac{r}{2})$. From Eq. (3.41), it is shown that the fringes obtained are sine functions.

Figure 3.4(a) shows a sine wave compared with a normalized wave function which is obtained using Eq. (3.5). While Fig. 3.4(b) shows a cosine wave compared with a normalized zero order Bessel function of the first kind. It is evident that the fringes produced by the proposed method can be considered as a sine function while a zero order Bessel function of the

first kind can be considered as a cosine function. Since $\Delta\tilde{\Omega}$ is small, $\sin(\frac{\Delta\tilde{\Omega}}{2})$ can be considered small as well and it would cause a slow varying background intensity. Hence the intensity value obtained using Eq. (3.41) has to be normalized and ASR-EFEMD is used for normalization to remove the noise and background contrast variation. The intensity of the fringes after normalization is a pure sine function given by:

$$I_n = \sin(\tilde{\Omega}') \tag{3.42}$$

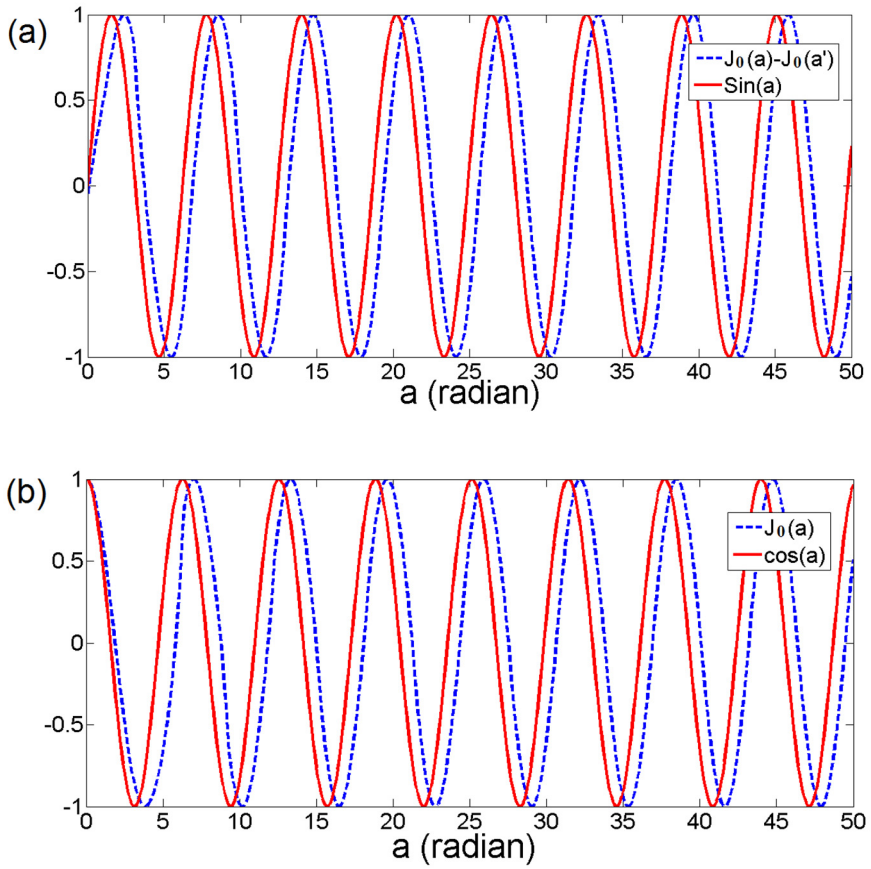

Figure 3.4 (a) A sine wave compared with a normalized fringe pattern obtained using the proposed method; (b) A cosine wave compared with a normalized Bessel function.

In the DRPT method, the phase in a cosine function, say $\cos(\phi')$, is demodulated by minimizing a cost function with respect to $\phi'(m,n)$ as shown in Eqs. (3.35) and (3.37). The fringes obtained are sine functions as shown in Eq. (3. 5) so the DRPT is modified for sine function vibrational amplitude measurement. The minimization function is given by

$$U_{TA}(m,n) = \sum_{(\varepsilon,\eta)\in M_{m,n}} \{[I_n(\varepsilon,\eta) - \sin\{p(m,n,\varepsilon,\eta)\}]^2 + \beta_{reg}[\tilde{\Omega}'(\varepsilon,\eta) - p(m,n,\varepsilon,\eta)]^2 s(m,n)\} \tag{3.43}$$

After phase demodulation, the phase value $\tilde{\Omega}'$ is corrected for errors introduced as shown in Eq. (3.39) to obtain accurate phase value Ω and the amplitude A_v.

3.4 Phase unwrapping

3.4.1 Ensemble of HGA for phase unwrapping

3.4.1.1 Genetic Algorithm

Genetic algorithm (GA) is an AI method which is based on the concept of evolution. It is a stochastic search technique that uses global random or problem-specific search controlled by a set of different operators. Every possible solution set will be considered as a single chromosome and every variable in the solution set is considered as a gene in the chromosome. The population, which is only a group of chromosomes, will undergo evolution in every generation by three processes called selection, crossover and mutation. Genetic algorithm uses both probability and adaptability in random exploration in search of the fit chromosome or global optimum. The selection process will make sure only fit chromosomes are selected for next generation to ensure 'survival

of the fittest'. The crossover will choose some pair of chromosomes randomly for offspring generation and remaining chromosomes will be moved directly to next generation. Each chromosome pairs which are chosen for crossover will produce two offspring for the next generation. After the crossover process, some randomly chosen genes in some randomly chosen chromosome will undergo some random change in their value. This process is called mutation. If a mutation results in increase in fitness, the mutant gene will be replicated in the similar genes of other chromosomes. Otherwise, those genes will be eradicated gradually in future generations.

Selection will make sure that the search is directed towards the best result while the mutation will ensure that the search will not be trapped in a local optimum. The crossover will make sure that some new solutions (offspring) are generated for every generation. This evolution will be repeated for every generation till the exit criteria is achieved.

The initial solution for GA will be generated randomly. The random initial solution will take more time to converge. Karout et al proposed a hybrid genetic algorithm (HGA) approach for phase unwrapping, which combines the advantages of local search and GA (Karout et al, 2007). The initial population is generated based on a local search method called nearest neighbor method. This reduces the computation time drastically.

3.4.1.2 HGA for phase unwrapping

In GA, solutions are coded as chromosomes and they would be evolved under a fitness function which is defined by the problem. The phase unwrapping problem should be coded in GA syntax to employ HGA for solving it. In branch-cut phase unwrapping method, if a curl operation is applied on the wrapped phase map, noise and discontinuities cause non-zero residues. Branch cut is the region between a positive and

negative residue pair. Hence to determine branch-cuts, the residues should be correctly paired and it can be achieved by minimizing the summation distance between all the residue pairs i.e. total branch cut length. Any wrapped phase map has set of positive and negative residues and the objective is to pair them correctly by minimizing the total branch cut length. In this phase unwrapping coding, positive residues are packed as a primary chromosome and the negative residues are packed as a solution chromosome. Variations in the solution chromosomes are achieved by the modifying the position of the negative residues in the solution. When a solution is provided, positive residues in the primary chromosome will be paired with the corresponding negative residues in the solution chromosome. Fitness of a solution chromosome is calculated by the total Euclidian distance between the paired residuals.

One of the challenges in this phase unwrapping coding is that number of positive and negative residues are not always equal in a residual map. Some residues near the boundary region might have their pairs outside the area of interest. To address such monopole residues, while initial population generation, some of the chosen border pixels are also included as residue pairs. First, each positive residues determine their neighbor negative residue. If the image boundary is nearer than the nearest negative residue, the corresponding border pixel is considered as the nearest neighbor. Subsequently, each negative residues which are not paired with any positives residues are paired with their nearest border pixel. These border pixel pairs of negative residues along with positive residues forms a primary chromosome. Figure 3.5 shows the residues and their corresponding opposite polarity. Primary chromosome which contains all the positive residues and the border pixel pairs of left out negative residues, is shown in Fig. 3.6. The corresponding residue pairs of the primary chromosome form the initial solution chromosome and it is shown in Fig. 3.6. In GA, each functional unit

of the chromosome is called as genes, so each residue in our phase unwrapping problem is a gene in a solution chromosome.

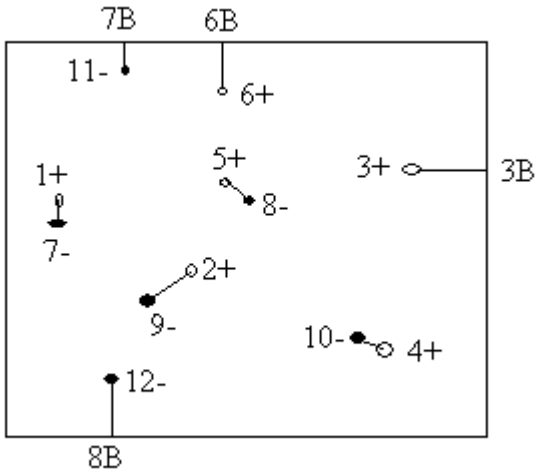

Figure 3.5 Residue and their corresponding opposite polarity.

Primary chromosome:	1+	2+	3+	4+	5+	6+	7B	8B
Initial chromosome:	7-	9-	3B	10-	8-	6B	11-	12-

Figure 3.6 Primary and initial chromosome.

3.4.1.2a Initial population generation

After coding the initial solution chromosome, an initial population (Fig. 3.7) is generated. The initial solution chromosome is create using nearest neighbor local search, so the GA converges faster than a random solution. More solution chromosomes are generated using a random initialization method from the single initial solution chromosome. In this method, two genes are randomly selected from the initial solution chromosome and the positions of these two genes are swapped in the chromosome. The cut length i.e., the total Euclidian distance between residue pairs, is calculated before and after the swapping. If the swapping generates better results i.e. a shorter cut length, the swapping is finalized. Otherwise, the genes are reverted back to their initial position.

This process (NNR2OPTI) is repeated until all the chromosomes required for the population are found.

Negative chromosome 1:	7-	9-	3B	10-	8-	6B	11-	12-
Negative chromosome 2:	3B	9-	7-	10-	8-	11-	6B	12-
Negative chromosome 3:	9-	7-	3B	10-	8-	6B	11-	12-
Negative chromosome 4:	7-	9-	8-	3B	10-	6B	11-	12-
Negative chromosome 5:	7-	3B	9-	10-	8-	6B	11-	12-
Negative chromosome 6:	7-	9-	3B	10-	8-	11-	6B	12-

Figure 3.7 Initial population generation.

3.4.1.2b Fitness evaluation and selection operator

A selection operator is a survival key for the evolution. It is problem specific but should prevent a search from being trapped in a local optimum. The fitness of the chromosomes generated is evaluated based on a fitness function shown in Eq. (3.44). The chromosomes are sorted out in the order of fitness level. Similar chromosomes are deleted and new chromosomes are generated using the NNR2OPTI method. If the new chromosomes generated are similar to the existing chromosomes, they are deleted and newer chromosomes are generated. This process is repeated until all the chromosomes in the population are unique or after a specific time (*Lm)* of repetition. *Lm* is a parameter for this operation to make sure that the evolution is not trapped in a loop. A larger value of *Lm* gives a better possibility of unique chromosomes in a population. After this, a set of chromosomes, one based on the fitness value and another one randomly, are selected for the survival in the next generation. This step is repeated to form a whole population of chromosomes. Table 3.1 shows the fitness evaluation process.

$$\text{Fitness} = \sum_{i}^{N_p} [(xg_i^+ - xg_i^-)^2 + (yg_i^+ - yg_i^-)^2]^{1/2} \quad (3.44)$$

Where g_i^+ is a positive residue, g_i^- is a negative residue, xg_i^+ is a x coordinate, yg_i^+ is a y coordinate and N_p is the number of pairs.

Table 3.1 Selection process of HGA.

Current Population	Fitness Value	Sorted Population	Fitness Value	New Sorted Population	Fitness Value
Chromosome 1:	5789	Chromosome 6:	5600	Chromosome 6:	5600
Chromosome 2:	7856	Chromosome 1:	5789	Chromosome 1:	5789
Chromosome 3:	6159	Chromosome 3:	6159	Chromosome 3:	6159
Chromosome 4:	7201	Chromosome 5:	6159	Chromosome 5:	6356
Chromosome 5:	6159	Chromosome 4:	7201	Chromosome 4:	7201
Chromosome 6:	5600	Chromosome 2:	7856	Chromosome 2:	7856

3.4.1.2c Crossover and mutation

The smallest edge crossover operator (SCX) is designed specifically for phase unwrapping (Karout et al, 2007). The chromosomes pairs are randomly selected for a crossover based on probability *Pc* so that good genes from the parents are preserved and better offspring are produced. The genes with minimum cut length from the parents would be transferred to the offspring. This might result in repeated genes in the offspring hence a LK method is employed to solve this issue as shown in Fig. 3.8. *L* number of genes are selected in the chromosome and their cut lengths are calculated. The genes are swapped to the corresponding positions of other genes and the cut lengths are calculated again. The process is continued until the cut length of a swapped position is shorter than the precious position. This LK algorithm is also used as a mutation operator in the proposed method. After the crossover, some chromosomes are randomly selected for mutation based on the probability *Pm*. Some genes in the selected

chromosomes are randomly selected and LK method is employed as shown in Figs. 3.9 and 3.10.

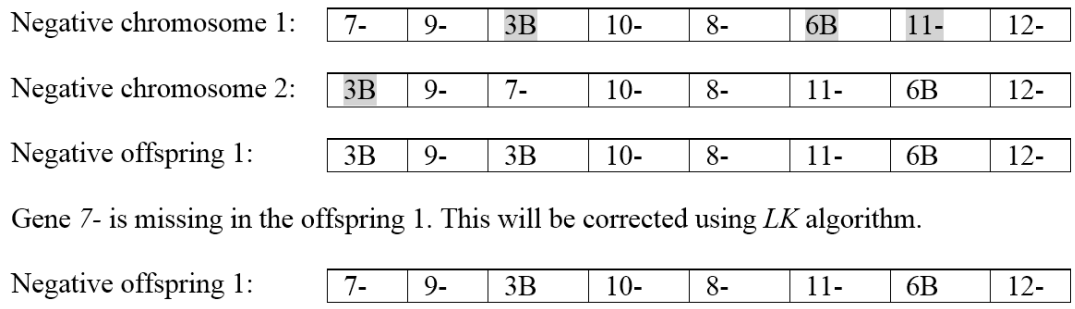

Figure 3.8 Crossover process.

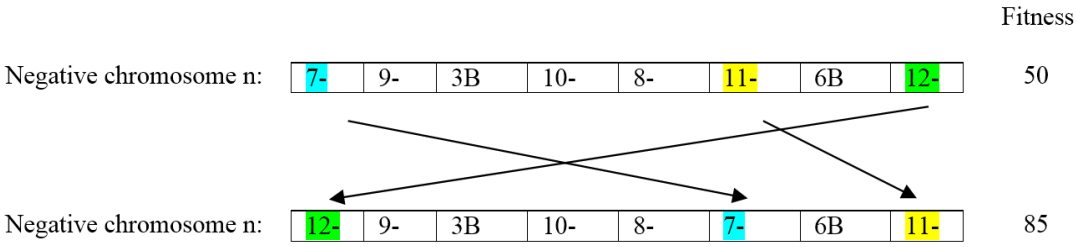

Figure 3.9 L-K Mutation operator performing three gene mutation (Unsuccessful).

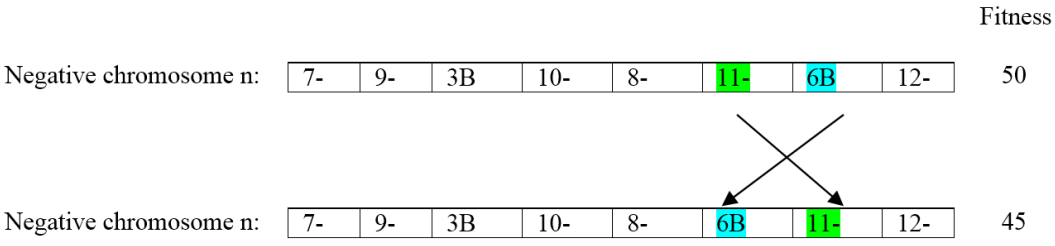

Figure 3.10 L-K Mutation operator performing two gene mutation (Successful).

3.4.1.3 Ensemble of HGA (eHGA)

In this method, the ensemble of parameter values is simultaneously employed in the HGA by using parallel populations. Even though the parameters are obtained selectively, it is uncertain that any single combination of parameter values would be effective for a particular problem (Tasgetiren et al, 2010). Based on the path chosen

(value fixed for parameters), the search explores in a space and selects a local optimum. For different values of the parameters, different paths are chosen. To make sure that more paths are evaluated in a single run and more possibilities are explored in the searched space, simultaneous usage of different parameter values is employed with different parallel populations. The offspring produced from a population not only competes with its peers from the same population but also with offspring of other populations. This ensemble of HGA (EHGA) explores more within a search space and also converges better with the same computational expense. It is also mentioned in the literatures that the ensemble will increase the performance of GA (Tasgetiren et al, 2010; Zhou and Sun, 2005).

The EHGA has *Np* populations evolving in parallel and each population has *Nc* chromosomes. Initial population generation is carried out for all the populations and generated chromosomes are assigned to each population. The selection operated can be completely replaced by tournament operator in the EHGA. However, for the first generation, some selection should be carried out to obtain the survival criteria before the chromosomes undergo the crossover operation. In the following generations after mutation, the tournament operator is employed. However, the selection process is not completely replaced by the tournament operator as the selection operator with a *Lm* parameter is retained to ensure the uniqueness of the chromosomes. The *Lm* parameter is assigned with unique values for every population. After the selection, crossover and mutation operations are carried out in each population. The parameters *Pc* and *Pm*, the probability for a chromosome to undergo crossover and mutation respectively, are also assigned unique values in each population.

After the operations are carried out, *Nc* numbers of offspring would be generated from each population. All the offspring from each population are put together in the offspring pool and a tournament selection is carried out to select the chromosomes for the next generation. The tournament operator ensures that the offspring competes with all the offspring from every population. Hence it is evident that the fittest offspring joins a different population even though they are generated from another population. This increases the possibilities in the search space.

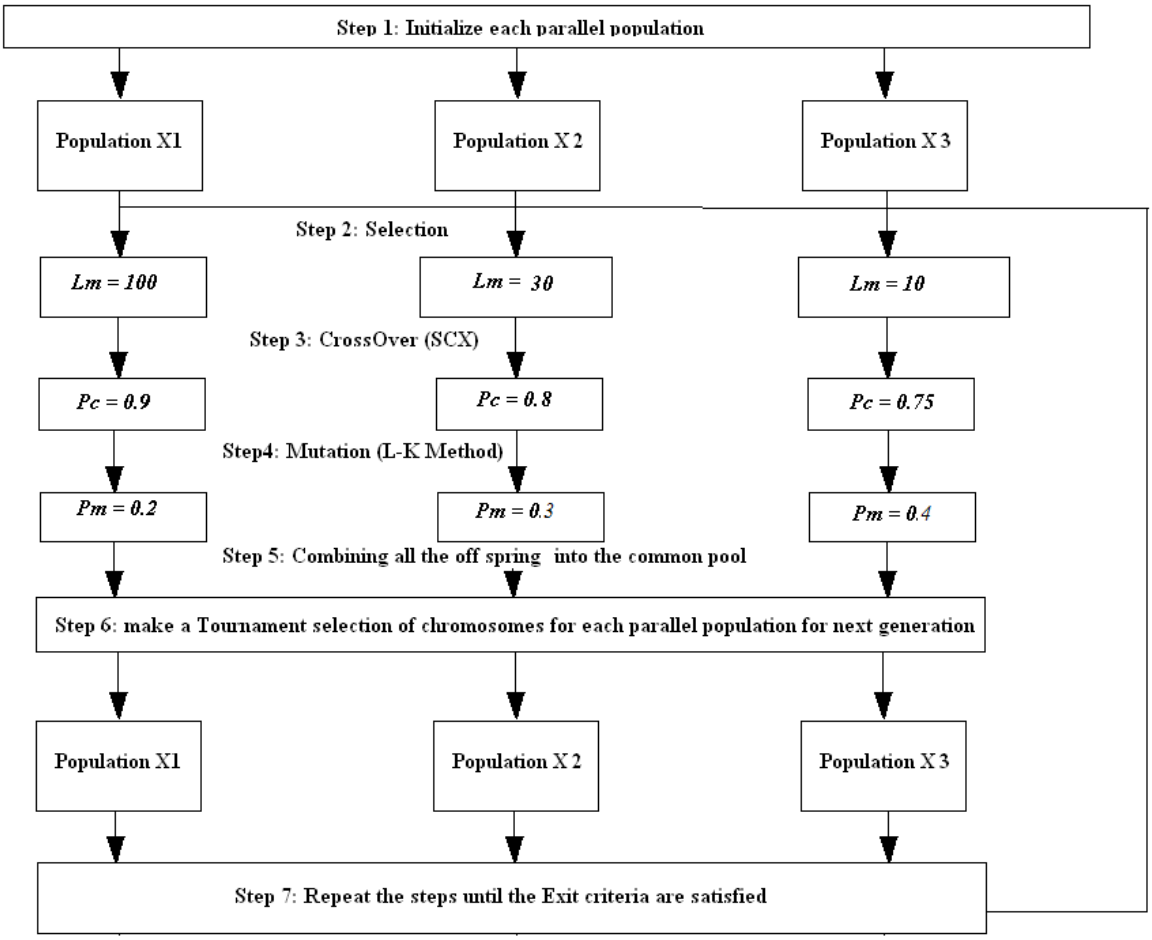

Figure 3.11 Flowchart for eHGA.

The offspring in the pool are sorted based on the fitness and each population gets half of the required chromosomes (*Nc*/2) based on their fitness and the remaining half of the chromosomes are selected randomly. For example, if *Nc*=10, the fittest 5

chromosomes in the whole pool would be selected for every population irrespective of their origin and the remaining 5 chromosomes are randomly selected to ensure variation in the population. Since the fittest chromosomes are desirable, this type of selection ensures that all the offspring from different populations would have an equal chance to represent any given population. The flow of the EHGA is summarized as follows and a flowchart of algorithm is shown in Fig. 3.11.

Step 1, Initialize each parallel population using NNR2OPTI operator.

Step 2, Select the surviving chromosomes by selection operator in each population with unique value for *Lm* parameter.

Step 3, Create an offspring by crossover operator (SCX) in each population with unique value for *Pc*.

Step 4, Operate mutation in each parallel population using *LK* algorithm mutation operator with unique value for *Pm.*

Step 5, Combine all the offspring from each parallel population and create a pool of offspring for the tournament.

Step 6, Select chromosomes for each parallel population for next generation by tournament operator.

Step 7, Repeat steps 2 to 6, until the exit criteria are satisfied.

3.5 Material characterization of a small cantilever beam

One of the important applications of optical techniques is material characterization of small objects as they are non-contact, non-destructive and provide full field measurements with high-resolution (Kim et al, 2008; Farias et al, 2009). In this section,

an experimental protocol is designed, which applies the DHODA algorithm, for determining the elastic modulus of a small cantilever beam. The speckle pattern interferometry technique is highly sensitive to the rigid body motion, hence the displacement obtained from DSPI is the summation of deformation and rigid body motion (Chen et al, 2013). Hence even a small rigid body movement affects the accuracy of the deformation measurement which in turn affects the accuracy of the mechanical properties determined from these data. Chen et al proposed a correction method for strain errors induced by small rigid body motions in ESPI. However this method requires the amount of rigid body motion for the error correction and in real applications, the rigid body motion is an unknown quantity. In this experiment, the rigid body movement problem is addressed to obtain accurate elastic modulus of the materials.

The deflection and slope along x axis of a cantilever beam loaded at the end is given by:

$$w(x) = \frac{Px^2(3L - x)}{6EI_a} \tag{3.45}$$

$$\frac{\partial w}{\partial x}(x) = \frac{Px(2L - x)}{2EI_a} \tag{3.46}$$

where w is the deflection in z direction, P is the load applied, L is the length of the cantilever beam, E is the elastic modulus and I_a is the area moment of inertia. A cantilever beam before and after loading is shown in Fig. 3.12. An out of plane displacement measuring DSPI experimental setup measures the deflection w and ideally, the Young's modulus value could be determined from every pixel as it would

provide a deflection data from Eq. (3.45). However, as DSPI is sensitive to rigid body movement, the out of plane displacement captured by the DSPI set-up would be corrupted with rigid body movement. The translation movements in the x and y axis and the rotation about the z axis causes in-plane displacement so they would not influence the out of plane displacement measurement. Rotation about the x axis would cause a change in the deflection along the y direction. Hence it is ignored as the deflection and slope of the cantilever beam are functions of x. Translation in the z direction and rotation about the y axis cause a change in out of plane displacement and slope as given below:

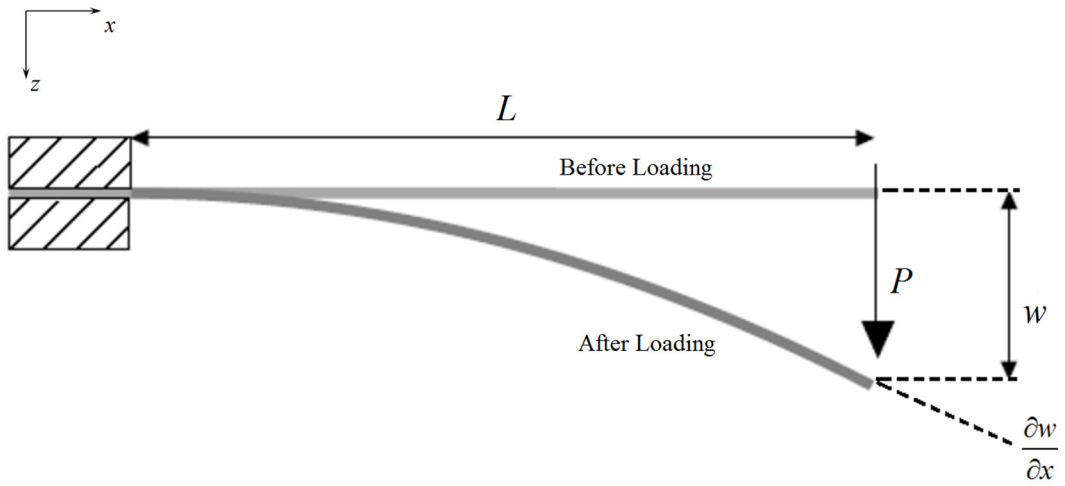

Figure 3.12 Deflection of a cantilever beam loaded at the end.

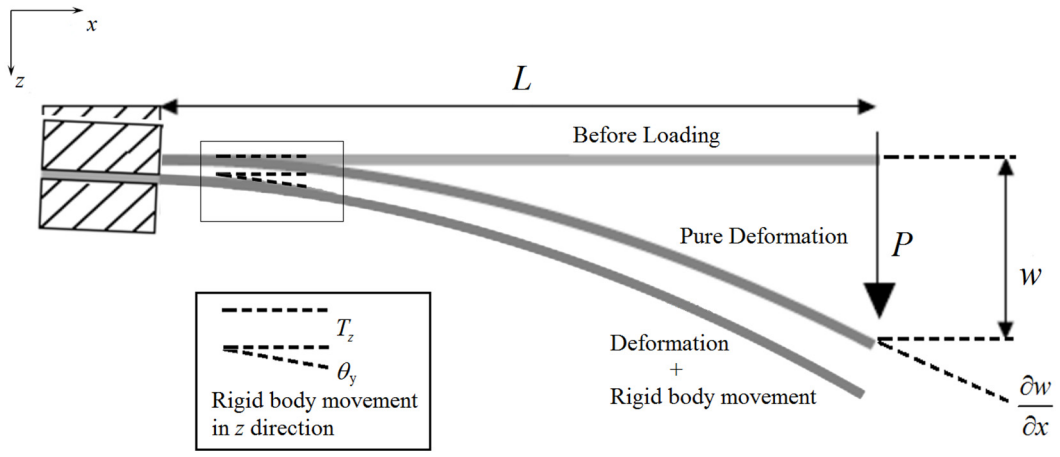

Figure 3.13 Rigid body movement along with deflection of a cantilever beam.

$$w_d(x) = \frac{Px^2(3L-x)}{6EI_a} + \tan(\theta_y)x + T_z \tag{3.47}$$

$$\frac{\partial w_d}{\partial x}(x) = \frac{Px(2L-x)}{2EI_a} + \tan(\theta_y) \tag{3.48}$$

where w_d is the out of plane displacement obtained by a DSPI setup, θ_y is a rotation about the y axis and T_z is a translation in the z direction.

Figure 3.13 shows the actual deformation and rigid body movement due to a rotation and translation on a cantilever beam. Even a small rigid body movement would cause a large deviation in the elastic modulus value. Hence it is not straight forward to determine the elastic modulus of the material from the out of plane displacement values obtained by the DSPI setup as it is influenced by rigid body motion (translation and rotation). As it is known that the actual slope of deformation is zero at the fixed end $\frac{\partial w}{\partial x}(0) = 0$, the rotation term from Eq. (3.48) can be eliminated easily. Hence the elastic modulus is determined from a slope map irrespective of the rigid body movement.

However, in applications where the boundary conditions are unknown and a zero-slope point ($\frac{\partial w}{\partial x} = 0$) does not exist in the measured area, the proposed method cannot be applied.

The deflection of a cantilever beam produces open fringes so the complex field of the phase map is obtained directly using Fourier transform method. From the complex field, a biased slope map is determined using DHODA. After that a median filtering and B-spline smoothing is carried out to obtain a high quality unwrapped slope map. Every pixel in the slope map provides an elastic modulus value (using Eq. (3.48)) and statistical mean and standard deviation of the elastic modulus of the material is obtained from the elastic modulus data at every pixel. There is no need for normalization of the speckle fringe pattern as this method uses Fourier transform to obtain a complex field of the phase map.

CHAPTER FOUR

EXPERIMENTAL WORK

To verify the theories and algorithms proposed digital holographic interferometry (DHI), digital speckle pattern interferometry (DSPI) and digital speckle shearing interferometry (DSSI) experimental validations are carried out. The out of plane displacement and displacement derivatives of centrally loaded circular plate is recorded using these systems. Quantitative vibration modal analysis on a thin circular plate is carried out using time average speckle pattern interferometry. Elastic modulus of a cantilever beam is determined using DSPI system. The equipment and experiment procedures are described in detail in the following sections. Apart from the experiments, various simulation studies are carried out as well to analyze the robustness and effectiveness of the proposed algorithms. All simulations are carried out using Matlab R2013b 64 bit and run on a computer equipped with Intel Core i7-4770 (3.4 GHz) processor and 8 GB RAM.

4.1 Digital holographic interferometry (DHI)

Figure 4.1 shows a schematic experimental arrangement for recording digital holograms in the spatial-domain analysis. A fiber optic coupler separates a coherent light beam into two beams of intensity ratio 90:10, i.e., object and reference waves. A polarizer is placed in the reference wave path to regulate the intensity. A beam splitter cube is placed in front of a CCD camera to recombine object and reference waves. A digital hologram is recorded by the CCD camera. A HeNe laser with power of 30 mW and wavelength 632.8 nm is used as light source and Manta G-201B monochrome camera, which has Sony ICX274AL CCD sensor with 1628x1236 pixels of size 4.4 μm

x 4.4 μm, is used to capture the fringe pattern. The CCD camera used to capture the holograms is shown in Fig. 4.2. A circular aluminum plate with a center point load is used as a specimen for the experiment. The aluminum disc has thickness of 1.5 mm and diameter of 50 mm. The micrometer loading setup used to apply static load at the center of the disc is shown in Fig. 4.3.

As this is a Fourier lensless holography setup, the reference beam is a spherical wave. Hence, every pixel of the CCD can be utilized, and it can provide much sharper images (Wagner et al., 1999). The distance between the specimen and the CCD should be equal to the distance between the point source of the spherical reference wave and the CCD to obtain a Fourier lens-less hologram. In the experimental setup, the distance between the specimen and the CCD is 93 cm. The entire setup is placed on a vibration-isolation table to reduce the influence of environmental vibration and ambient conditions. Two holograms one before and one after loading are captured to obtain the phase difference caused by the loading. The holograms captured before and after loading are used to validate various algorithms developed in this thesis.

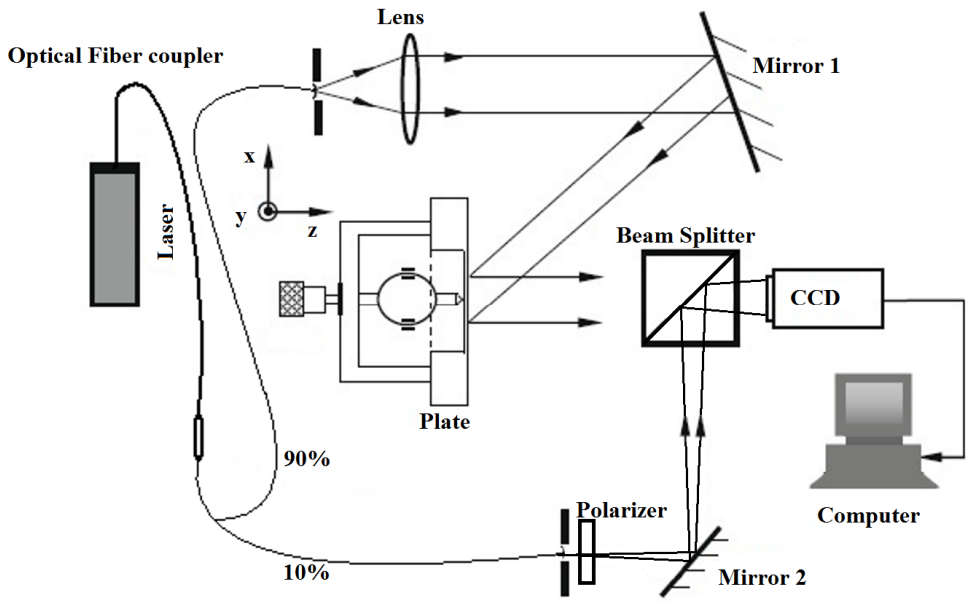

Figure 4.1 A schematic setup of DHI system.

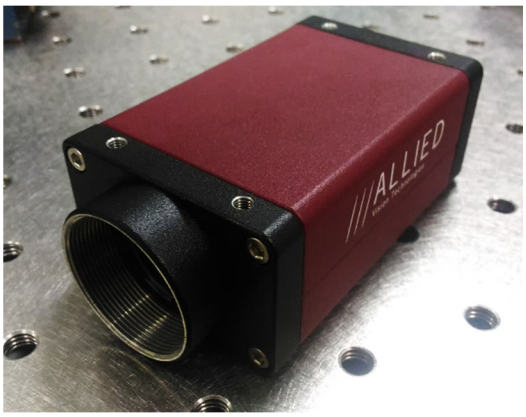

Figure 4.2 Manta G-201B monochrome CCD camera.

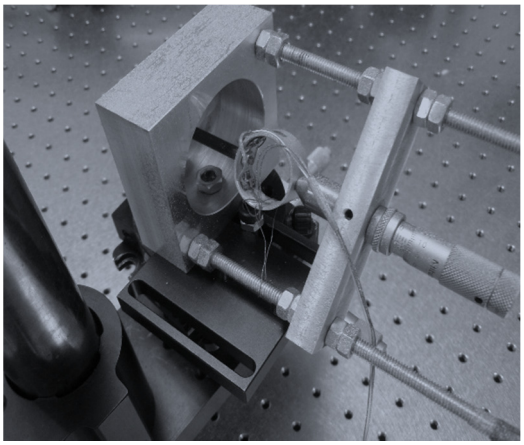

Figure 4.3 Thin plate specimen loaded at center.

4.2 Digital speckle pattern interferometry (DSPI)

4.2.1 Static loading on a thin circular plate

The experimental setup of Michelson interferometry for an out of plane displacement sensitive DSPI measurement is shown in Fig. 4.4. A coherent light beam is opened by a microscope objective and a beam-splitter splits the beam into a reference and an object waves. The reference wave incidents on a reference plate and creates speckle patterns on the reference plate. Similarly the object wave creates speckle patterns on the specimen. The specimen and the reference plate

have optically rough surface and are painted with matt-white paint to have better visibility. The interference between these two speckle-patterns are captured by a CCD camera. The CCD camera has a lens and the speckle pattern has subjective speckles as the pattern is captured by an imaging system.

A HeNe laser with a power of 30mW and wavelength 632.8 nm is used as a light source. A Manta G-046B monochrome camera, which has Sony ICX415 CCD sensor with 780 x 582 pixels of size 8.3 μm, is used to capture the fringe pattern. A circular plate with diameter of 65 mm and thickness of 1.23 mm, clamped at its edge, is used as a test specimen. The specimen is made of aluminum 6061-T6 alloy which has an elastic modulus 69 GPa and a Poison's ratio 0.33. A point load is applied at the center of the specimen through a micrometer. A TML CLS-50NA compression load cell which measures load ranging 0-50 N, is mounted between the specimen and the micrometer as shown in Fig. 4.5. The load cell indicates the load applied and is useful to validate the measurement in the DSPI system.

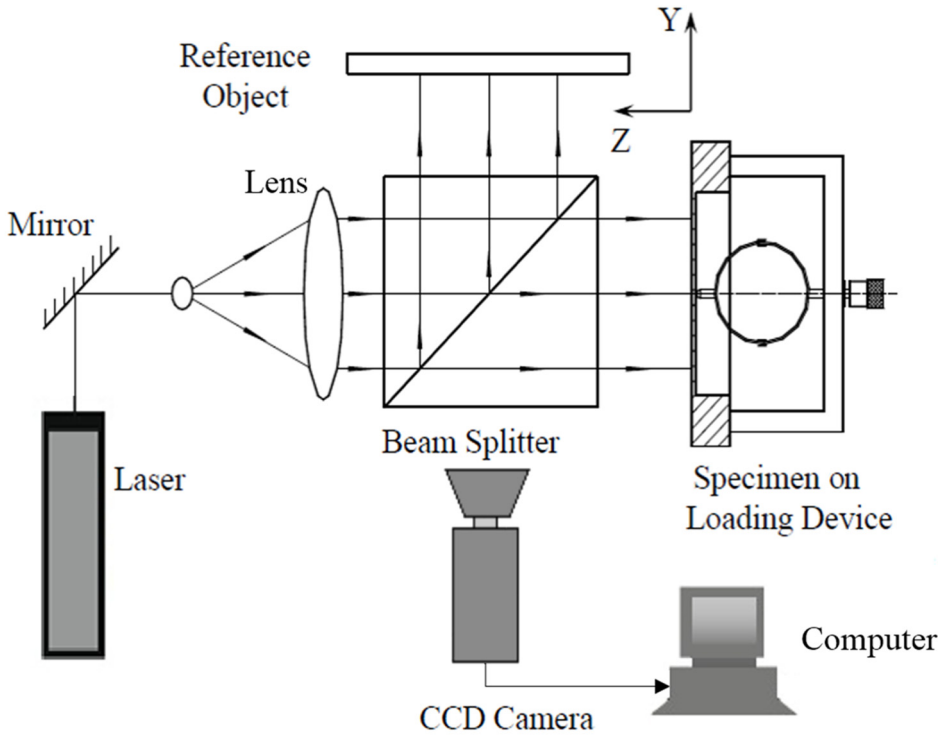

Figure 4.4 A schematic setup of Michelson DSPI system.

Both the reference plate and the specimen should be kept at equidistance from and the camera should be focused on the speckle-patterns to obtain high fringe contrast. A speckle-interference image is captured before loading and stored as a reference image. A static load is applied and the corresponding fringe patterns are captured by real time subtraction of the speckle-patterns after loading from the reference image. This real-time subtraction is carried out using a software named UU (Chen 2013).

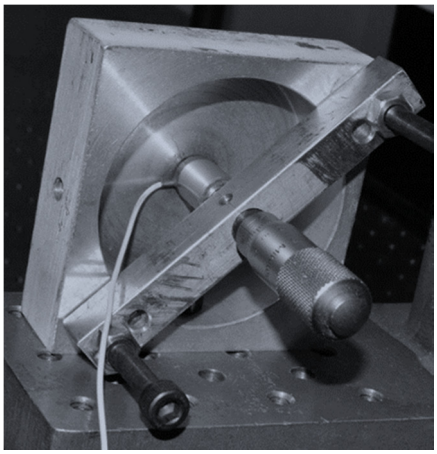

Figure 4.5 Load cell and micrometer setup.

4.2.2 Material characterization of a small cantilever beam

Material characterization of a cantilever beam is carried out using a DSPI system. The schematic diagram of the experimental setup is shown in Fig. 4.6, which is also a Michelson interferometer setup. Same laser source and CCD camera are used for the setup. The specimen and the loading setup are different as a cantilever beam is the specimen. Magnesium nanocomposite material is used to fabricate a small cantilever beam of length 100 mm with rectangular cross section of same width and height of 5.5 mm. A fixture holds the specimen in one end with the effective length of 66mm and a micrometer attached with the load cell is used to apply load on the other end of the cantilever beam as shown in Fig. 4.7.

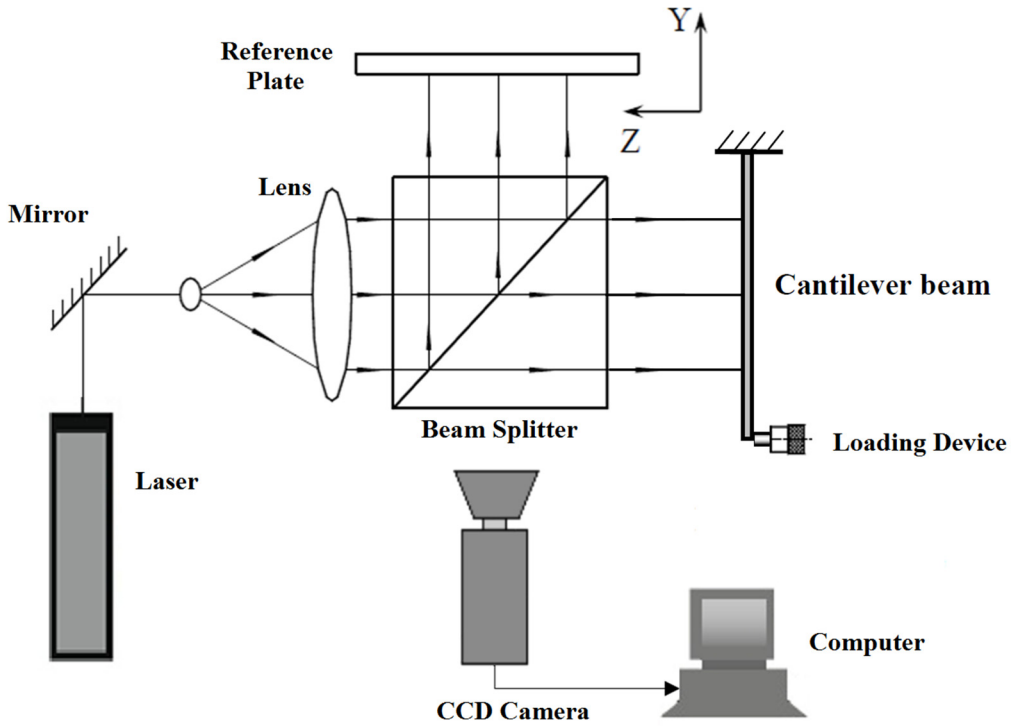

Figure 4.6 A schematic setup for material characterization of a cantilever beam.

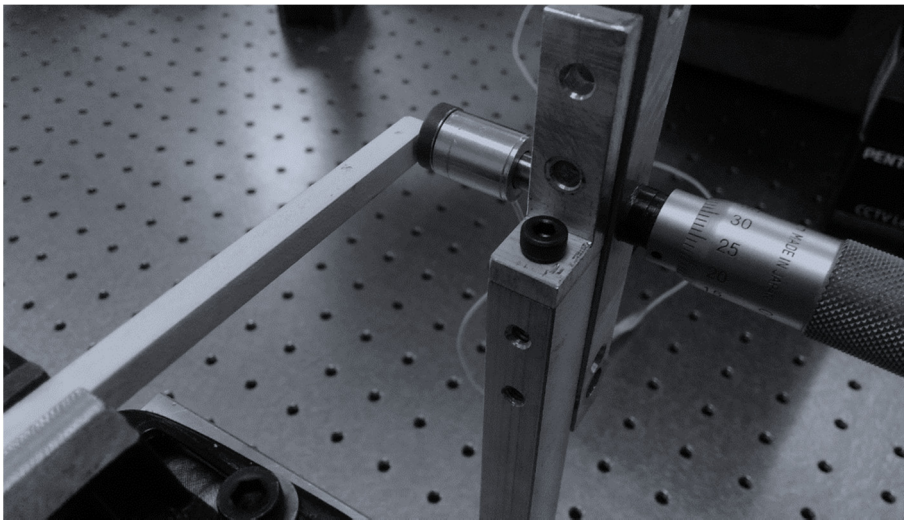

Figure 4.7 Magnesium nanocomposite cantilever beam loading setup.

4.2.3 Time-average DSPI for vibration analysis

A schematic diagram of the experimental setup is shown in Fig. 4.8. A function generator which is attached with a shaker provides a harmonic excitation on the specimen as shown in Fig. 4.9 and 4.10. The specimen is a thin circular plate ,clamped at its edge, with diameter of

65 mm and thickness of 1.6 mm and it is made of aluminum 6061-T6 alloy which has an elastic modulus 69 GPa and a Poison's ratio 0.33. A HeNe laser source of wavelength 632.8 nm and Manta G-046B monochrome camera, which has Sony ICX415 CCD sensor with 582 × 780 pixels of size 8.3 μm, are used to capture interference patterns. Amplitude of the harmonic excitation is manually varied using a function generator i.e. one time-average frame of the plate vibrating at some amplitude is captured first and another time-average frame of the same plate vibrating with a small change in the amplitude (5%), is captured next. These two time average frames captured are then subtracted digitally using UU software. However, this process could be automated by a simple program which controls both the function generator and the CCD camera.

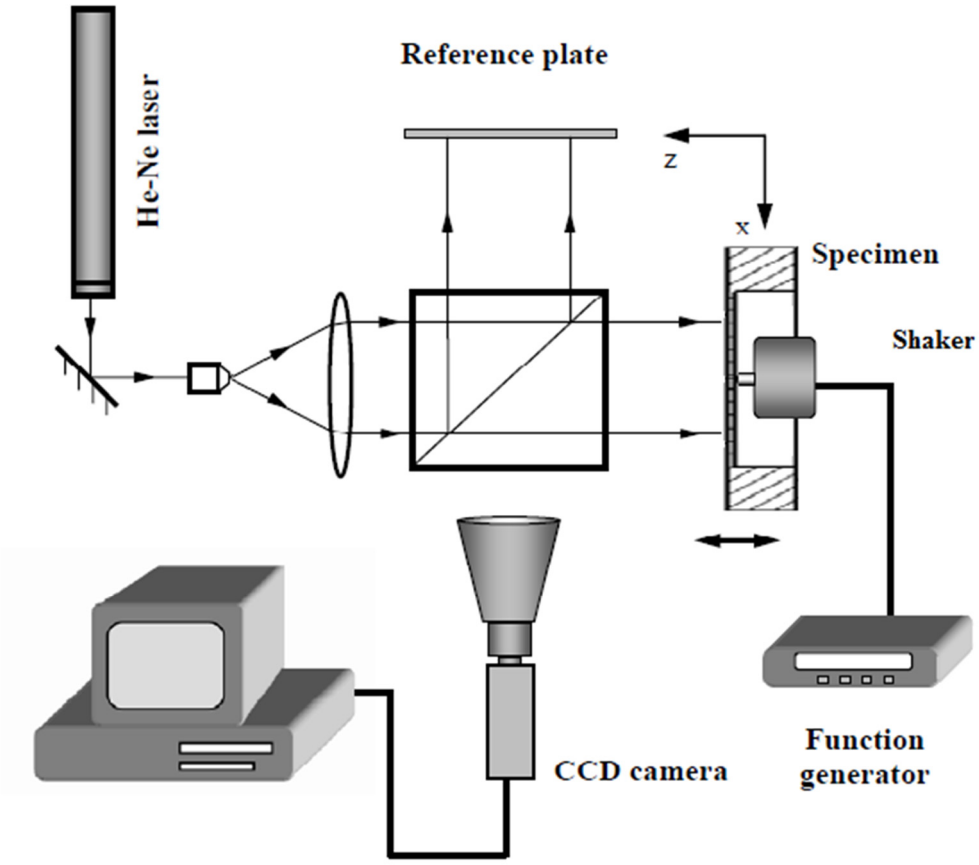

Figure 4.8 A schematic diagram of a TA-DSPI experimental setup.

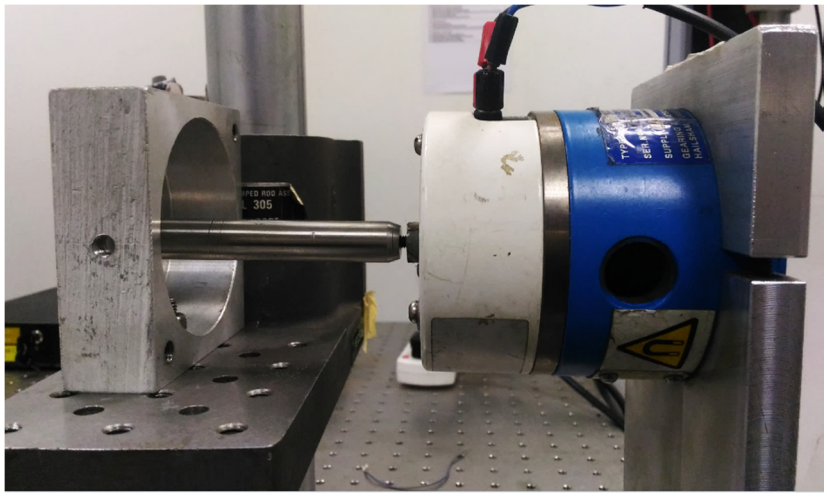

Figure 4.9 Shaker and a thin circular aluminum plate – dynamic loading setup.

Figure 4.10 Function generator and amplifier setup.

4.3 Digital speckle shearing interferometry (DSSI)

A schematic diagram of DSSI experimental setup for measuring the out of plane deformation derivatives is shown in Fig. 4.11. A coherent light beam is directed at a thin circular plate specimen. The light beam reflect from the plate is split into two beams.

They are reflected by mirrors 1 and 2 before forming a speckle-interference pattern. The speckle pattern is then captured using a CCD camera. Mirror 2 is attached to a micrometer setup, which facilitates the shearing. A reference speckle pattern is captured before loading. A static loading is applied on the specimen and a shearing is applied by tilting the mirror 2 with a micrometer. The speckle pattern after loading and shearing is captured and subtracted from the reference speckle pattern to produce shearography fringes.

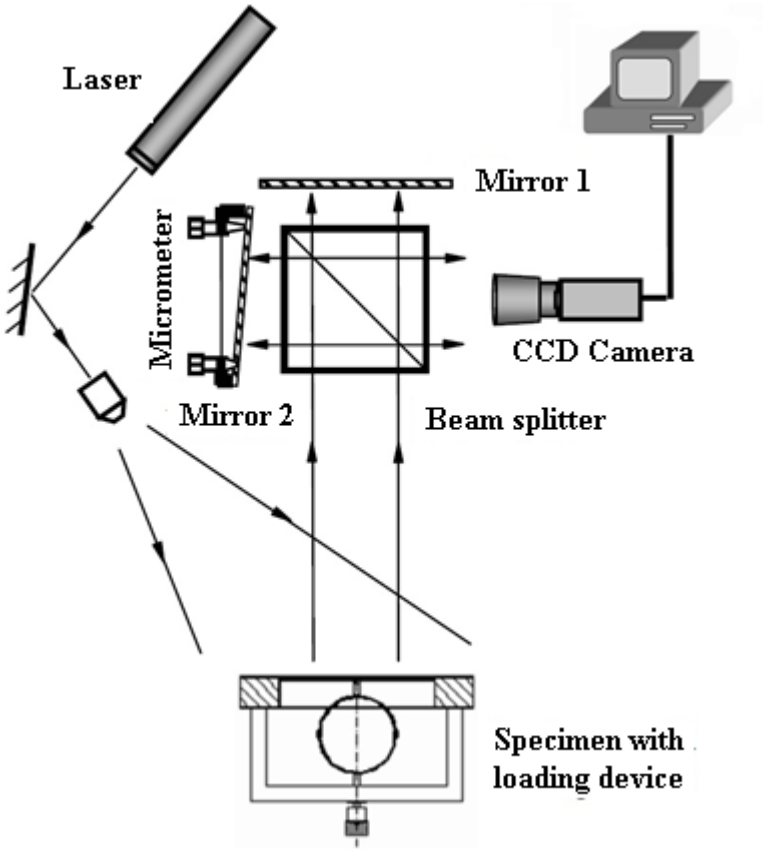

Figure 4.11 A schematic diagram of a DSSI experimental setup.

A HeNe laser source of wavelength 632.8 nm and Manta G-046B monochrome camera, which has Sony ICX415 CCD sensor with 582×780 pixels of size 8.3 μm, are used to capture interference patterns. The same specimen shown in Fig. 4.5 along with the micrometer loading setup is used in this DSSI experiment. The load applied is

measured using the compressive load cell for validation of the strain measurement in the DSSI system.

CHAPTER FIVE

RESULTS AND DISCUSSION

5.1 Fringe quality improvement

5.1.1 Amplitude-varied refreshing reference frame technique in TA-DSPI

Amplitude-varied refreshing reference frame technique is used to capture high quality time-average digital speckle pattern interferometry (TA-DSPI) fringes. A dynamic loading TA-DSPI experiment is carried out to validate the proposed technique. Figure 5.1 shows fringe patterns of mode 2 vibration of a circular plate, which are captured using conventional subtraction from stationary frame technique (Fig. 5.1(a)) at frequency 8050Hz with amplitude 240mV and the proposed amplitude-varied refreshing reference frame technique (Fig. 5.1(b)) at the same frequency between amplitude 120-114mA. Only half of the amplitude applied for stationary frame technique is applied for the proposed technique as the proposed technique produces twice the amount of fringes than its counterpart. It is noticeable that the fringe pattern in Fig. 5.1(a) has black background and Fig. 5.1(b) has white background. In conventional technique, phase zero position always represents a dark fringe. However, in the proposed technique, phase zero can produce either white or dark fringe. Phase zero produces dark fringe, when the reference vibration has lower amplitude value than the second vibration and vice versa.

The figures show that the fringe quality obtained using the amplitude-varied refreshing reference frame technique is far more superior to the conventional technique.

Contrast values of the fringe patterns are calculated for a quantitative comparison and the result shows that the contrast value of a fringe pattern from the proposed method is 0.39, which is far better than the contrast of a fringe pattern from the conventional technique (0.15).

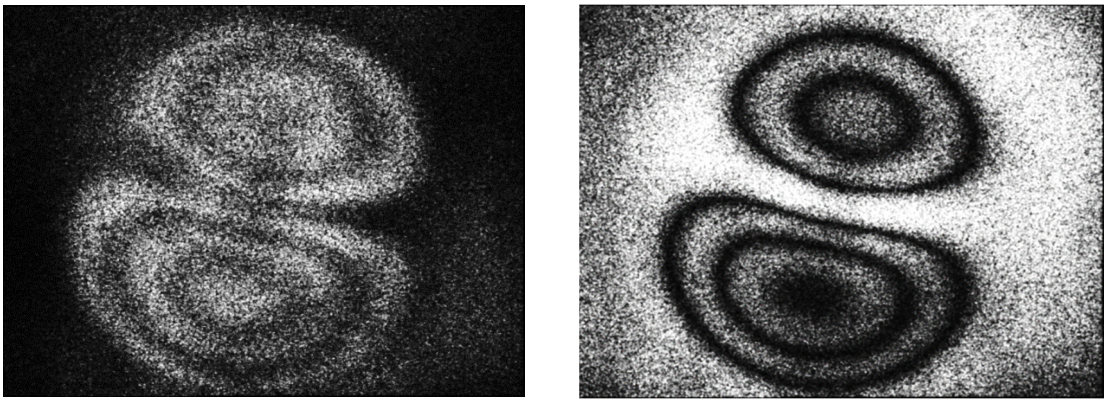

(a) (b)

Figure 5.1(a) TA-DSPI fringes obtained using conventional method; (b) TA-DSPI fringes obtained using proposed method.

A simulation study is carried out to investigate the influence of the amplitude increment factor r on the fringe contrast. Fringe patterns are simulated using Eq. (3.5) with r values of 1%, 2%, 4%, 10%, 20% and 25% as shown in Fig. 5.2(a)-5.2(f) respectively. From these figures, we can see that there is no change in fringe contrast. The mean contrast values for Fig. 5.2(a)-5.2(f) are 0.74, 0.73, 0.73, 0.71, 0.69 and 0.73 respectively. Hence it is evident that the factor r has a very little or zero influence on the fringe contrast for r values less than 25%. However, fringe shapes are noticeably changed for r values 20% and 25% i.e. the central fringes inside the oval patterns are bright for r values 20% and 25% which is different from other fringe patterns. This is caused due to a significant change in fringe locus function.

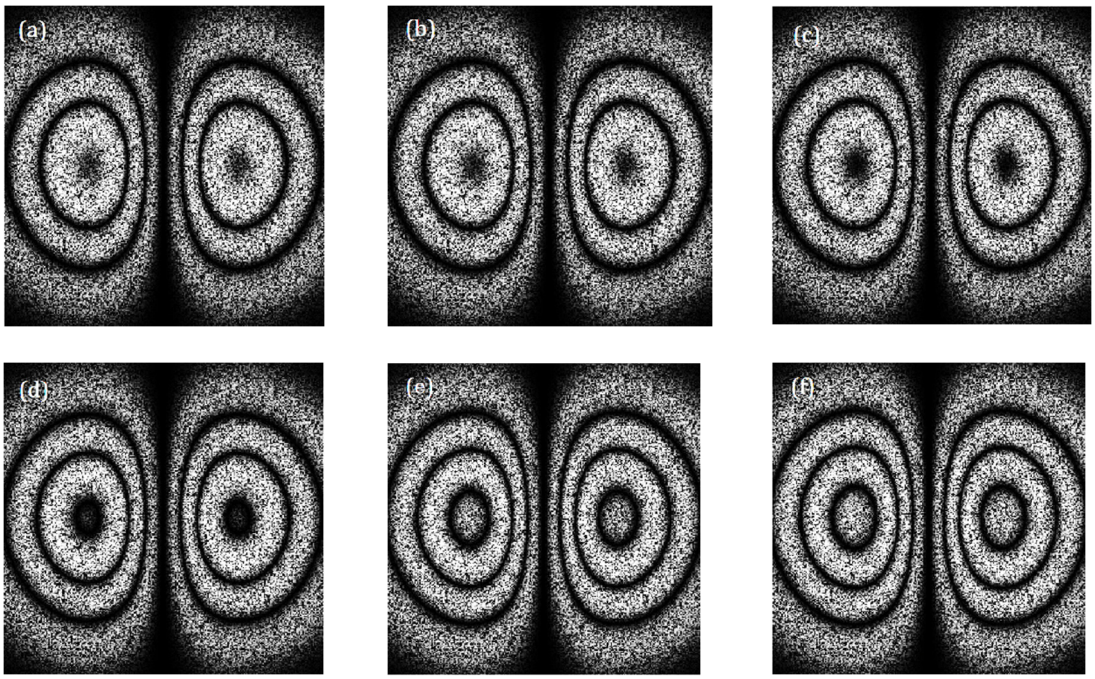

Figure 5.2 (a) Simulated fringe pattern with amplitude increment factor $r = 1\%$; (b) $r = 2\%$; (c) $r = 4\%$; (d) $r = 10\%$; (e) $r = 20\%$; (f) $r = 25\%$.

5.1.2 Mode shape visualization using TA-DSPI and FEM Validation

The specimen is excited at different frequencies and the mode shapes are captured at the resonant frequencies. Resonant frequencies are identified by their large displacements which cause more fringes in the fringe patterns. The fringe patterns at the first five vibration modes are captured at 30 fps using the conventional stationary reference method and using the proposed method. A FEM simulation is carried out using ANSYS to validate the experimental results i.e., to verify the mode shapes and their corresponding resonance frequencies. The fringe patterns obtained from the conventional and proposed method experiments are compared with the FEM modal analysis as shown in Fig. 5.3(a) - 5.3(o). The resonant frequencies at which these modes occur are tabulated in Table. 5.1, and it is noteworthy that both the experimental methods had resonances at same frequencies. For mode 2, 3 and for mode 4, 5, resonances occur at adjacent frequencies in the FEM results, however in reality, it occurs at distinct frequencies, as shown in the experimental results. Though, these four modes (2-5) from FEM

has different orientations from their corresponding experimental fringe patterns, this can be ignored as the specimen is circularly symmetric. Ideally, Mode 2 and Mode 3 obtained from the experiment should be orthogonal, but it is well established in the literature that orthogonal modes which has very little frequency gap would provide superimposed mode shapes (Soedel, 2004). These superimposed modes are not necessarily orthogonal to each other in real experiments. In general, the correlation between mode shapes from FEM and experimental modal analysis are good and the discrepancies in the resonant frequencies are less than 3%. It is also evident from Fig. 5.3 that the proposed method provides better fringe quality for the same amplitude and frequency than the conventional method. FEM modal analysis can provide only Eigen values and vectors which represent natural frequencies and corresponding mode shapes. Hence the amplitude values shown in the FEM results are arbitrary so they should be ignored.

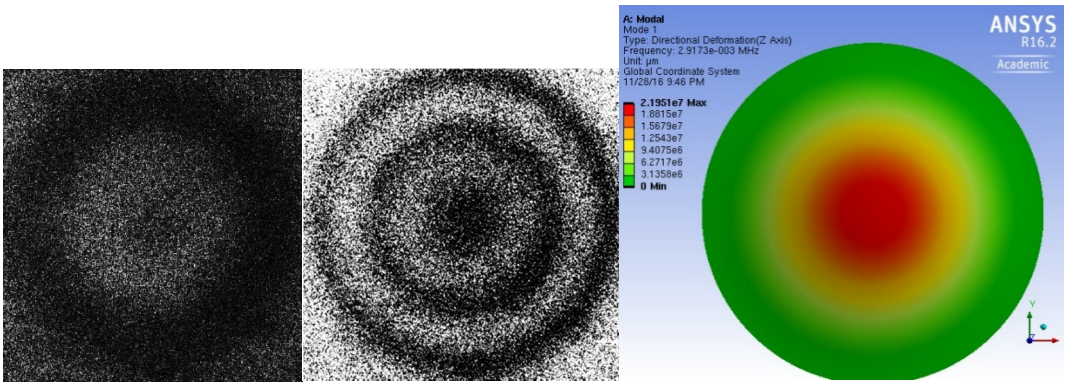

(a) **(f)** **(k)**

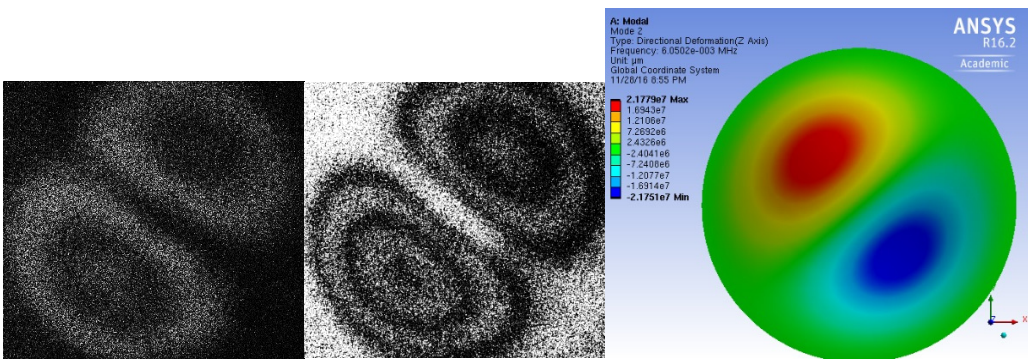

(b) **(g)** **(l)**

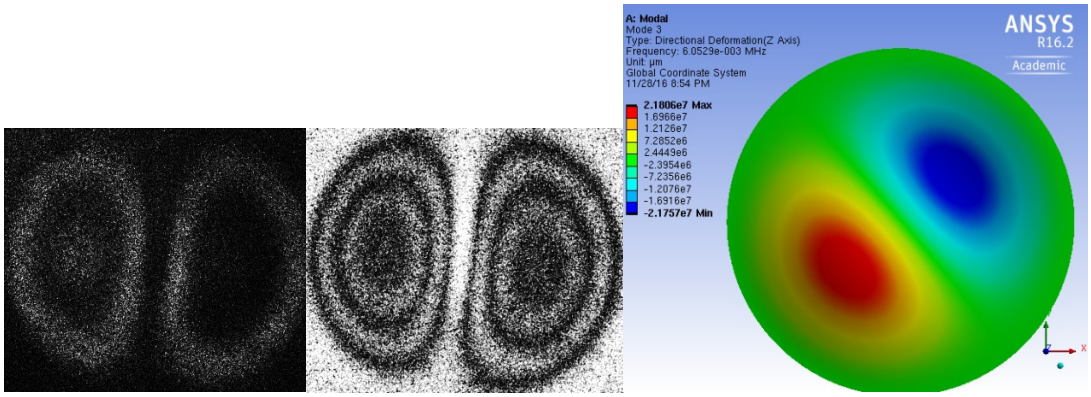

(c) **(h)** **(m)**

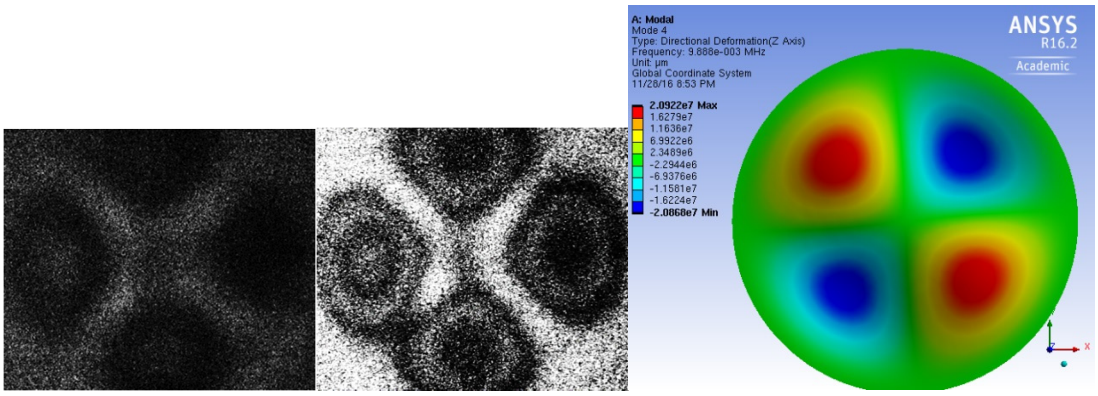

(d) **(i)** **(n)**

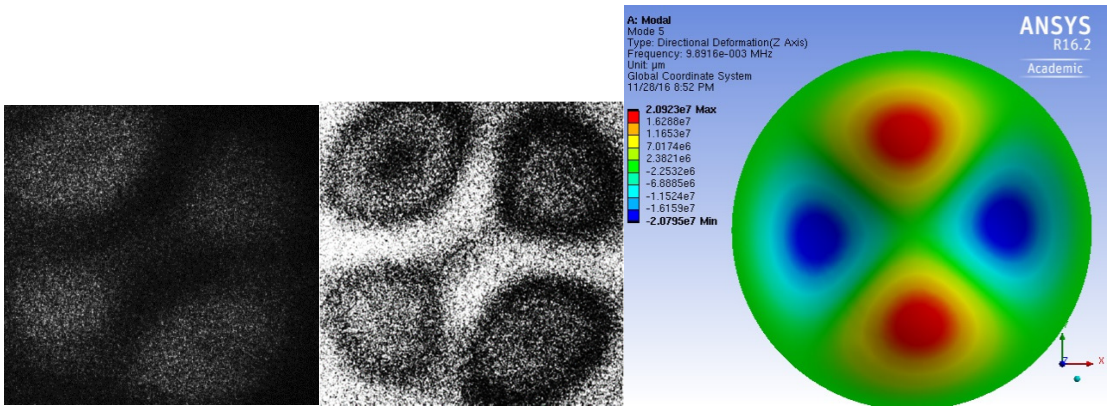

(e) **(j)** **(o)**

Figure 5.3(a) TA-DSPI (stationary reference method) experimental fringe pattern of a circular plate vibrating in mode1; (b) mode 2; (c) mode 3; (d) mode 4; (e) mode 5; (f) TA-DSPI (amplitude-varied refreshing reference frame method) experimental fringe pattern of the same plate vibrating in mode1; (g) mode 2; (h) mode 3; (i) mode 4; (j) mode 5; (k) Mode shapes (obtained from FEM simulation) of a circular plate vibrating in mode 1; (l) mode 2; (m) mode 3; (n) mode 4; (o) mode 5.

Table 5.1 Comparison between experimental and FEM modal analysis.

	FEM Result (Hz)	Experimental Result (Hz)	Deviation
Mode 1	2917.3	2886	-1.07%
Mode 2	6050.2	6006	-0.73%
Mode 3	6052.9	6042	-0.18%
Mode 4	9888	9633	-2.58%
Mode 5	9891.3	9773	-1.20%

5.2 Phase and phase derivatives from complex amplitude using Teager operator - DHODA

A simulated complex amplitude signal (512×512 pixels) generated using Eq. (5.1) is shown in Fig. 5.4(a). Noise η of 10 SNR is added and the corresponding phase map φ_s is shown in Fig. 5.4(b). The first and second order phase derivatives in the x direction $\dot{\varphi}_x(m,n)$ and $\ddot{\varphi}_{xx}(m,n)$ are shown in Figs. 5.4(c) and 5.4(d) respectively; the corresponding error maps $\dot{e}_x(m,n)$ and $\ddot{e}_{xx}(m,n)$ are shown in Figs. 5.4(e) and 5.4(f) respectively. Similarly, the first and second order derivatives in the y direction $\dot{\varphi}_y(m,n)$ & $\ddot{\varphi}_{yy}(m,n)$ and their corresponding error maps $\dot{e}_y(m,n)$ & $\ddot{e}_{yy}(m,n)$ are shown in Figs. 5.4(g) – 5.4(j). A phase map $\varphi(m,n)$ determined from integration of phase derivatives maps is shown in Fig. 5.4(k).

$$CP_s = \exp(j[\varphi_s(m,n)]) + \eta \tag{5.1}$$

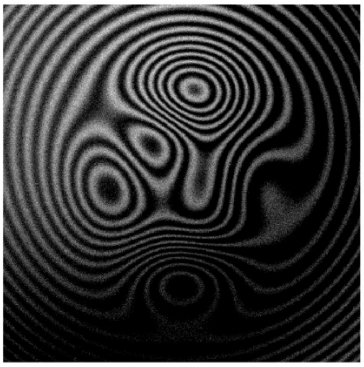

(a)

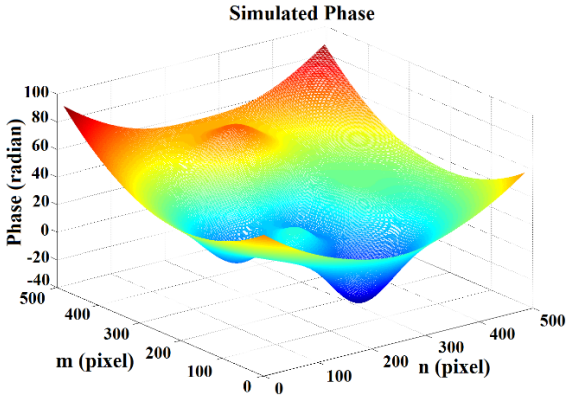
Simulated Phase
Phase (radian)
m (pixel)
n (pixel)

(b)

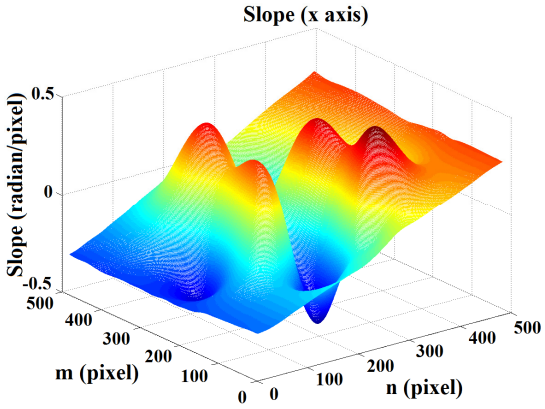
Slope (x axis)
Slope (radian/pixel)
m (pixel)
n (pixel)

(c)

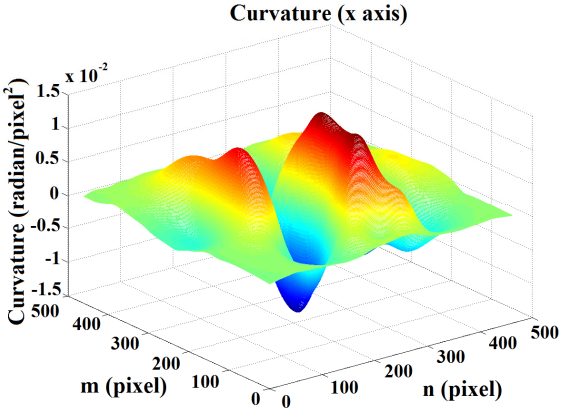
Curvature (x axis)
x 10-2
Curvature (radian/pixel2)
m (pixel)
n (pixel)

(d)

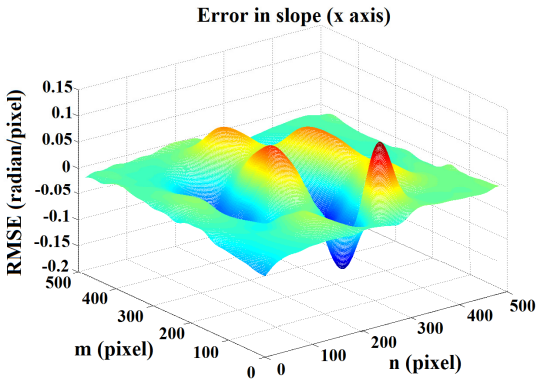
Error in slope (x axis)
RMSE (radian/pixel)
m (pixel)
n (pixel)

(e)

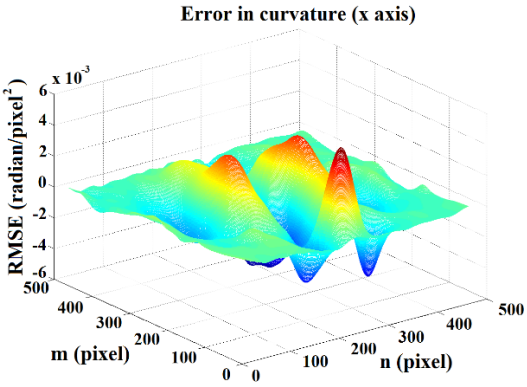
Error in curvature (x axis)
x 10-3
RMSE (radian/pixel2)
m (pixel)
n (pixel)

(f)

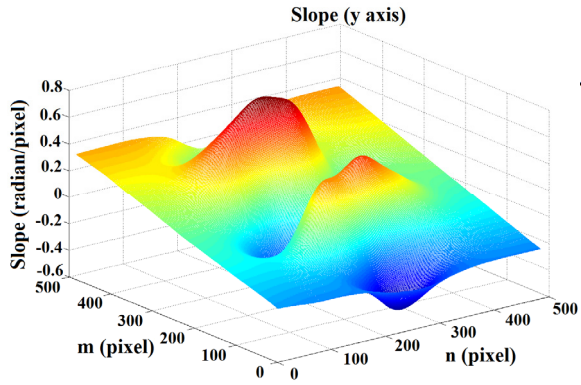

(g)

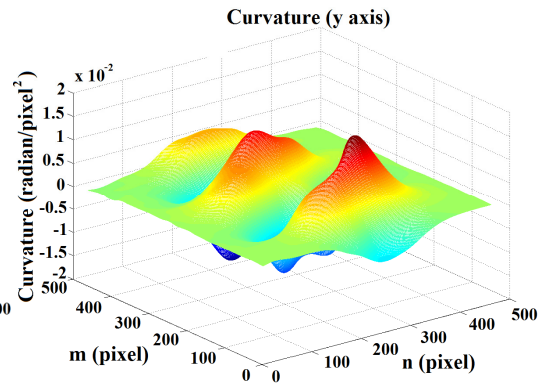

(h)

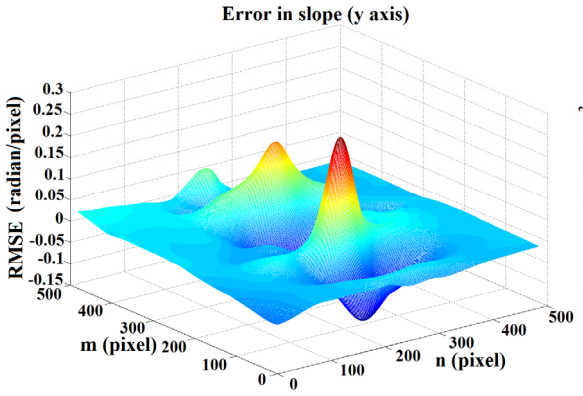

(i)

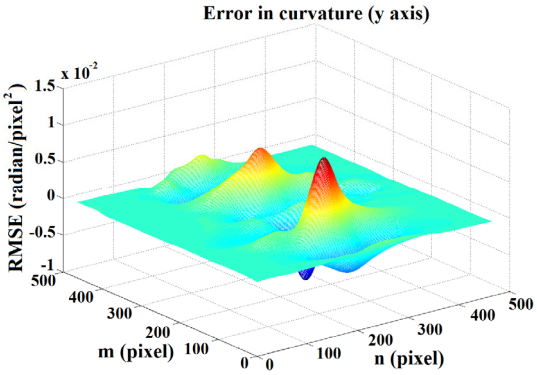

(j)

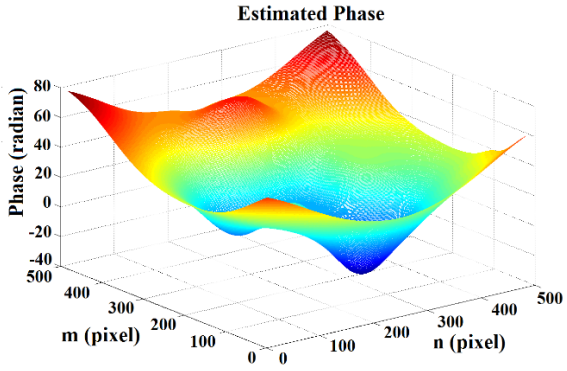

(k)

Figure 5.4(a) Simulated complex signal with noise (real part); (b) Phase map of the signal; (c) First order phase derivative in *x* direction; (d) Second order phase derivative in *x* direction; (e) Error map of first order derivative; (f) Error map of second order derivative; (g) First order phase derivative in *y* direction; (h) Second order phase derivative in *y* direction; (i) Error map of first order derivative; (j) Error map of second order derivative; (k) Estimated Phase map.

The proposed algorithm requires 41 seconds to compute both the first and second order derivatives in both directions (fringe pattern 512×512 pixels). The root mean square error calculated for the first and second order phase derivatives in the x and y directions are 0.0293, 1.0×10^{-3} and 0.0331, 1.3×10^{-3} respectively. It is seen that the phase derivatives obtained from the simulation show less discrepancy. The maximum discrepancy for the first and second order phase derivatives are 0.124 radian/pixel and 5.5×10^{-3} radians/pixel^2 respectively and few regions show large deviations as is evident from the low RMSE values.

5.2.1 Robustness and accuracy analysis of proposed method

A study on effectiveness, accuracy and computation speed of the proposed technique is carried out to compare with the vortex operator (VO) with virtual sheering complex phasor and VO with discrete energy separation algorithm (DESA) methods. The phase and phase derivative maps are determined for a 512×512 pixel fringe pattern shown in Fig. 5.4(a) and the root mean square errors and computation time are shown in Table. 5.2. The phase derivatives from a complex amplitude signal are determined by the virtual sheering complex phasor, DESA and discerete high order demodulation algorithm (DHODA) methods. The errors introduced by the virtual sheering complex phasor method are relatively larger than that of DESA and DHODA and it also requires a larger computation time. This is mainly due to the fact that a separate phase unwrapping method is required. This in turn increases the computation time and complexity. In this study, Goldstein's branch-cut unwrapping method is used. The errors are also affected by the quality of the unwrapping process. Teager-Kaiser energy based methods i.e., DESA and DHODA, require relatively less computation time compared with the aforementioned methods and are also able to provide more accurate phase derivatives. The methods determine phase derivatives directly and the phase values are obtained by numerical

integration of the phase derivatives. Even minor deviations in the phase derivatives would result in large errors after integration. Hence the errors of the phase values are relatively higher. However, the phase derivatives determined using the proposed method are more accurate. Hence the proposed method is suitable for dynamic strain, twist and curvature measurements. Out of the two Teager-Kaiser energy based methods, DHODA uses a higher order energy operator. In general, a two-dimensional operator would be less sensitive to noise than its one dimensional counterpart. Two dimensional DESA is an extension of 1D DESA along the horizontal and vertical axes but DHODA analyzes the frequency in more directions (such as the diagonals) apart from the vertical and horizontal. Hence DHODA is able to track the frequencies more effectively than both 1D and 2D DESA. A comparison between 1D DESA, 2D DESA and DHODA is also carried out and results are shown in Fig. 5.5(a)-5.5(g). A complex signal with SNR=2 (amplitude of signal to amplitude of noise ratio), demodulated with DHODA, 1D DESA and 2D DESA is shown in Fig. 5.5(a) (real part) and the slope and error maps are shown in Figs. 5.5(b)-5.5(g). The RMSE values of the slope calculated by DHODA, 1D DESA and 2D DESA are 0.0263, 0.0274 and 0.0323 respectively.

Table 5.2 Comparison between different phase derivative determination algorithms.

	RMSE – error in slope (radian/pixel)	RMSE error in curvature (radian/pixel^2)	RMSE error in Phase (radian)	Time taken for computation (sec)
Complex Phasors (with phase unwrapping)	0.0522	0.0036	1.180	81.5
DESA	0.0403	0.0013	2.770	42.3
DHODA	0.0293	0.0010	1.824	40.8

(a)

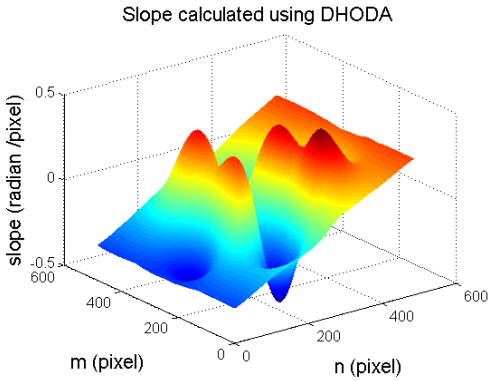

(b)

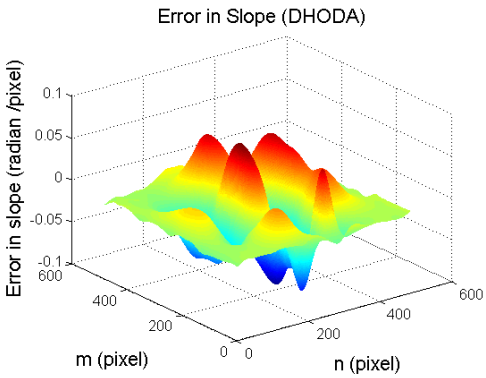

(c)

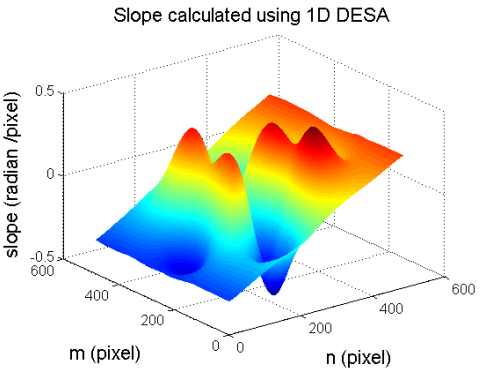

(d)

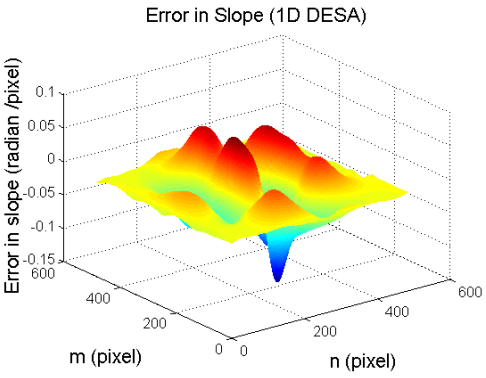

(e)

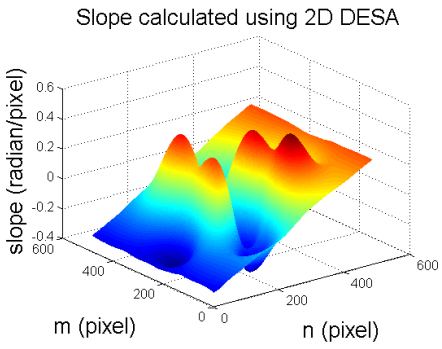

(f)

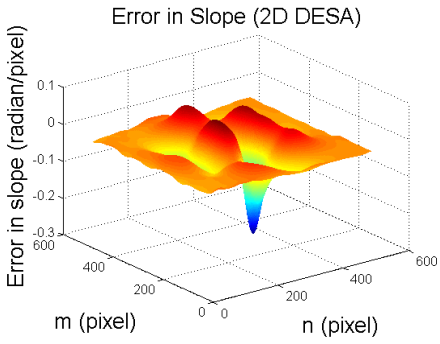

(g)

Figure 5.5 (a) Simulated complex signal (real part); (b) First order phase derivatives in *x* direction determined using DHODA; (c) Corresponding error map; (d) First order phase derivatives determined using 1D DESA; (e) Corresponding error map; (f) First order phase derivatives determined using 2D DESA; (g) Corresponding error map.

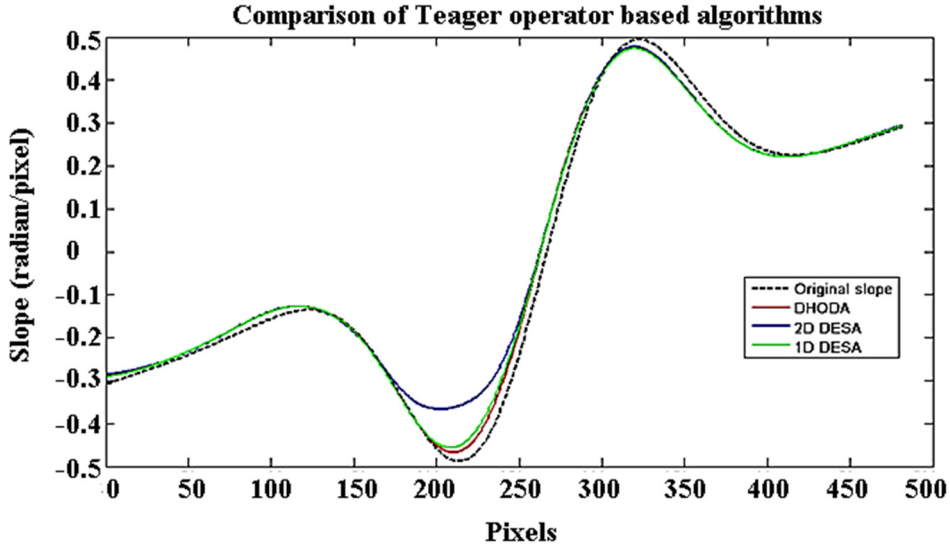

Figure 5.6 Comparison Teager-Kaiser energy operator based algorithms.

In Fig. 5.6, the actual slope values of a particular row (m=116) of a simulated signal is compared with the estimated values using DHODA, 1D DESA and 2D DESA. It is seen that for pixels from 170 to 250, 2D DESA values show large deviations from the actual values and the DHODA values show less discrepancies. The results show that the errors introduced by DHODA are less than that of 1D DESA and 2D DESA though they all require approximately the same computation time. On the whole, the proposed method (DHODA) outperforms the other methods in accuracy and computational time in phase derivative determination.

For DSPI fringes, the phase derivatives are obtained from the fringe patterns. Hence the sequential algorithm called Teager-Hilbert-Huang algorithm, is proposed. Due to the sequential processing, various parameters such as noise level, fringe density and window size affect the overall performance of the method. Hence it is important to study the influence of these parameters. Window size is a parameter which affects both the quality of the orientation map and computation time. Though the accuracy of the orientation map would only introduce

a minor error, large deviations of the orientation however could have significant effect on the overall results. To obtain accurate results in the orientation map, the window size of the plane fit operation should be smaller than the smallest fringe width in a fringe pattern. The relation between window size and fringe width and its effects on phase derivatives are shown in Figs. 5.7(a)-5.7(j). The fringe pattern shown in Fig. 5.7(a) contains different regions with different fringe widths; line A, shown in Fig. 5.7(a), has a fringe width of 12 pixels while line B has a fringe width of 38 pixels. Figures 5.7(b)-5.7(d) show an orientation, first order phase derivative and error map respectively calculated using an 11×11 window size for a plane fit operation. Similarly Figs. 5.7(e)-5.7(g) and Figs. 5.7(h)-5.7(j) show the corresponding maps for window sizes of 17×17 and 25×25 respectively. The orientation map (Fig. 5.7(b)) and slope map (Fig. 5.7(c)), which are obtained using a 11×11 window, shows smaller errors than the slope maps calculated by window sizes of 17×17 and 25×25. The orientation map shown in Fig. 5.7(e) obtained with a 17×17 window, shows relatively small errors in regions where the fringe width is larger than 17pixels. The orientation map shown in Fig. 5.7(h) show erroneous results throughout the entire region as the fringe widths are smaller than 25 pixels in most of the fringe pattern. Hence the results show that window size smaller than the smallest fringe width would provide more accurate results. In this work, the window size is chosen manually but an automated selection of window size based on the fringe width would expedite the entire process.

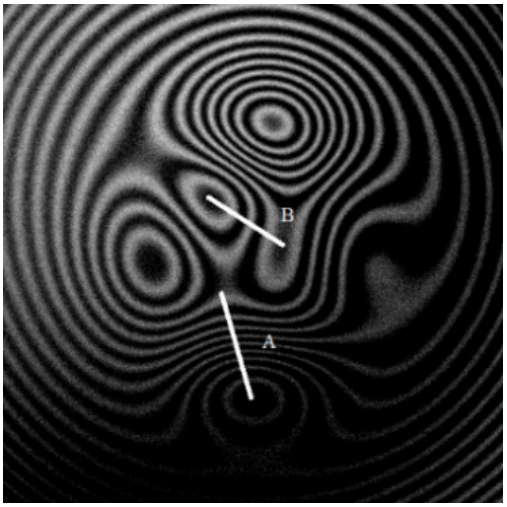
B
A

(a)

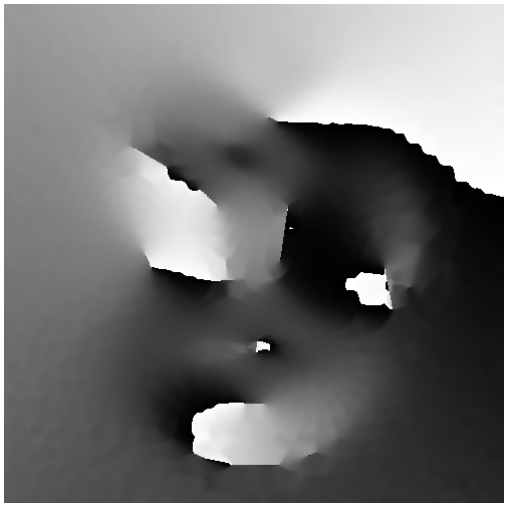

(b)

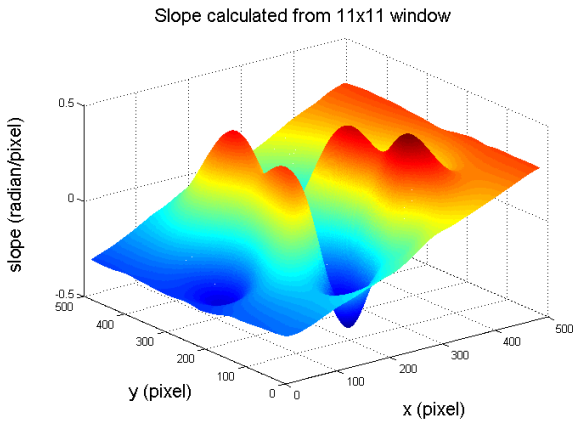
Slope calculated from 11x11 window
slope (radian/pixel)
0.5
0
-0.5
500
400
300
200
100
0
y (pixel)
0
100
200
300
400
500
x (pixel)

(c)

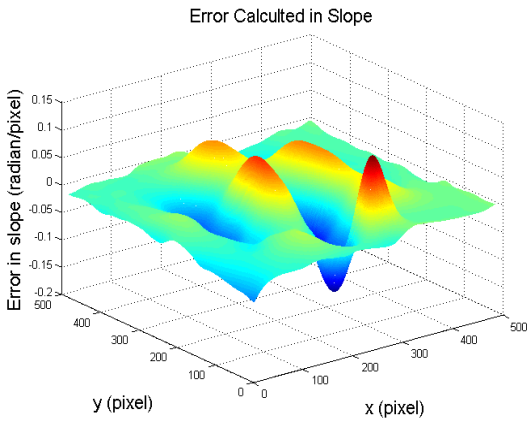
Error Calculted in Slope
Error in slope (radian/pixel)
0.15
0.1
0.05
0
-0.05
-0.1
-0.15
-0.2
500
400
300
200
100
0
y (pixel)
0
100
200
300
400
500
x (pixel)

(d)

(e)

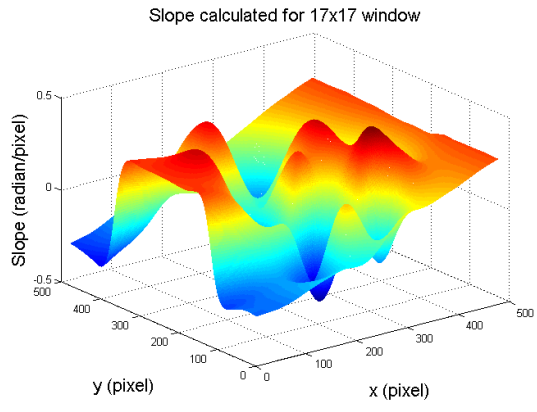
Slope calculated for 17x17 window
Slope (radian/pixel)
0.5
0
-0.5
500
400
300
200
100
0
y (pixel)
0
100
200
300
400
500
x (pixel)

(f)

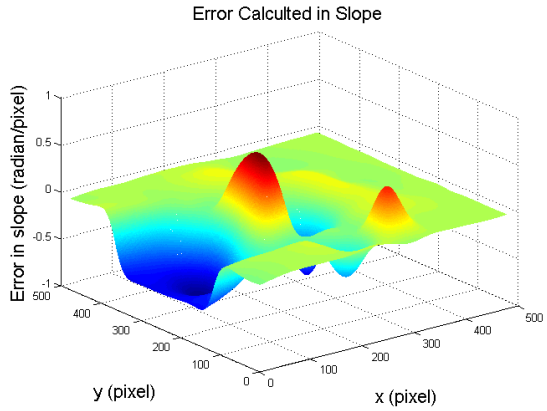

(g)

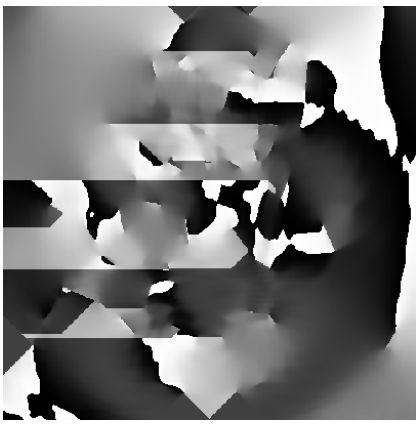

(h)

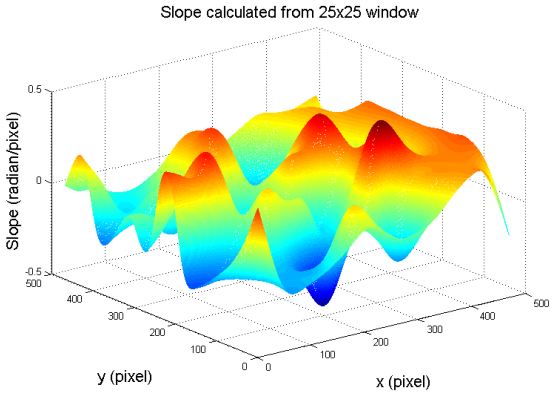

(i)

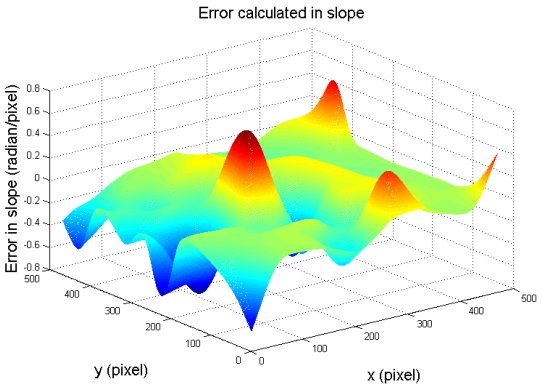

(j)

Figure 5.7 (a) Simulated fringe pattern; (b) Orientation map calculated with an 11×11 pixel window; (c) First order phase derivatives in x direction; (d) Corresponding error map; (e) Orientation map calculated with a 17×17 pixel window; (f) First order phase derivatives; (g) Corresponding error map; (h) Orientation map calculated with a 25×25 pixel window; (i) First order phase derivatives; (j) Corresponding error map.

Speckle noise level, background and contrast would also affect the quality of the interferograms. Hence ASR-EFEMD is employed for normalization and speckle filtering. The significance of the noise removal and normalizaion process in the proposed method is validated with a simple analysis. The proposed method is employed on a noisy fringe pattern shown in Fig. 5.8(a) with and without normalization and noise removal. Slope maps obtained with employing the ASR-EFEMD normalization is shown in Fig 5.8(b) and without employing any normalization and noise removal process is shown in Fig. 5.8(c). The slope error achieved with

ASR-EFEMD normalization is 0.01 radian/pixel, which is more accurate than the slope error value of 0.34 radian/pixel achieved without employing any noise removal process. From these results, it is obvious that normalization and noise removal are important processes for the proposed fringe analysis method and ASR-EFEMD is an effective tool for that.

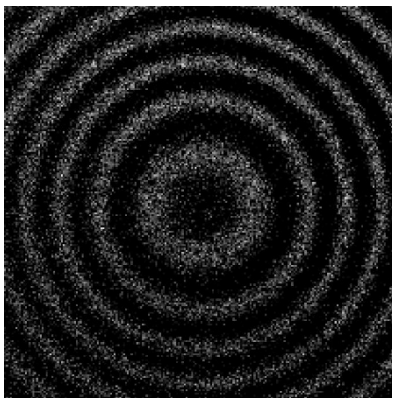

(a)

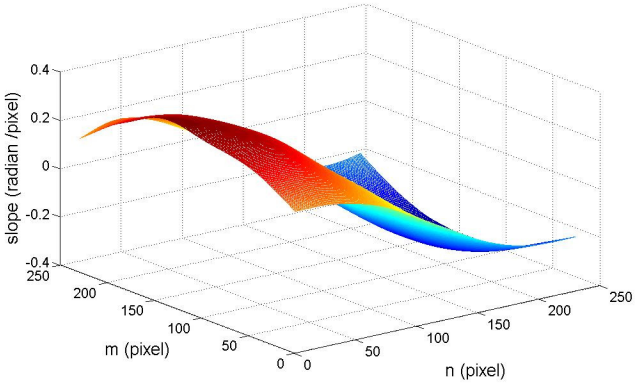

(b)

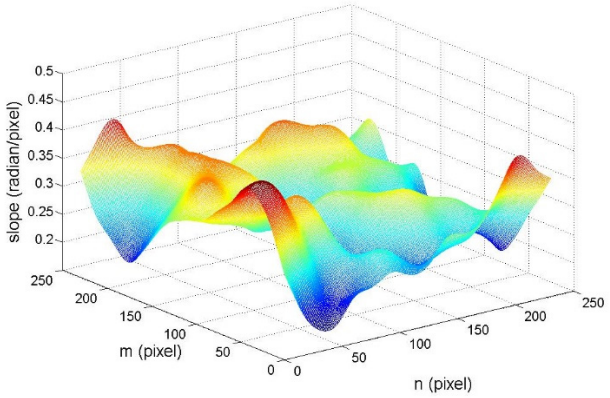

(c)

Figure 5.8 (a) Simulated fringe pattern; (b) Slope map with noise removal; (c) Slope map without noise removal;

Though noise and background variation can be removed by ASR-EFEMD normalization, noise level would still have an effect on the overall effectiveness of the proposed method. To study the effect of noise, the first and second phase derivatives are determined using the proposed method for a series of fringe patterns with SNR varying from 1 to 100 and the results are shown in Figs. 5.9(a)-5.9(b). It is seen that the errors are large for a signal with

SNR=1 and decrease with higher SNR values. However the decrease in error is not significant after SNR=2. This shows that enhanced fast empirical mode decomposition (EFEMD) is more effective in filtering noise and that the proposed algorithm is able to produce better quality phase derivatives even with SNR values as low as 2.

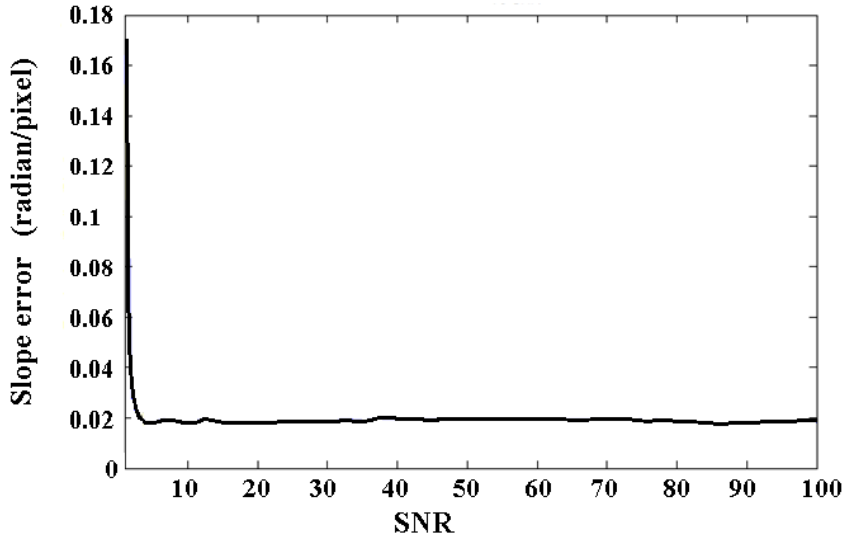

(a)

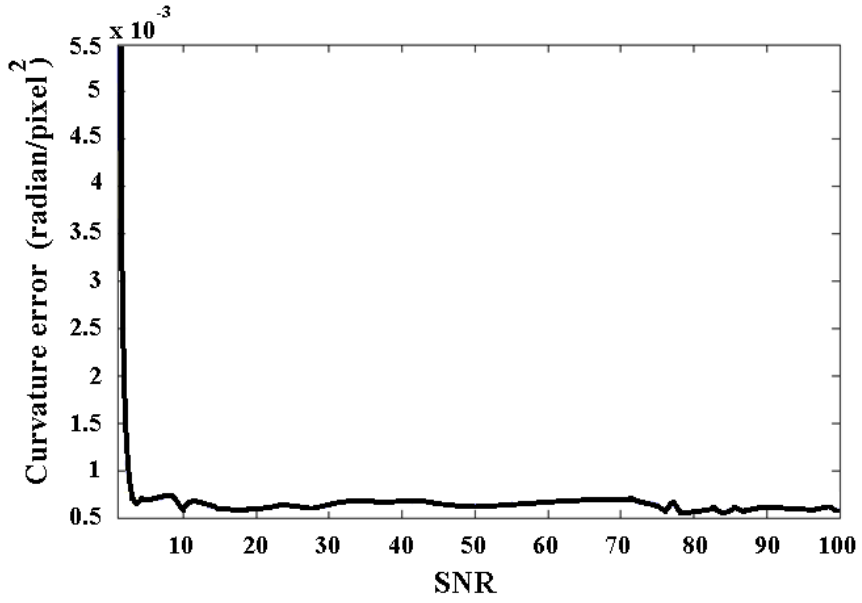

(b)

Figure 5.9 (a) RMSE error of first order phase derivatives versus noise (SNR values); (b) RMSE error of second order phase derivatives versus noise (SNR values).

5.2.2 Digital holographic interferometry

The holograms obtained from the digital holography experiment before and after loading are shown in Fig. 5.10. The complex amplitude signal obtained from the complex phasors method is used to validate the proposed DHODA based phase derivatives determination technique and the results are shown in Fig. 5.11. The proposed method is able to determine the unwrapped slope and curvature maps from the DHI complex amplitude signal effectively. However, this signal has less number of fringes which means it has low instantaneous frequency values which can be easily separated from the carrier frequencies values.

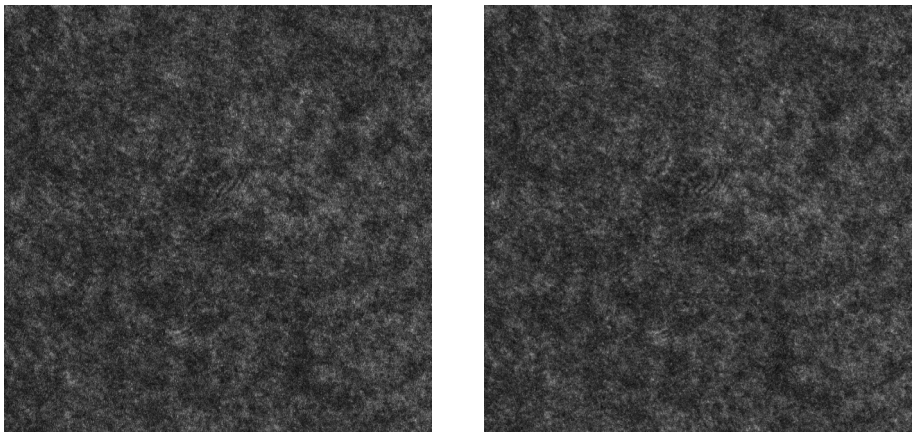

(a) (b)

Figure 5.10 (a) Digital hologram of a thin circular plate recorded before loading; (b) After loading.

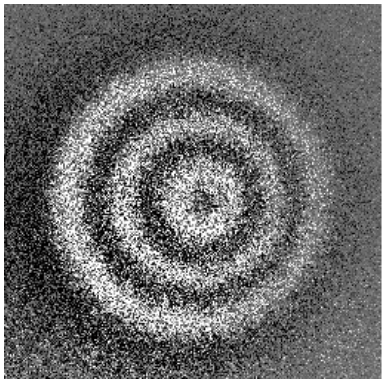

(a)

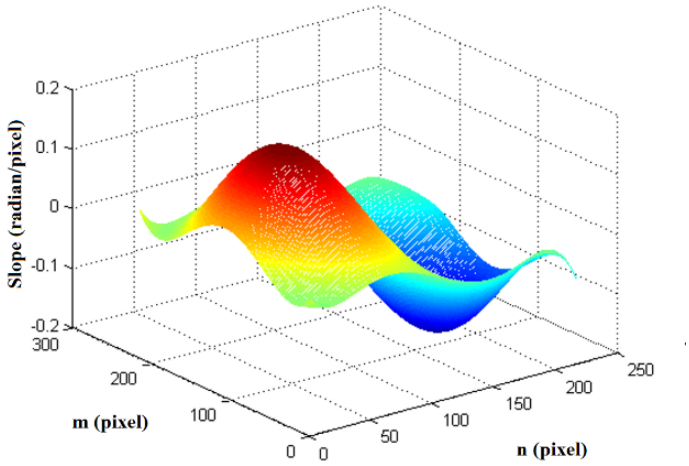

(b)

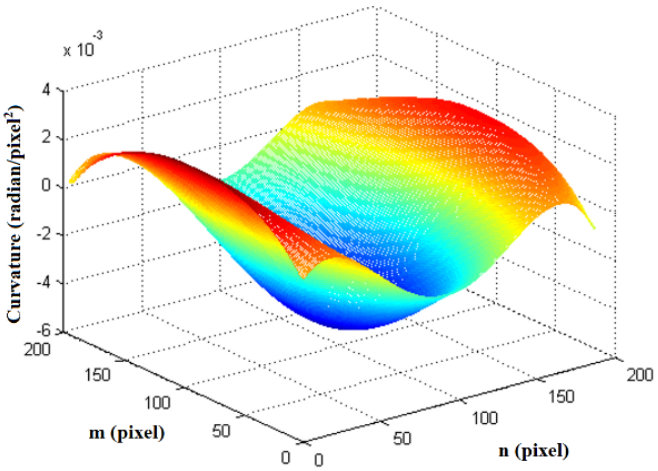

(c)

Figure 5.11 (a) Deformation fringes obtained from DHI; (b) First order phase derivative in *x* direction; (c) Second order phase derivative in *x* direction.

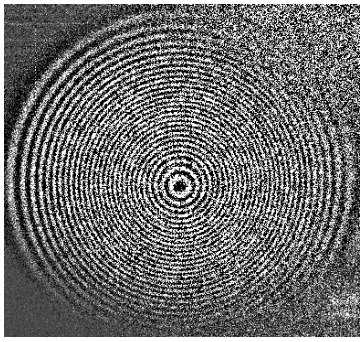

(a)

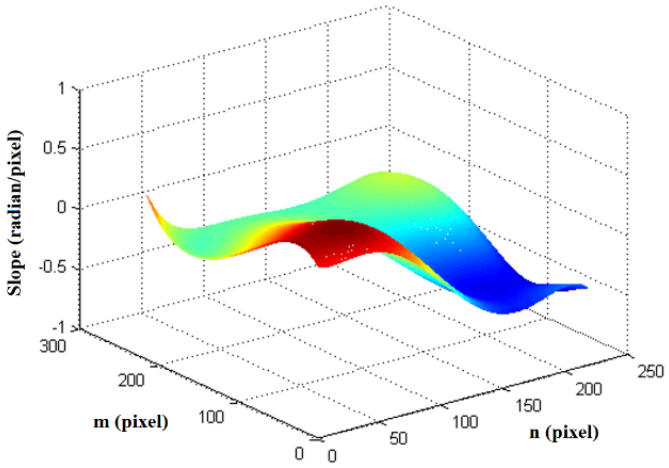

(b)

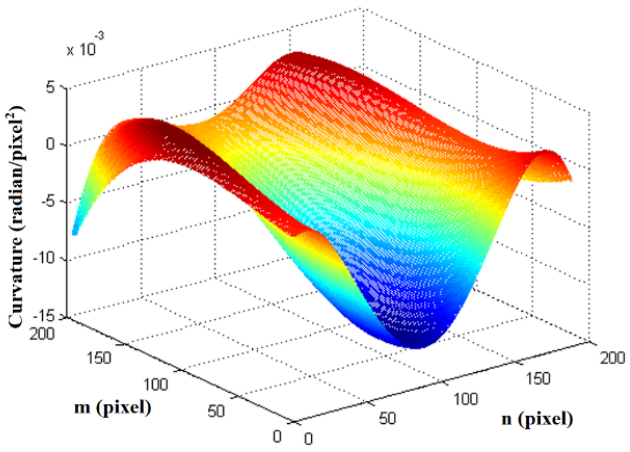

(c)

Figure 5.12 (a) Deformation fringes with high fringe density; (b) First order phase derivative in *x* direction; (c) Second order phase derivative in *x* direction.

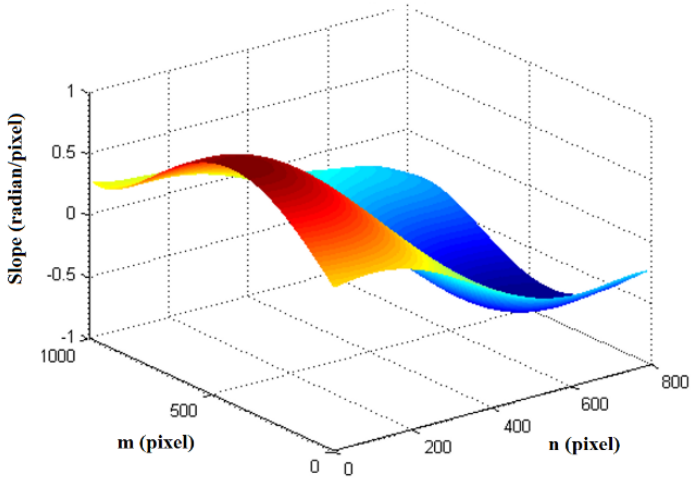

(a)

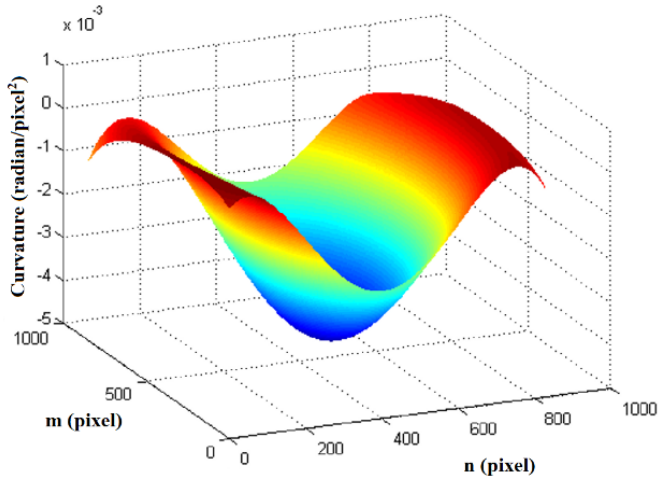

(b)

Figure 5.13 (a) First order phase derivative in *x* direction after zero-padding; (b) second order phase derivative in *x* direction after zero-padding.

To validate the effect of high density fringes (or higher instantaneous frequencies), another set of holograms with a larger applied load is captured. Due to the large load, the phase difference map has higher density fringes resulting in higher instantaneous frequencies. The proposed method is used to obtain phase derivatives and the results are shown in Fig. 5.12. The results show that the proposed method is not

able to determine accurate phase derivatives. Hence an interpolation is carried out by the zero-padding method on complex signal, before applying the DHODA method for phase derivatives determination. Zero-padding provides higher resolution complex signal, which means the complex signal are represented by more pixels (Shinpaugh et al, 1992; Lyons, 2001). Hence the fringe density and instantaneous frequency are reduced. The proposed DHODA method is implemented on higher resolution complex signals obtained from the same holograms and the results are shown in Fig. 5.13. The increase in number of pixels in Fig. 5.13 is caused as a result of zero-padding interpolation. The results show that zero-padding interpolation effectively overcome the high instantaneous frequency problem. Hence the proposed method can be applied for high and low density fringe patterns.

5.2.3 Digital speckle pattern interferometry

The fringe pattern obtained from DSPI for out of plane displacement measurement in a thin circular plate is shown in Fig. 5.14(a). The first and second order phase derivatives in the x direction are shown in Figs. 5.14(b) and 5.14(c) respectively. Likewise, the first and second order phase derivatives in the y direction are shown in Figs. 5.14(d) and 5.14(e) respectively. A phase map obtained by integration of the first order phase derivatives is shown in Fig. 5.14(f). The phase derivatives obtained from the experimental results are well behaved even with high speckle noises.

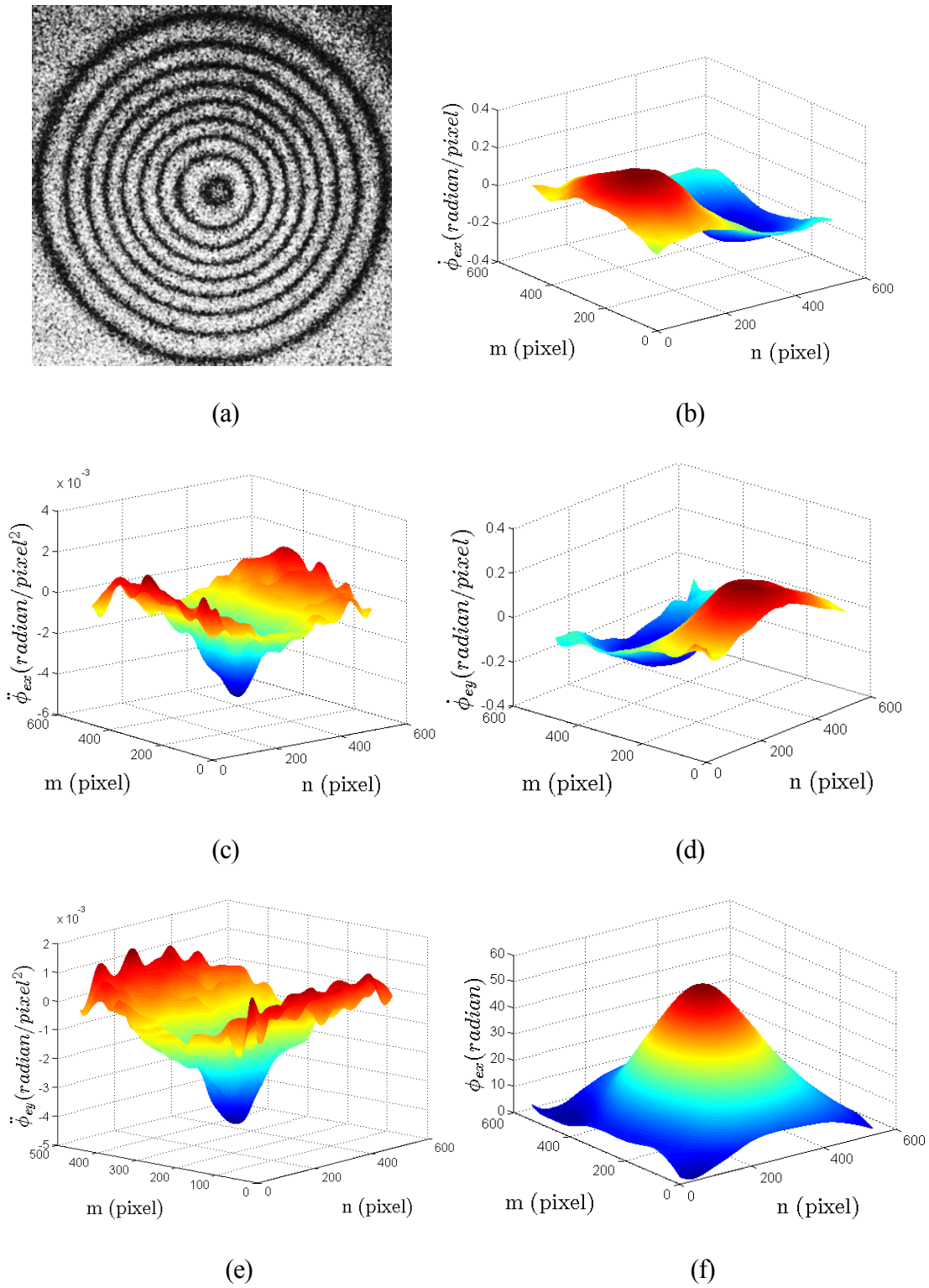

Figure 5.14 (a) DSPI fringe pattern; (b) First order phase derivatives in x direction; (c) Second order phase derivatives in x direction; (d) First order phase derivatives in y direction; (e) Second order phase derivatives in y direction; (f) Phase map estimated by integrating first order phase derivatives.

The central displacement for a circular thin plate with elastic modulus E, Poisson's ratio υ, the radius r_0 and the thickness t loaded with a central point load is given by the following equation.

$$w = \frac{3Pr_0^2(1-\upsilon^2)}{4\pi Et^3} \tag{5.2}$$

For a load of 1.57 N, the theoretical displacement is 2.74 μm, which is in good agreement with the measured value of 2.69 μm. It is noted that, though the proposed method is able to retrieve the phase values and derivatives from a noisy fringe pattern, the measurement sensitivity is still limited by SNR value. Fringes, which do not have enough contrast, could not be processed effectively. However, a temporal phase shifting method, which has a high SNR value, would be more effective, due to its high sensitivity. The proposed method, however, is suitable for phase derivative measurement and in a dynamic situation where it is difficult to capture more than one fringe pattern at each deformed state.

5.3 Phase and phase derivatives using derivative based regularized phase tracker

5.3.1 Simulation study and comparison of proposed method with the RPT method

A simulation study is carried out to verify the effectiveness of the proposed method using a simulated fringe pattern as shown in Fig. 5.15(a) with SNR 5 and the corresponding phase map is shown in Fig. 5.15(b). The proposed algorithm is implemented using MATLAB and requires 60 s (512×512 image) to determine the phase derivatives in both the x and y directions. The

computation time taken for the phase tracking process is 471 s. A specialized minimization algorithm with optimized code will further decrease the computation time. Phase derivatives (in the x direction) obtained using the proposed method is shown in Fig. 5.15(c). The values are compared with that obtained from direct differentiation of the phase map shown in Fig. 5.15(b) and the discrepancies are shown in Fig. 5.15(d). Similarly phase derivatives (in the y direction) and their discrepancies are shown in Figs. 5.15(e) and 5.15(f) respectively. The discrepancies are within -0.08 to 0.08 (radian/pixel). From the derivative maps (Figs. 5.15(c) and 5.15(e)), a phase map is constructed using the proposed technique as shown in Fig. 5.15(g). It is seen that Fig. 5.15(g) is almost identical to Fig. 5.15(b) and the discrepancies as shown in Fig. 5.15(h) are within -0.8 to 0.6 (radians). It is noteworthy that the phase tracking process is carried out row by row with a constant window size.

Results obtained from the proposed method are also compared with that of the RPT and direct integration methods as shown in Figs. 5.16(a) - 5.16(d) and Table 5.3. All these methods do provide unwrapped phase values but the phase values are wrapped in Figs. 5.16(a) – 5.16(d) for better visual comparison. Six critical regions in the simulated wrapped phase map (Fig. 5.16(a)) are indicated. From the results, it is seen that the phase values obtained by simple integration of phase derivatives (Fig. 5.16(b)) show the largest discrepancies compared with Fig. 5.16(a). The deviations of the marked regions 1-6 vary from 6% in region 2 to 50% in region 4. The RPT method is able to demodulate the phase values fairly accurately with deviations of less than 4% in regions 1, 3 and 6 as shown in Fig. 5.16(c). However the accuracy decreases drastically at saddle points especially in region 2 (17%). The proposed method does not show such discrepancies (Fig. 5.16(d)). The deviations at all the 6 regions are less than 4%.

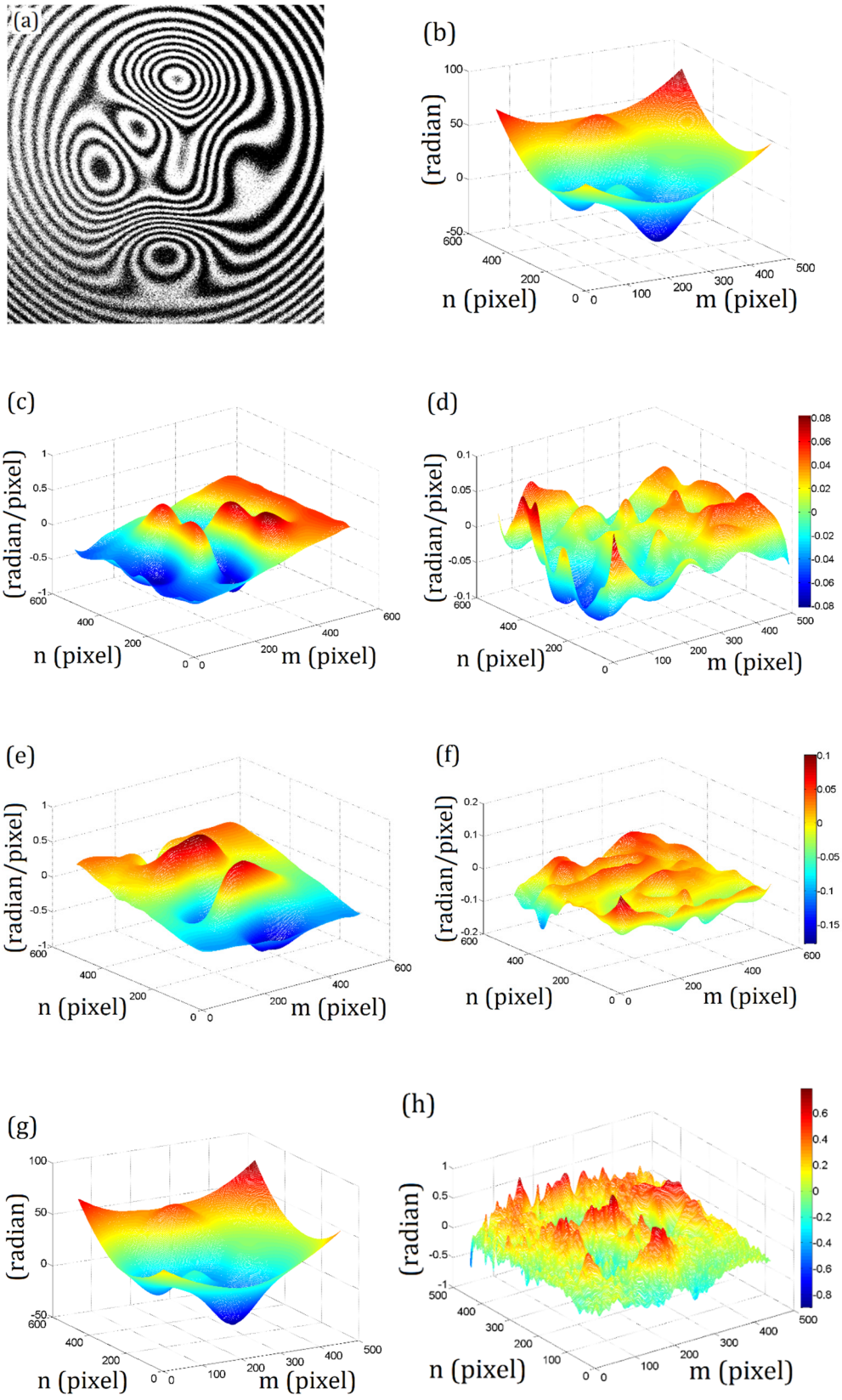

Figure 5.15 (a) Simulated fringe pattern; (b) Simulated phase map; (c) Phase derivatives in x direction; (d) Deviation in phase derivatives in x direction; (e) Phase derivatives in y direction; (f) Deviation in phase derivatives in y direction; (g) Phase map; (h) Deviation in phase values.

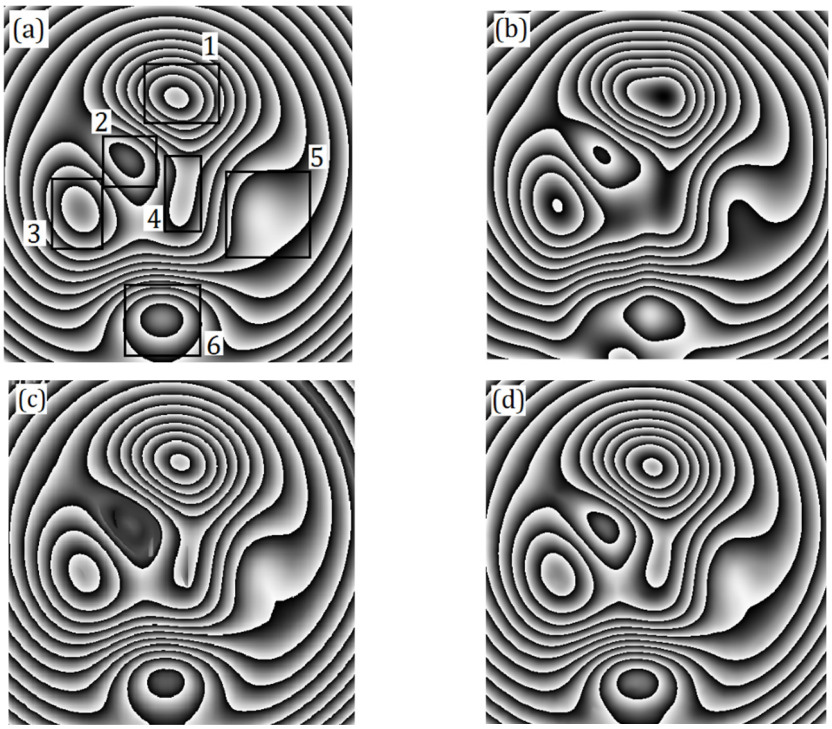

Figure 5.16 (a) Simulated wrapped phase map; (b) Wrapped phase map determined by direct integration of phase derivatives; (c) Wrapped phase map determined by RPT method; (d) Wrapped phase map determined by the proposed method.

Table 5.3 shows the computation time and RMS errors of the various methods employed. As can be seen, though the computation time taken by direct integration of the phase derivatives is the least compared with the RPT and the proposed methods, it shows large discrepancies in the phase values obtained. This is due to the accumulation of errors in the phase derivative values during integration. Compared to the RPT method, the proposed method is able to provide a better accuracy with less computation time. As mentioned earlier, the computation time of the proposed method is reduced due to the reduction in the number of variables and the complexity of the minimization function. Better accuracy is also achieved as the proposed method is able to process the saddle points better than the RPT method. However, using a fringe following technique or a paraboloid phase model, the RPT method would be able to achieve similar accuracy. However, this would be achieved at the expense of higher computation time.

Table 5.3 Comparison of proposed method with RPT.

	Computation Time (s)	RMSE phase error (radian)	RMSE phase derivatives error in x direction (radian/pixel)	RMSE phase derivatives error in y direction (radian/pixel)
Regularized Phase Tracker (RPT)	3300	0.7461	0.0352	0.0381
Direct integration method	60	2.2998	0.0294	0.0324
Proposed method	471	0.1779	0.0294	0.0324

Various parameters like noise level in the fringe pattern, window size to choose the neighborhood for minimization in phase tracker model and regularization parameter β in the phase tracker model would affect the accuracy of the phase estimation. Hence a study to find the effect of these three parameters on the output of the proposed system is carried out using the same simulated fringe pattern as shown in Fig. 5.15(a) with different noise levels.

5.3.1.1 Effect of noise and window size of phase tracker in phase demodulation

In literature, it is shown that the window size in the regularized phase tracker would affect the phase accuracy drastically and a spatially adaptive window size is suggested to overcome this issue on complex fringe patterns with different fringe density at different regions (Kai et al, 2013). The effect of window size in the proposed derivative based simplified phase tracker is analyzed using simulated fringes, which are demodulated with the proposed method with different window sizes. The results are plotted in Fig. 5.17(a). Four fringe patterns with SNR value 2, 3, 5 and 8 represent the four curves. From the results, the general trend obtained is that

the error value is increasing with increase in window size. When a fringe pattern has a constant fringe density these error curves would increment monotonously for values of window size above its fringe width but the simulated pattern, which is used in this study, contains different fringe density at different region. Hence wherever the window size matches with the fringe width, the phase accuracy would be good for that particular region but would suffer in remaining regions. Due to this, the increment in the error is very small till window size of 25 because most of the fringes have width less than 25 pixels. Hence the window size larger than 25 pixel increases the error value more rapidly. Increment in window size would also increases the computational requirement, so it is reasonable to choose a window size smaller than the smallest fringe width of the fringe pattern. In addition to this, it is also evident from the results that the increment in SNR value decreases the error value. However, the difference between SNR 5 and 8 curves are very small which shows that the noise removal by EFEMD is very effective for fringe patterns with SNR value above 5.

5.3.1.2 Effect of regularization parameter of phase tracker in phase demodulation

Regularization parameter β_{reg} ensures the smoothness and continuity of phase demodulation. Hence lower values for regularization parameter causes sharp changes in a phase map. The accuracy of the phase variation with respect to the regularization parameter is studied in a simulated fringe pattern with SNR 5 and the results are plotted in Fig 5.17(b). The error values are shown in logarithmic scale to accommodate high error values and to highlight the differences between window size 5 and window size 18 curves. It is found that regularization parameter values less than 0.5 cause very high discrepancies and values between 0.5 and 3 provide accurate phase values for both curves. The parameter values >3 cause slightly larger error values but they are negligible compared to the error values for parameter<0.5. Hence it is reasonable to choose any parameter value above 0.5.

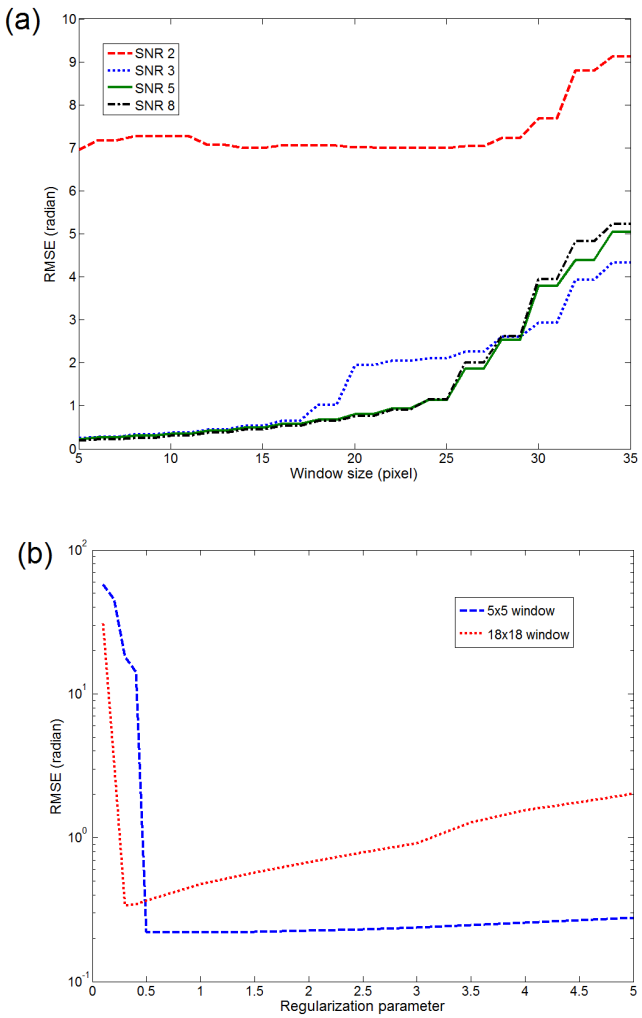

Figure 5.17 (a) Phase error vs Window size; (b) Phase error vs Regularization parameter.

5.3.2 Digital speckle pattern interferometry

The experimental setup for out of plane displacement measuring DSPI is used to capture the fringe pattern shown in Fig. 5.18(a). The derivatives in the *x* and *y* directions are shown in Figs. 5.18(b) and 5.18(c) and the phase values obtained by the derivative based simplified phase tracker is shown in Fig. 5.18(d).

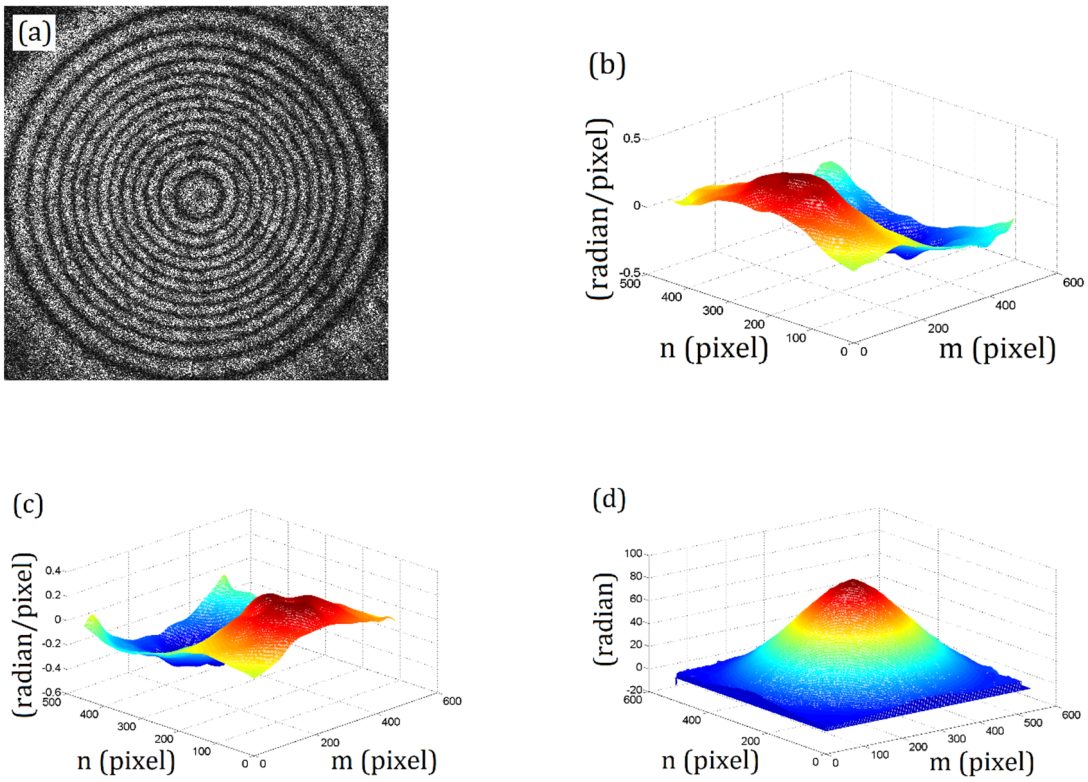

Figure 5.18 (a) DSPI fringe pattern; (b) derivatives in x direction; (c) derivatives in y direction; (d) Phase map.

The phase and phase derivatives obtained from the experimental results are well behaved even with high speckle noises. To validate the phase map quantitatively, the calculated maximum value is compared with the theoretical value calculated using Eq. (5.2). The maximum displacement of 4.43 μm , measured from the experiment data using the proposed method, is in good agreement with the theoretical value of 4.46 μm .

5.3.3 Digital speckle shearing interferometry

An out of plane deformation derivative measurement shearography experimental setup is used to verify the proposed method in the determination of slope, curvature and twist in a thin circular plate. The experimental fringe pattern obtained using DSSI is also utilized to explain the influence of fringe density and B-Spline smoothing in the

accuracy of the phase map determined. The load applied P is measured using a load cell. If the material properties (Young's modulus E and Poisson ratio υ) of the specimen is known, theoretical slope values across the central row of pixels in x direction of the specimen can be calculated using Eqs. (5.3) and (5.4).

$$\frac{\partial w}{\partial x}(m) = \frac{Pr_p(m)}{4\pi D} \ln\left(\frac{r_p(m)}{r_0}\right) \tag{5.3}$$

$$D = \frac{Et^3}{12(1-\upsilon^2)} \tag{5.4}$$

where D is the flexural rigidity of the plate and r_p is the distance of corresponding position from the centre.

A shearography fringe pattern of the specimen, captured for a static load of 2.49 N with a 5-mm shear in the x direction (i.e. horizontal direction) is shown in Fig. 5.19(a). The normalized fringe pattern after EFEMD is shown in Fig. 5.19(b). The fringe gradient angle map and fringe density map are shown in Figs. 5.19(c) and 5.19(d). In Fig. 5.19(d), the center region has high intensity values than the rest of fringe density map as the fringe pattern has more dense fringes in the center. Due to this sharp change in fringe density, the chosen window size is not appropriate anymore in these region. Hence EFEMD normalization left some noise exactly in that high fringe density region as shown in Fig. 5.19(b).

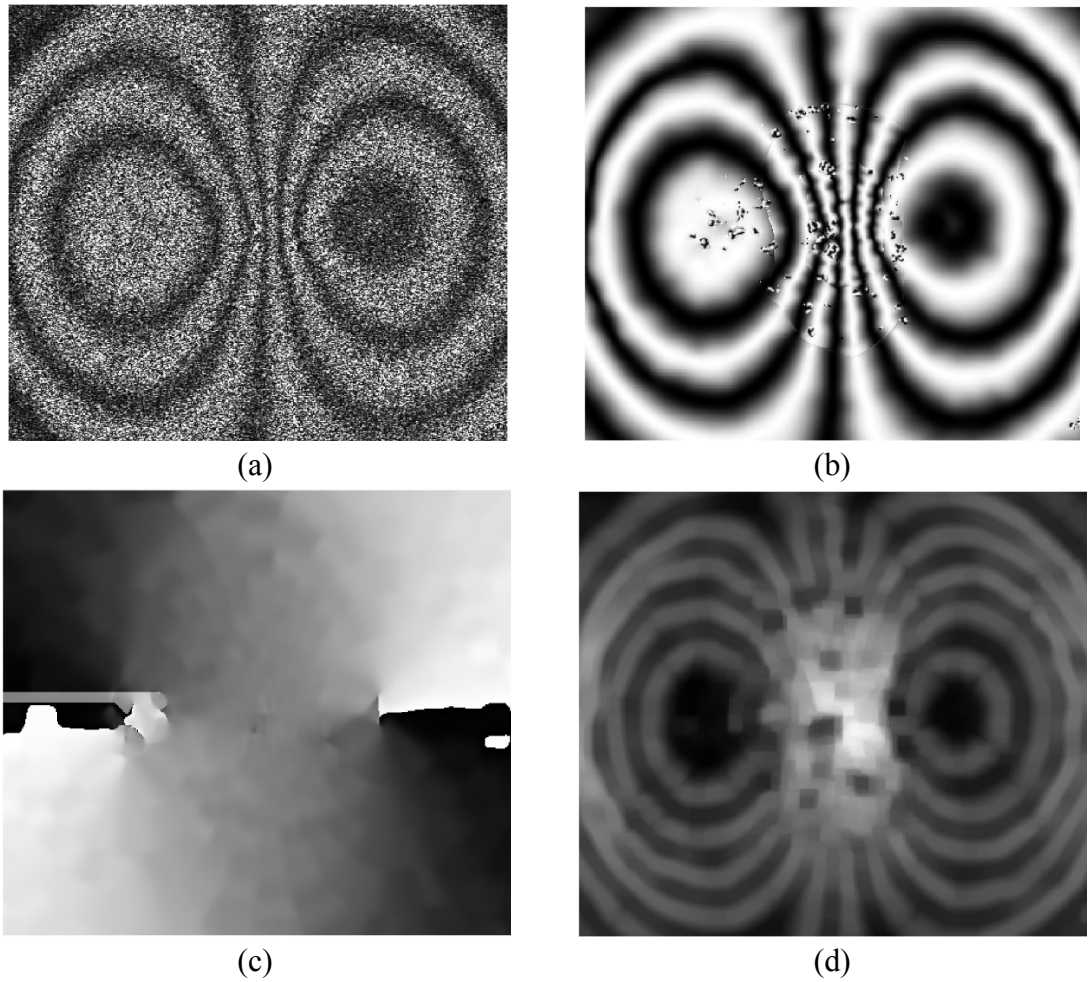

Figure 5.19 (a) Shearography fringe pattern; (b) Normalized fringe pattern; (c) Fringe gradient angle map; (d) Fringe density map.

A biased curvature map is determined by the proposed method as shown in Fig. 5.20(a) and high quality curvature map is obtained after median filtering and B-spline smoothing as shown in Fig 5.20(b). In Fig. 5.20(a), a sharp discontinuity in the biased curvature map is occurred around coordinates (1,250) to (120,250). This is caused by a small corrupted region in the fringe orientation map, which is present in the left side of the map as shown in Fig. 5.19(c). This small corrupted region is formed while converting π-moduli fringe angle map to 2π-moduli fringe orientation map, due to unwrapping error. However, the discontinuity in the curvature is corrected by the

filtering process as shown in Fig. 5.20(b). Similarly, the twist maps, which are obtained before and after filtering and smoothing, are shown in Figs. 5.20(c) and 5.20(d). The slope map determined by the proposed DRPT which utilizes high quality curvature and twist maps is shown in Fig. 5.20(e). The proposed method was implemented using Matlab. It took 1101s of computation time to obtain slope, curvature and twist maps for this fringe pattern. Though the fringe pattern is affected by speckle noise, the proposed method is able to provide high quality slope, curvature and twist maps.

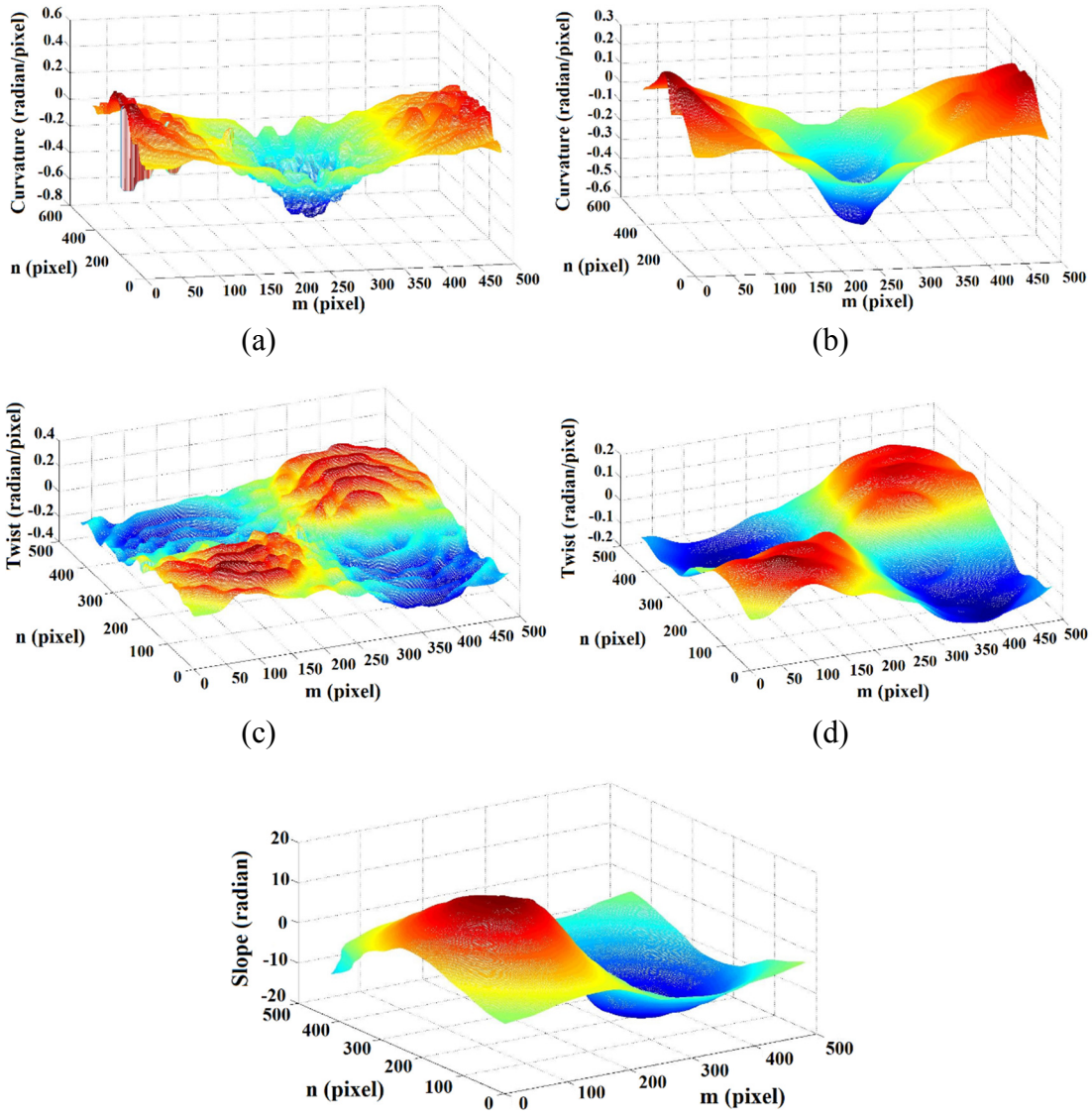

Figure 5.20 (a) Curvature map before filtering; (b) Curvature map after filtering; (c) Twist map before filtering; (d) Twist map after filtering; (e) Slope map.

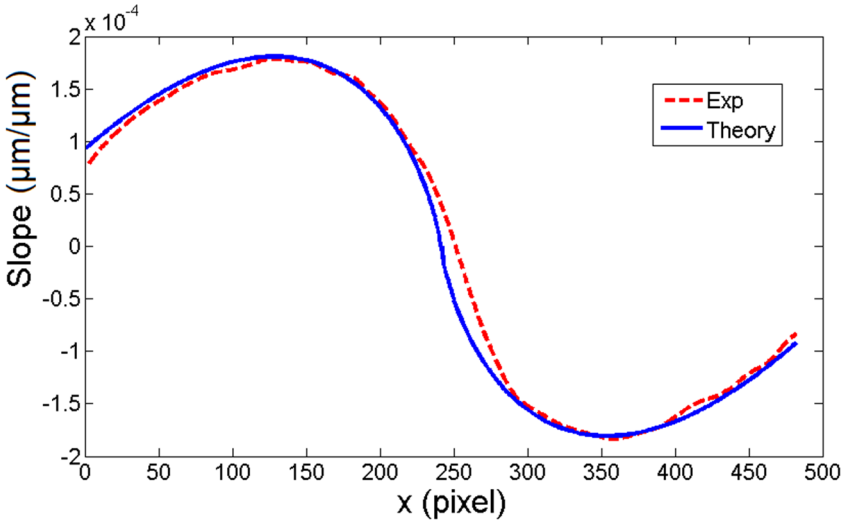

Figure 5.21 Comparison between theoretical & experimental values at central section.

The accuracy of the slope values obtained from the proposed method is validated by comparison with theoretical values. Slope values obtained across the central section of the specimen are plotted in Fig. 5.21. It is shown that the slope values obtained by proposed method is in good agreement with theoretical values for most parts except for a small deviation in the center (deviation up to 0.6e-4). This deviation from the theoretical values is due to high fringe density. Though the DRPT method performs better than the conventional RPT, a sharp change in fringe density has little impact on the accuracy of the proposed DRPT method.

5.3.4 Vibration amplitude measurement using TA-DSPI

5.3.4.1 Accuracy and parameter influence on amplitude determination using TA-DSPI

A simulation study is carried out to determine the accuracy of the proposed method for vibration amplitude measurement. A 256×256 fringe pattern is simulated using Eq. (3.5) with I_0 and V values of 1 and r of 5%. A simulated fringe pattern is shown in Fig. 5.22(a) and the corresponding phase map is shown in Fig. 5.22(b). The phase derivatives in the x and y direction determined from the fringe pattern is shown in Figs. 5.22(c) & 5.22(d). A phase map

determined using the proposed method is shown in Fig. 5.22(e). The discrepancies between simulated phase values and values obtained using the proposed methods are shown in Fig. 5.22(f).

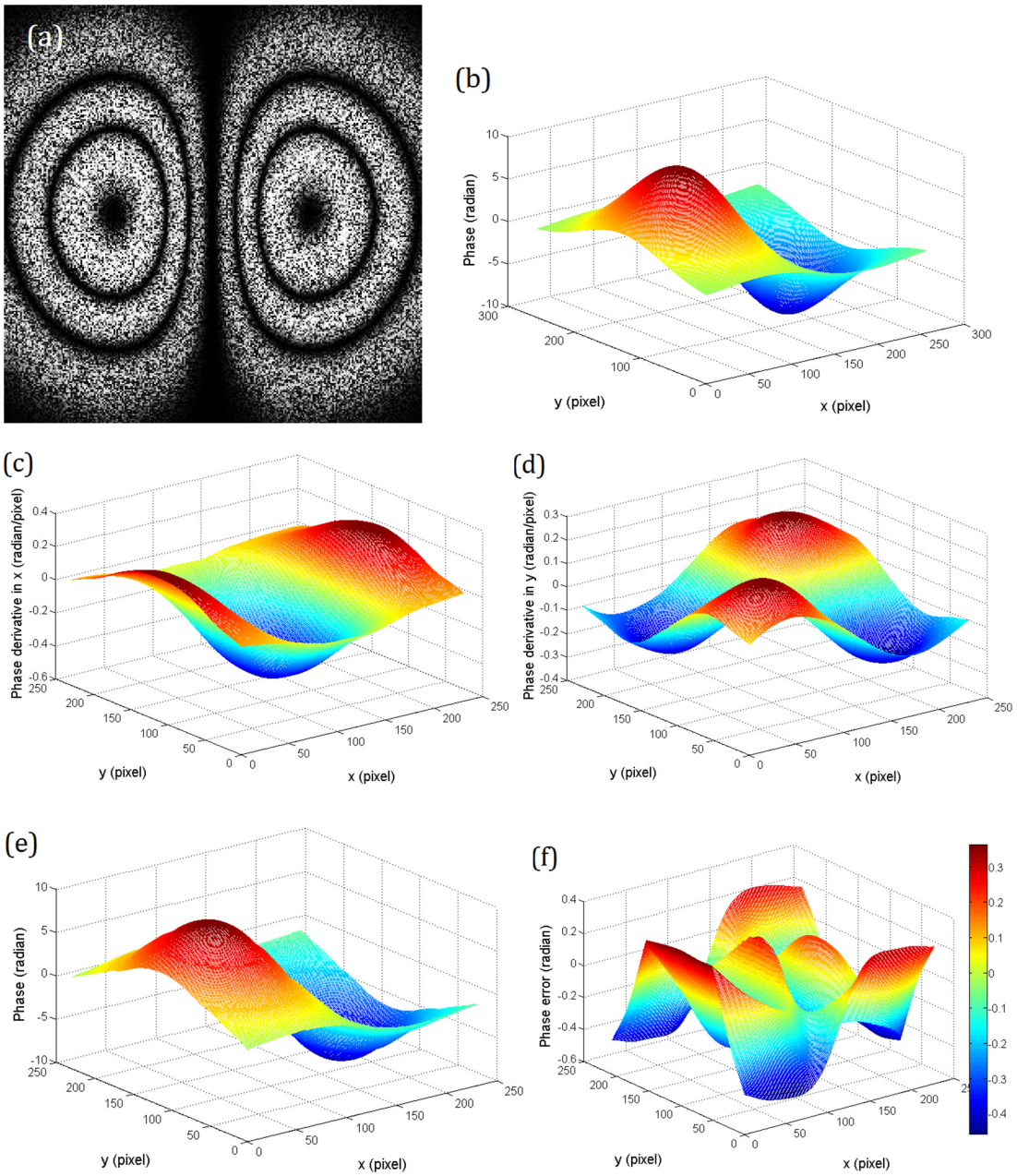

Figure 5.22 (a) A simulated time average fringe pattern; (b) corresponding phase map; (c) phase derivatives in x direction; (d) phase derivatives in y direction; (e) phase map after error correction for Bessel to cosine conversion; (f) phase error map.

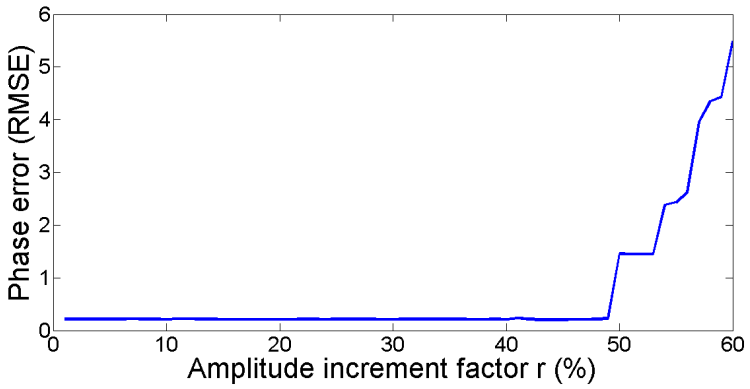

Figure 5.23 Phase error (RMSE) vs amplitude increment factor r.

The proposed method is implemented in Matlab and it took 136 seconds to process 256×256 size image. The root mean square error (RMSE) value calculated for this simulation is 0.2145 radian. However the deviations in the calculated phase are within 0.2 radian except in the regions where the vibration amplitude is maximum and near the boundaries. These larger deviations are due to speckle noise filtering and phase derivative smoothing function but overall the RMSE values for the phase map produced by this method are acceptable.

As mentioned in section 5.1, fringe shapes are noticeably changed for r values 20% and 25% due to a significant change in the fringe locus function $\ddot{\Omega}$. The changes in the fringe shape affect the accuracy of the amplitude. Hence a new simulation study is conducted to investigate the influence of r in amplitude measurement. The proposed amplitude measurement is employed on a series of fringe patterns with r values from 1% to 60%. In Fig. 5.23, phase error values (RMSE) are plotted against r. The plot shows that the error values are less than 0.23 radian for r<50%. Hence choosing an amplitude increment value less than 50% provides high accuracy in amplitude measurement and there is no significant change in fringe contrast for r values below 25%. Hence it is better to choose a r value less than 25%.

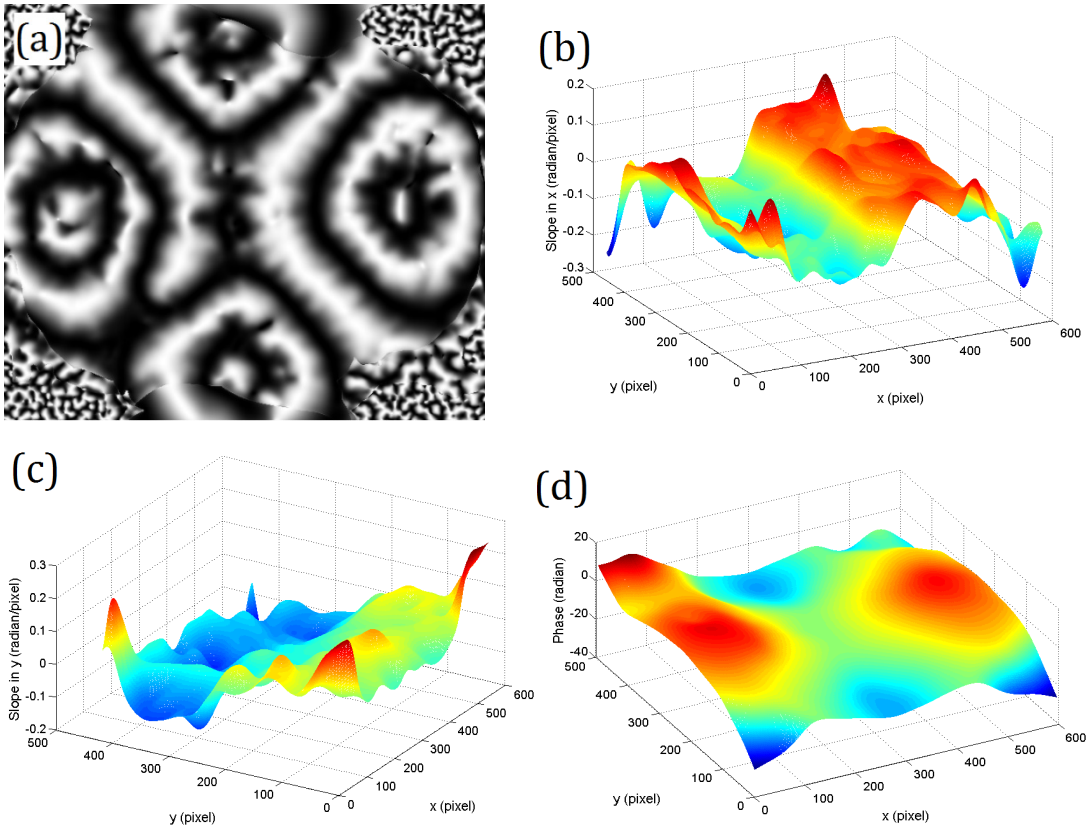

Figure 5.24 (a) Mode 4 experimental fringe pattern after speckle filtering and normalization; (b) phase derivative in *x* direction; (c) phase derivative in *y* direction; (d) phase map after correction.

5.3.4.2 Experimental validation

To validate the proposed amplitude measurement in TA-DSPI using DRPT method, mode 4 experimental fringe pattern (shown in 5.2(i)). Figure 5.24(a), shows the filtered and normalized mode 4 experimental fringe pattern. Phase derivatives obtained in the *x* and *y* directions are shown in Figs. 5.24(b)-5.24(c). A phase map after compensation of the Bessel to cosine function is shown in Fig. 5.24(d). It is seen that the corners of the phase map (Fig. 5.24(d)) have erroneous values which are caused due to the fact that circular vibration patterns are captured on a rectangular sensor. The phase map obtained after correction for Bessel are validated with the fringe counting method which estimates -15.3 radians in the valley and 8.9 radians at the peak. The phase map values, -16 radians in the valley and 8.4 radians at peak, show a good agreement with the fringe counting method. From the results, it is evident that the proposed

method is able to determine full field vibration amplitudes accurately from a single time average complex closed fringe pattern.

5.4 Phase unwrapping using ensemble of hybrid genetic algorithm

5.4.1 Simulation and comparison study of the proposed method

The proposed Ensemble of Hybrid Genetic Algorithm (eHGA) based phase unwrapping method and Hybrid Genetic Algorithm (HGA) based phase unwrapping are implemented in C programming language to calculate the branch cut. A simulation study is carried out for analyzing the robustness and accuracy of the proposed method and the results are compared with Goldstein branch-cut algorithm and HGA algorithm. The first image shown in Fig. 5.25(a) is a wrapped phase signal with SNR 5. Figure 5.25(b) shows the calculated residues. Since the wrapped phase map has less noise, the unwrapped phase maps obtained from all the three methods are very similar to each other as shown in Figs. 5.25(c)-5.25(e). Both HGA and eHGA solutions are obtained at first iterations and no further convergence was necessary.

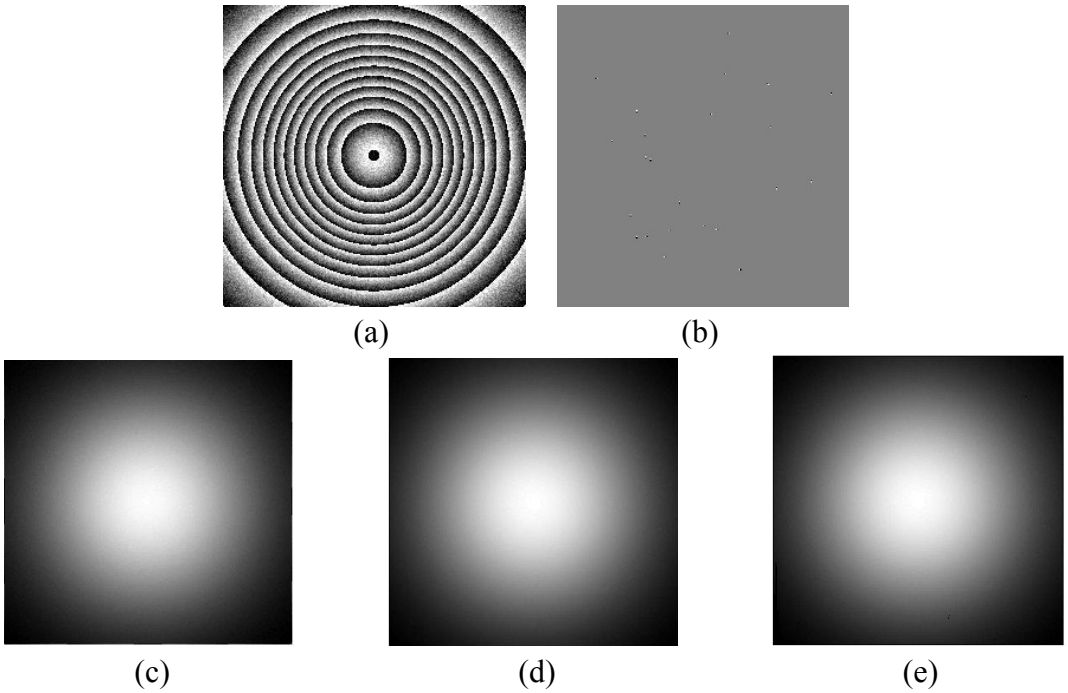

Figure 5.25 (a) Simulated wrapped phase (SNR = 5); (b) Residues calculated; (c) Unwrapped phase map calculated by Goldstein method; (d) HGA; (e) eHGA.

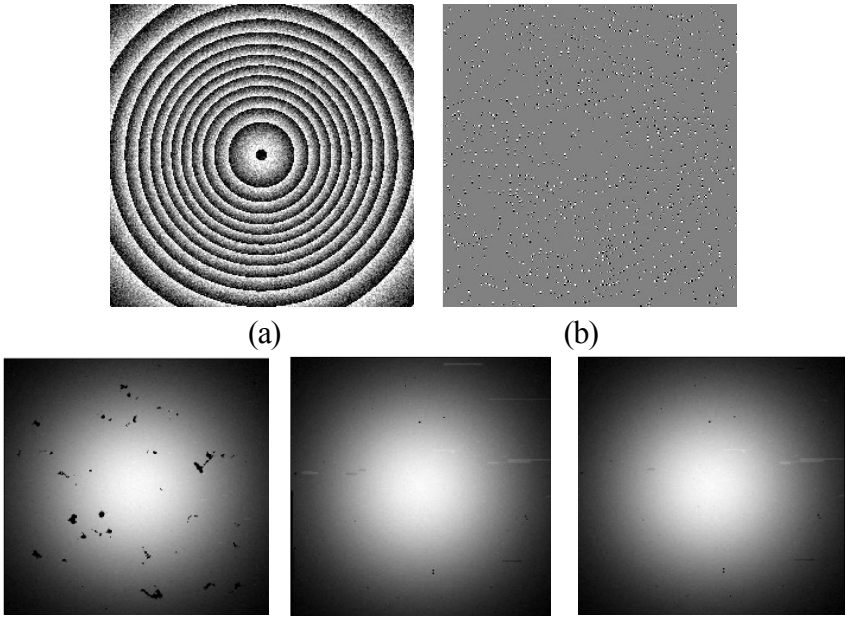

(a) (b)

(c) (d) (e)

Figure 5.26 (a) Simulated wrapped phase (SNR = 1); (b) Residues calculated; (c) Unwrapped phase map calculated by Goldstein method; (d) HGA; (e) eHGA.

A noisy wrapped phase map with SNR 1, which is shown in Fig. 5.26(a), is unwrapped using all three methods. Data from Fig. 5.26(a) produced more residues than the data from Fig. 5.25(a), which can be seen in Figs. 5.25(b) and 5.26(b). An increase in number of residues makes the phase unwrapping process complex. The results are shown in Figs. 5.26(c)-5.26(e), the unwrapped phase map obtained from Goldstein method has more corrupted patches (Fig. 5.26(c)). Both HGA and eHGA outperformed Goldstein method as shown in Figs. 5.26(d)-5.26(e). Figure 5.27 shows 3D-plot of unwrapped phase maps calculated using these three algorithms. Even though the output of the HGA and eHGA are similar, the branch cut length found by eHGA is less than the length found by HGA method.

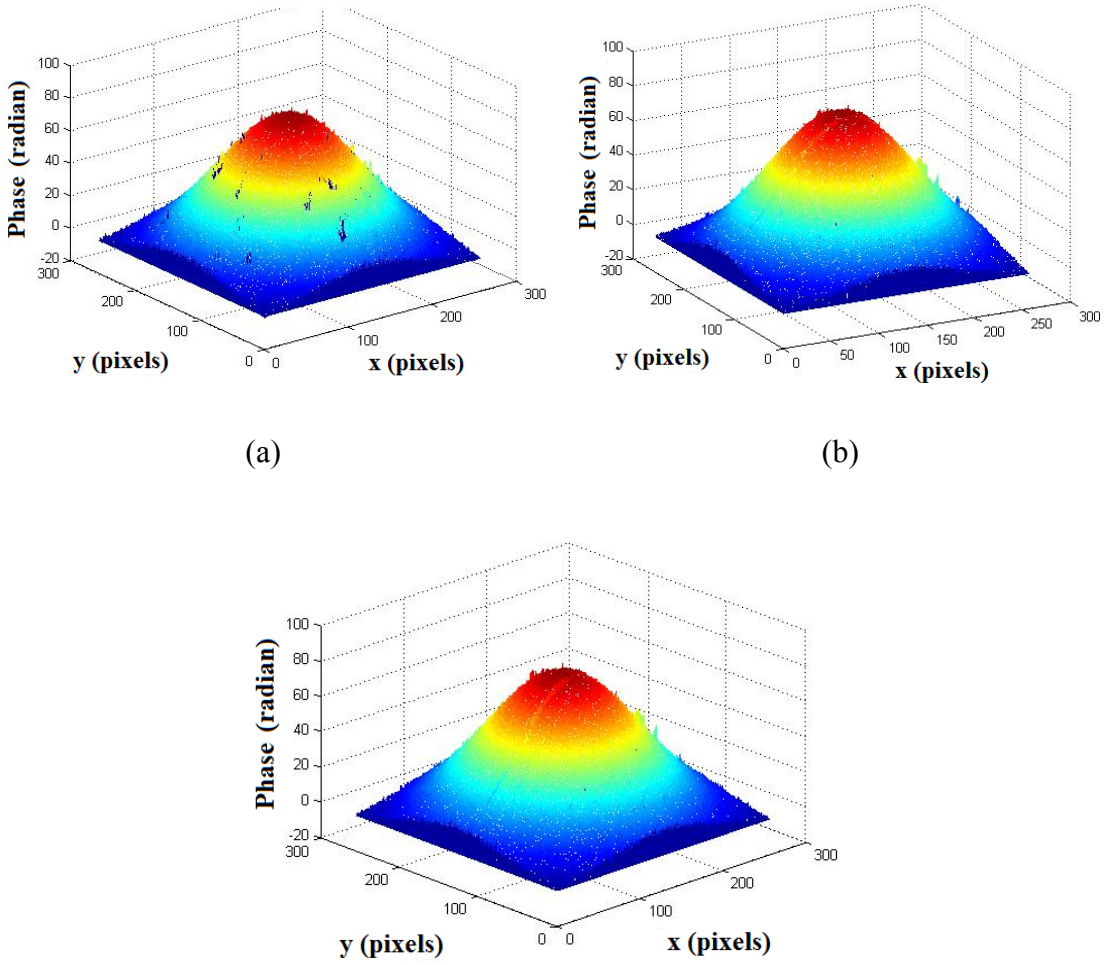

Figure 5.27 (a) Unwrapped phase map calculated by Goldstein algorithm; (b) HGA; (c) eHGA.

To unwrap the phase map shown in Fig 5.26(a), HGA required 47 iterations to obtain the solution. Whereas eHGA required only 22 iterations for producing a similar result and a solution is obtained at the 28th iteration. Table 5.4 illustrates a comparison of three algorithms in terms of computation time, cut length, RMSE and unweighted L0 measure. As artificial intelligence (AI) techniques would not produce the same result on every run, it is not valid to compare the convergence effectiveness of HGA and eHGA in one run. Hence both HGA and eHGA are executed on the same problem for 10,000 times and the convergence results are shown in Fig. 5.28. The results show the mean fitness value or branch cut length (for 10,000 runs) at every generation (iteration)

for the first 300 generations. Even though the eHGA started with the same initial fitness value, it converged more efficiently than HGA. The mean branch cut length of eHGA at every generation is better than the mean branch cut length of HGA. Though eHGA requires more computation time to execute a generation than HGA, it compensates for the extra computation time by converging faster. Hence the overall solution obtained from the eHGA took less time than the HGA. From the results, it is evident that eHGA performs better than HGA for phase unwrapping a noisy fringe pattern.

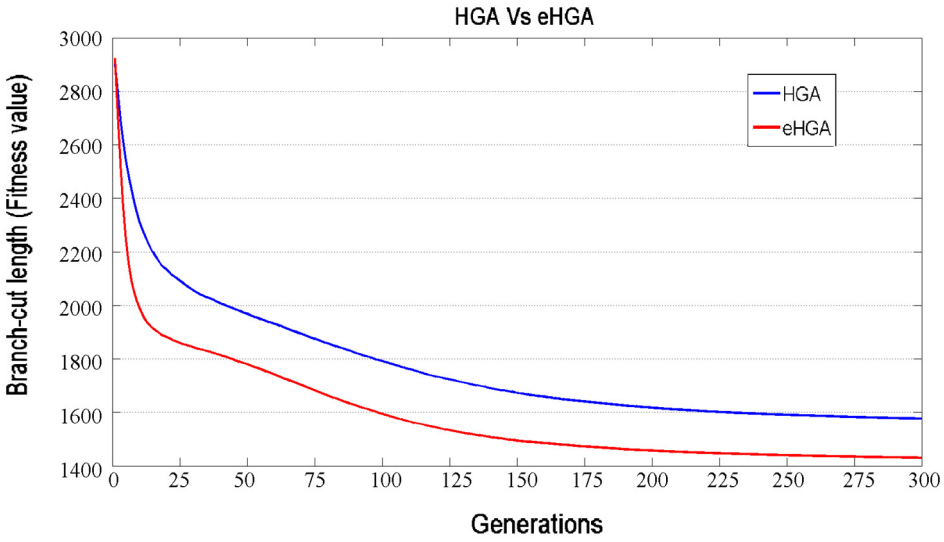

Figure 5.28 Performance comparison between HGA and eHGA.

Table 5.4 Comparison of results from different branch-cut methods.

Algorithm	**Time taken (s)**	**Total Cut Length**	**RMSE**	**Unweighted L^0 measure**
Goldstein	1	5019.0	0.0150027	0.1352
HGA	5	1204.38	0.0040324	0.1056
eHGA	3	987.54	0.0038924	0.1063

Though the proposed branch cut minimization based phase unwrapping method is effective for noisy phase maps, it is not suitable for phase maps with discontinuities (Karout,

2007). Residues caused due to discontinuities are different from the residues from noise, so the same approach will not be effective. A simulation study is carried out to verify the effectiveness of the proposed method for phase maps with discontinuities. Figure 5.29(a) is a simulated wrapped phase map and the unwrapped phase maps obtained using the proposed method is shown in Fig. 5.29(b). From the results, it is evident that this method is not effective for unwrapping phase map with discontinuities.

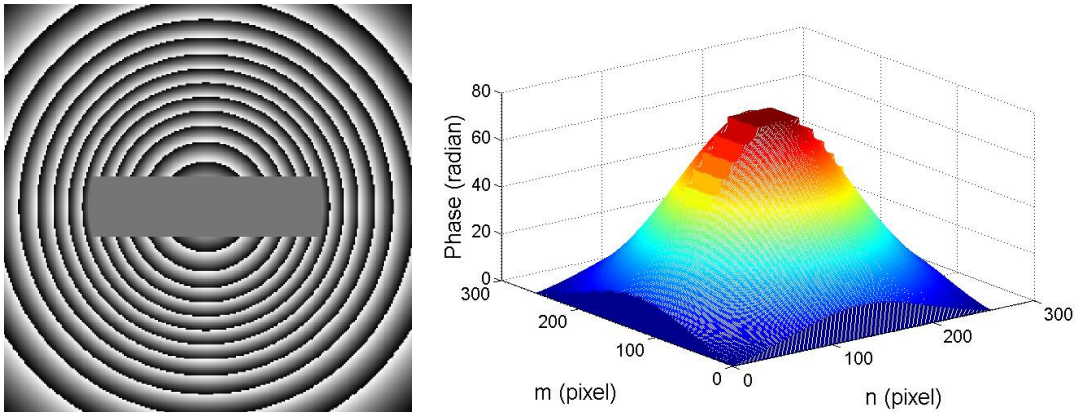

(a) (b)

Figure 5.29 (a) Wrapped phase map with discontinuity; (b) 3D plot of unwrapped phase map calculated by eHGA;

5.4.2 Experimental validation

An experimental validation to analyze the performance of the proposed method in a noisy wrapped phase map is carried out. A wrapped phase map obtained from DHI is shown in Fig. 5.30(a). Phase unwrapping is carried out using HGA and eHGA and the results are shown in Figs. 5.30(b)-5.30(c) and 3D plots of an unwrapped phase map is shown in Figs. 5.30(d)-5.30(e).

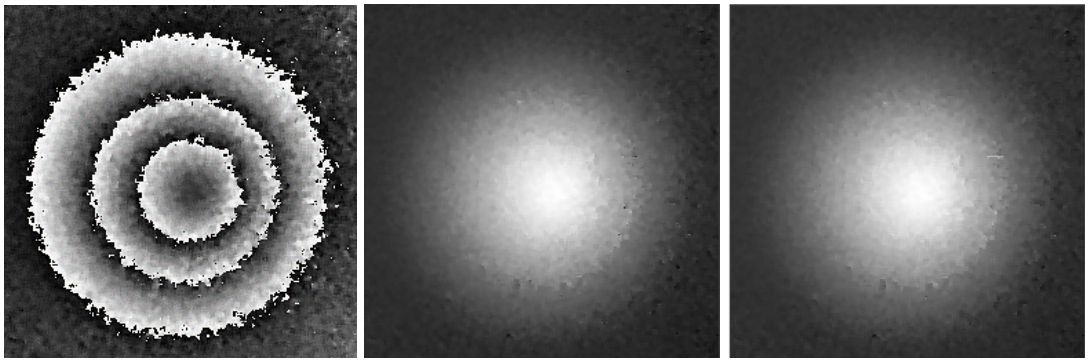

(a) (b) (c)

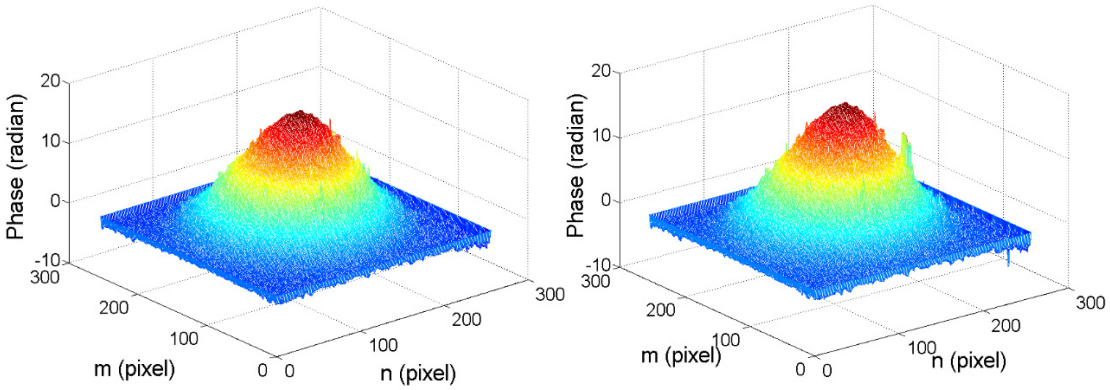

(d) (e)

Figure 5.30 (a) Wrapped phase map from DHI; (b) Unwrapped phase map calculated by eHGA; (c) HGA; (d) 3D plot of phase map calculated by eHGA; (e) HGA.

The results show that both HGA and eHGA are able to unwrap an experimental fringe pattern effectively. Thus, this method is able to overcome phase unwrapping of a noisy phase map, however the method is not suitable for a phase map with discontinuities. Hence the method is more suitable for displacement and strain map unwrapping and not suitable for profilometry application.

5.5 Material characterization of a small cantilever beam

A magnesium nano-composite cantilever beam is loaded at the free end and a DSPI fringe pattern is captured. A load of 0.275 N is applied on the cantilever beam and the corresponding fringe pattern is shown in Fig. 5.31(a). The phase map of complex signal using the Fourier transform method is shown in Fig. 5.31(b). The deformation plot of the cantilever beam obtained from unwrapping the phase map is shown in Fig. 5.31(c). As the displacement is influenced by rigid body motion, the elastic modulus calculated from the values of the displacement obtained would contain large errors. Hence the slope map of the displacement is obtained using the DHODA method and the slope values are shown in Fig. 5.31(d).

The elastic modulus of the cantilever beam is calculated using a tensile testing for validating the proposed method. Figure 5.32 shows the stress-strain curve obtained from the tensile test (only elastic deformation) and the elastic modulus is 38.6±1.2 GPa. The elastic modulus obtained using the proposed method (Eq. (3.48)) is 37.78±0.77 GPa which is more accurate than the elastic modulus (35.8±3.19 GPa) obtained from the deformation map without considering the influence of the rigid body movement (Eq. (3.47)). Due to the influence of small rigid body movement i.e. 0.5' rotation about the y axis, the elastic modulus shows a discrepancy of 6.1%. In comparison with the elastic modulus value obtained from the tensile test, the proposed method only shows a discrepancy of 2.1% but the same is 7.8% if the influence of the rigid body movement is not considered (Eq. (3.47)). Hence it is necessary to consider the influence of rigid body movement while measuring the material properties using DSPI and the proposed method is able to overcome this problem.

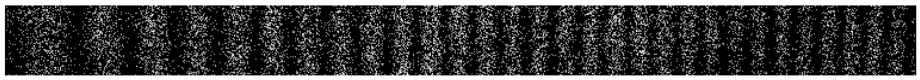

Fixed end Free end

(a)

Fixed end Free end

(b)

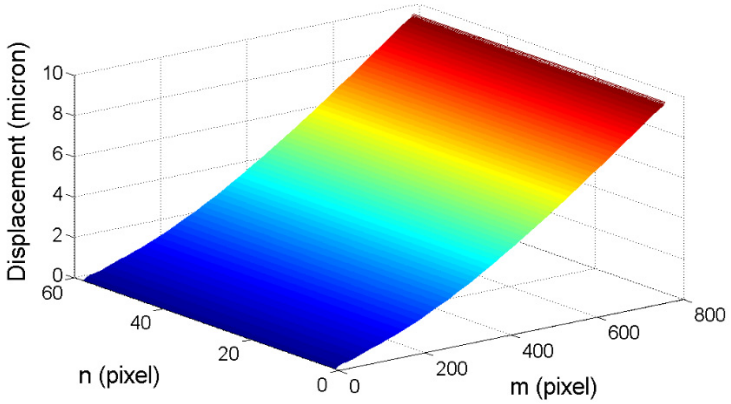

(c)

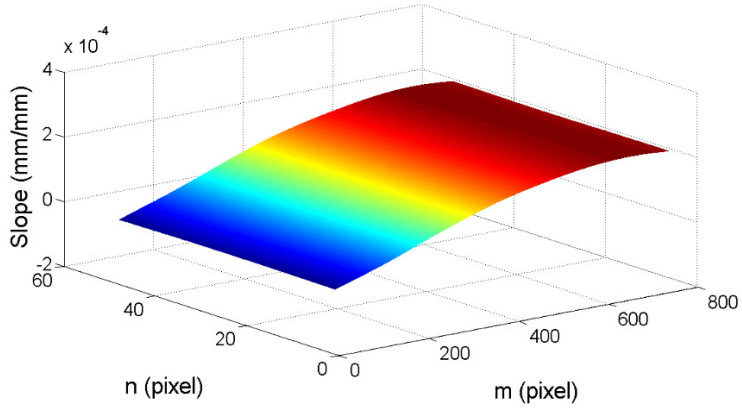

(d)

Figure 5.31 (a) DSPI fringe pattern of a cantilever beam; (b) Phase map obtained from Fourier method; (c) Displacement map of the cantilever beam; (d) Slope map.

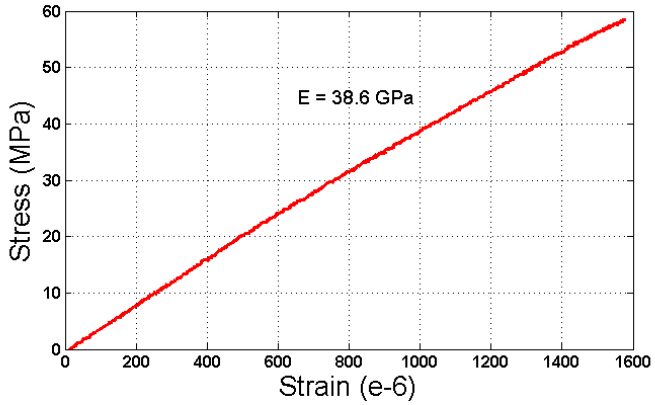

Figure 5.32 Stress-Strain curve from tensile test.

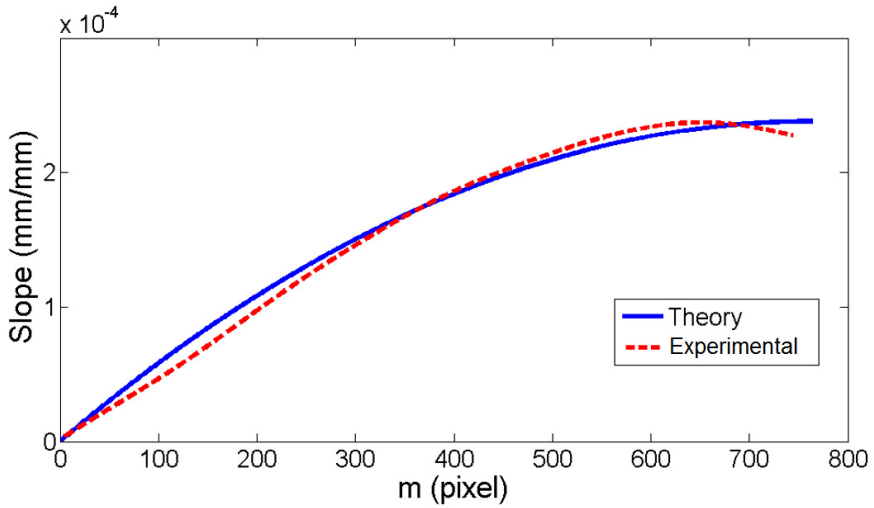

(a)

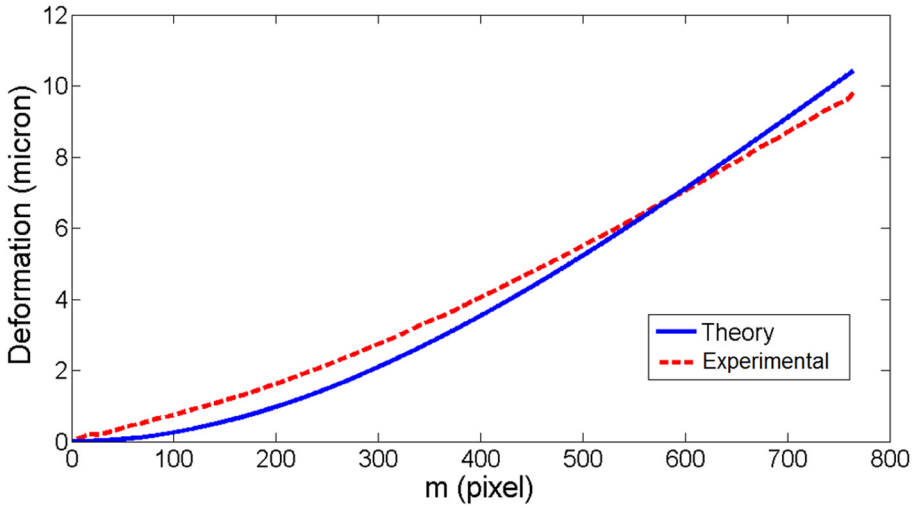

(b)

Figure 5.33 (a) Comparison of experimental and theoretical slope value (in the middle row); (b) same comparison of deformation value (in the middle row).

Figure 5.33(a) shows a comparison between the theoretical slope values caused and slope values obtained from experimental results (from the middle section of the image). Similarly Fig. 5.33(b) shows the theoretical deformation and the measured deformation. It is seen that the discrepancy between the theoretical slope values and experimental is less than the corresponding deformation values. The reason, as mentioned earlier, is due to the rigid body displacement.

CHAPTER SIX

CONCLUSIONS AND FUTURE WORK

6.1 Conclusions

The main goals of this thesis are to develop novel phase and phase derivative determination algorithms in coherent optical techniques, and to overcome the existing problems. The main conclusions drawn from the research work in this thesis are summarized as follows:

1. A novel phase derivative estimation method based on Teager operator to estimate the instantaneous frequencies from a complex amplitude is proposed. This method uses discrete higher order image demodulation for calculating biased phase derivatives. The biased phase derivatives are processed using B-spline smoothing to obtain high quality phase derivatives. The main advantages of the proposed method are a) unwrapped phase derivatives in both the x and y directions are obtained directly from a complex signal; b) less computational time; c) it is more accurate than existing Teager operator based phase derivative algorithms.

   A sequential algorithm called Teager-Hilbert-Huang transform is also proposed to determine phase derivatives from a single fringe pattern. Comprehensive analyses to study the influence of various parameters on the accuracy of the proposed algorithm are carried out. The results show that the method provides accurate phase derivatives even from fringe patterns affected by speckle noise.

Experimental validations for the proposed method is carried out using both DHI (complex signal) and DSPI (fringe pattern).

2. A novel method to calculate phase derivatives from fringe orientation and density is proposed. A derivative based simplified phase tracker algorithm is also proposed for phase demodulation. The novelty and main advantages of the proposed methods are a) this method determines the phase derivatives from fringe patterns directly without determining a phase map; b) determined phase derivatives are utilized for phase demodulation process; c) the proposed DRPT requires less computation time than the conventional RPT method; d) it also provides better accuracy and able to overcome the limitations of the RPT method. The experimental validation for the proposed method is carried out using both DSPI and DSSI.

3. A novel experimental modal analysis technique for mode shape visualization and vibrational amplitude measurement using TA-DSPI is proposed. An amplitude varied reference frame technique is also proposed to improve fringe contrast in time average methods and a mathematical model is further developed to determine the vibration amplitude from a single TA-DSPI fringe pattern using DRPT method. The novelty and main advantages of the proposed method are a) the method does not require a phase shifter either for fringe contrast improvement or amplitude measurement; b) this method requires only one fringe pattern for amplitude measurement and numerical analysis and experiments are carried out to validate the proposed method. Numerical analysis results show that the proposed method provides better fringe contrast in recorded fringe patterns and good accuracy. A FEM modal analysis is carried

out to validate the experiment results for mode shape visualization. Resonant frequencies and mode shapes obtained from FEM simulations are in good agreement with experiment. The proposed vibration amplitude determination method is validated with experimental TA-DSPI and the results show that the proposed method is able to demodulate complex and highly noisy fringe patterns.

4. A novel eHGA algorithm for 2D phase unwrapping is proposed. Among the AI methods used for branch-cut phase unwrapping hybrid genetic algorithm is found to be more robust and fast. Numerical analysis is carried out to compare the HGA and the proposed method. The proposed method consistently able to converge faster than the HGA method and also provides better results. Unwrapped phase map obtained from DHI is used for experimental validation. The results also confirms that the proposed method performs better than the HGA method.
5. A novel method to eliminate the influence of rigid body movement on Young's modulus determination is developed. A mathematical model for rigid body movement in out of plane displacement measurement is analyzed and it is found that the impact of a rigid body movement can be removed in slope map easily than in displacement map. The proposed technique uses Fourier transform and DHODA method to calculate the slope map from a DSPI fringe pattern from which the elastic modulus of the cantilever beam is determined. The results obtained using the proposed method is in good agreement with that determined using a resonance frequency damping analyzer.

6.2 Future work

The research work in this thesis has contributed significantly to improve phase retrieval techniques in displacement and displacement derivative measurements, and has also overcome some existing problems. Moreover, this research work also open up new research areas in optical measurement methods. In this thesis, the proposed techniques are described and validated with simulation and experimental results.

Though the proposed methods have overcome most of the existing challenges in optical displacement and displacement derivatives measurement, there are few limitations still exist. The Teager based phase derivatives determination methods have a limitation that the instantaneous frequency of the signal should not be greater than carrier frequency. Hence high frequency changes cannot be determined accurately. Derivative based regularized phase tracker method has reduced the computation time in RPT process, however large fringe pattern of size more than 1024x1024 pixels would take hours of computation time. Apart from these specific limitations, in all window based techniques proposed, the window size should be chosen manually. As mentioned earlier, eHGA phase unwrapping method are very effective for noisy phase maps but they cannot unwrap a phase map with discontinuities. In elastic modulus measurement of a cantilever beam, the rigid body movement can be corrected only when a known zero slope boundary condition point is available within the area of measurement. In general, phase retrieval techniques provide full-field displacement and displacement derivatives only when the boundary conditions are known. In practice, if the boundary conditions are unknown, force transducers or strain gauges could be attached to obtain boundary conditions, along with the optical techniques to measure full-field displacements.

Research is a continuous process and there is no stop point. Hence it is impossible to say that this thesis has covered all possible aspects in this topic. It is recommended that some future work can be done to develop new techniques or improve the adaptability of the proposed techniques. The following issues can be further addressed.

1. The frequency limitation in Teager based phase derivatives method is overcome by zero-padding frequency interpolation in DHI. However, no work has been done on a speckle fringe pattern. A Speckle fringe patterns resolutions are restricted by speckle noise and SNR value is also too low in a single fringe pattern analysis technique. All these factors prevent the speckle fringe pattern technique from achieving a higher resolution measurement. Further research can be carried out to improve the SNR value in a single speckle fringe pattern so that high frequency changes can be determined using Teager based methods.
2. Derivative based regularized phase tracker method overcome most of the limitations of conventional RPT method. The influence of fringe density variation in accuracy is reduced in DRPT than in RPT technique. However high fringe density change would affect the accuracy of phase demodulation in a local region and DPRT method requires normalized fringe pattern for phase demodulation. Techniques such as generalized regularized phase tracker and improved generalized regularized phase tracker techniques are available to overcome the limitations. However, these methods require large computational time. Hence further research can be carried out to overcome the limitations without increasing the computational time.
3. The proposed quantitative vibration analysis technique is utilized for mode shape visualization in this thesis. Further applications which utilizes the vibration amplitude data to determine material and structural properties

(dynamic elastic modulus, damping coefficient, frequency response functions, etc.) can be investigated. Similarly, this technique can be developed for non-destructive testing to detect defects which are difficult to detect with conventional methods.

4. The proposed eHGA utilized various parameters used in HGA for improving the convergence speed. Similarly, the ensemble of different operators for various operations such as initialization, selection, crossover & mutation, is expected to improve the results. Hence possibilities of such improvements on this algorithm can be investigated. The proposed algorithm is very effective for noisy images but it will not guarantee results if there are any real discontinuities present in the phase map. Hence further investigations can be carried out to develop hybrid algorithms for phase unwrapping problems which utilize the advantages of both AI and classical techniques.
5. The influence of rigid body movement in in-plane displacement measurement can be studied and methods to reduce this influence can be developed. Applications which are susceptible to rigid body movement such as residual stress measurement, can be investigated for utilizing the proposed method. Further, methods to prevent the influences of rigid body movement in deformation measurement can be investigated.

REFERENCES

1. Asundi, A. K., Matlab for photomechanics: a primer, Boston, Elsevier, 2002.

2. Asundi, A. and J. Wang, Strain contouring using Gabor filters: principle and algorithm, Opt. Eng. 41, pp.1400-1405, 2002.

3. Bhaduri, B., M. P. Kothiyal, and N. Krishna Mohan, Vibration mode shape visualization with dual function DSPI system, Proc. SPIE 6292, pp. 629217, 2006.

4. Bhaduri, B., C. J. Tay and C. Quan, Direct measurement of curvature and twist using two-channel double-aperture digital shearography, Opt. Eng. 49, pp. 033604-033604-6, 2010.

5. Bone, D. J., H. A. Bachor, R. J. Sandeman, Fringe-pattern analysis using a 2-D Fourier transform, Appl. Opt. 25, pp.1653-1660, 1986.

6. Boudraa, A. O., J. C. Cexust, F. Salzenstein, and L. Guillon, IF estimation using Empirical Mode Decomposition and nonlinear Teager energy operator, IEEE conf. pub., pp. 45-48, 2004.

7. Boudraa, A. O., F. Salzenstein, and J. Cexus, Two-dimensional continuous higher-order energy operators, Opt. Eng. 44, pp. 7001–7010, 2005.

8. Buckland, J. R., J. M. Huntley, and S. R. E. Turner, Unwrapping noisy phase maps by use of a minimum-cost-matching algorithm, Appl. Opt. 34, pp.5100-5108, 1995.

9. Butters, J. N. and J. A. Leendertz, Speckle pattern and holographic techniques in engineering metrology, Opt. Laser Technol., 3, pp. 26-30. 1971.

10. Butters, J. N., R. C. Jones, and C. Wykes, Electronic speckle pattern interferometry. In Speckle Metrology,Ed. R. K. Erf), New York, Academic Press, pp. 111-158. 1978.

11. Carré, P., Installation et utilization du compateur photoelectrique et interferential du Bureau International des Poids et Mesures, Metrologia, 2, pp. 13-20 1966.

12. Chau, F. S. and J. Zhou, Direct measurement of curvature and twist of plates using digital shearography, Opt. Lasers Eng. 39, pp.431-440, 2003.

13. Chen, H., R. Su, A. Kwan, and A. Fok, Correction of strain errors induced by small rigid-body motions in electronic speckle pattern interferometry measurement, HKIE Trans. 20, pp. 2-11, 2013.

14. Chen, L., C. Quan, C. J. Tay, and Y. Fu, Shape measurement using one frame projected sawtooth fringe pattern, Opt. Commun. 246, pp.275-284, 2005.

15. Chen, L., Development of optical phase evaluation techniques: application to fringe projection and digital speckle measurement, National University of Singapore, Ph. D. thesis, 2005.

16. Chen, L., Cross-platform Image-processing Program – UU and Fig for optical metrology applications, Proc. SPIE 8769, pp. 87690U1- 87690U4, 2013.

17. Chen, W., C. Quan, and C. J. Tay, Retrieval of instantaneous frequency from digital holograms based on adaptive windows, Opt. Eng. 47, pp. 065801(1)-065801(6), 2008.

18. Chen, W., C. Quan, and C. J. Tay, Measurement of curvature and twist of a deformed object using digital holography, Appl. Opt. 47, pp.2874–2881, 2008.

19. Chen, W., C. Quan, C. J. Tay, and Y. Fu, Quantitative detection and compensation of phase-shifting error in two-step phase-shifting digital holography, Opt. Commun. 282, pp.2800-2805, 2009.

20. Chen, W., C. Quan, and C. J. Tay, Extended depth of focus in a particle field measurement using a single-shot digital hologram, Appl. Phy. Lett. 95, pp.201103(1)- 201103(3), 2009.

21. Chen, W., Development of spatial and temporal phase evaluation techniques in digital holography, National University of Singapore, Ph. D. thesis, 2010.

22. Cornu, C., S. Stanković, C. Ioana, A. Quinquis, and L. Stanković, Generalized Representation of Phase Derivatives for Regular Signals, IEEE Trans. on Sig. Procss. 55 , pp. 4831, 2007.

23. Creath, K., Phase-shifting speckle interferometry, Appl. Opt. 24, pp.3053-3058, 1985.

24. Cuche, E., F. Bevilacqua, and C. Depeursinge, Digital holography for quantitative phase-contrast imaging, Opt. Lett. 24, pp.291-293, 1999.

25. Davies, J. C., C. H. Buckberry, J. D. C. Jones, and C. C. Panell, Development and application of a fibre-optic electronic speckle pattern interferometer (ESPI), Proc. SPIE 863, pp. 194-207, 1987.

26. Debnath, S. K., M. P. Kothiyal, and S. W. Kim, Evaluation of spectral phase in spectrally resolved white-light interferometry: comparative study of single-frame techniques, Opt. Lasers Eng. 47, pp.1125-1130, 2009.

27. Diop, E. H. S., A. O. Boudraa, and F. Salzenstein, A joint 2D AM-FM estimation based on higher order Teager-Kaiser energy operators, Sign. Img. Vid. Procs. 5, pp. 61-68, 2009.

28. Dorrio, B. V. and J. L. Fernandez, Phase-evaluation methods in whole-field optical measurement techniques, Meas. Sci. Technol. 10, pp.R33-R55, 1999.

29. Durak, L. and O. Arikan, Short-time Fourier transform: two fundamental properties and an optimal implementation, IEEE Trans. Signal Process. 51**,** pp.1231-1242. 2003.

30. Estrada, J. C., M. Servin, J. A. Quiroga, J. L. Marroquin, Path independent demodulation method for single image interferograms with closed fringes within function space C(2), Opt. Exp. 14, pp. 9687-9698, 2006.

31. Falldorf, C., R. Klattenhoff, and A. Gesierich, Lateral shearing interferometer based on a spatial light modulator in the Fourier plane, in Fringe 2009: 6th International Workshop on Advanced Optical Metrology (Ed. W. Osten, and M. Kujawinska), Springer, Heidelberg, pp. 93–98, 2009.

32. Farias, M., R. Rodriguez-Vera, and J. A. Raya, Young's modulus determination of a circular plate by ESPI, Proc. SPIE 7499, pp. 719912-1 719912-6, 2009.

33. Federico, A. and G. H. Kaufmann, Phase retrieval in electronic speckle pattern interferometry using the continuous wavelet transform, Proc. SPIE 4419, pp.162-165, 2001.

34. Federico, A. and G. H. Kaufmann, Comparative study of wavelet thresholding methods for denoising electronic speckle pattern interferometry fringes, Opt. Eng. 40, pp.2598-2604, 2001.

35. Federico, A. and G. H. Kaufmann, Evaluation of the continuous wavelet transform method for the phase measurement of electronic speckle pattern interferometry fringes, Opt. Eng. 41, pp.3209-3216, 2002.

36. Federico, A. and G. H. Kaufmann, Evaluation of the continuous wavelet transform method for phase measurement in digital speckle pattern interferometry, Proc. SPIE 4777, pp.279-287, 2002.

37. Federico, A. and G. H. Kaufmann, Phase retrieval in digital speckle pattern interferometry by use of a smoothed space-frequency distribution, Appl. Opt. 42, pp. 7066–7071, 2003.

38. Fienup, J. R., Phase retrieval algorithms: a comparison, Appl. Opt. 21, pp.2758-2769, 1982.

39. Fu, Y., C. J. Tay, C. Quan, and L. J. Chen, Temporal wavelet analysis for deformation and velocity measurement in speckle interferometry, Opt. Eng. 43, pp.2780-2787, 2004.

40. Fu, Y., Development of temporal phase analysis techniques in optical measurement, National University of Singapore, Ph. D. thesis, 2005.

41. Fu, Y., G. Pedrini, and W. Osten, Vibration measurement by temporal Fourier analyses of a digital hologram sequence, Appl. Opt. 46, pp.5719-5727, 2007.

42. Fu, Y., R. M. Groves, G. Pedrini, and W. Osten, Kinematic and deformation parameter measurement by spatiotemporal analysis of an interferogram sequence, Appl. Opt. 46, pp.8645-8655, 2007.

43. Gabor, D., A new microscopic principle, Nature (London) 161, pp.777-778, 1948.

44. Ganesan, A. R., D. K. Sharma, and M. P. Kothiyal, Universal digital speckle shearing interferometer, Appl. Opt., 27, pp. 4731-4734. 1988.

45. Ghiglia, D. C. and M. D. Pritt, Two dimensional phase unwrapping: theory, algorithm, and software, New York, Wiley, 1998.

46. Goldstein, R. M., H. A. Zebker, and L. Werner, Satellite Radar Interferometry: Two-Dimensional Phase Unwrapping, Radio Sci. 23, pp. 713-720, 1988.

47. Goodman, J. W. and R. W. Lawrence, Digital image formation from electronically detected holograms, Appl. Phys. Lett. 11, pp.77-79, 1967.

48. Goodman, J. W., Introduction to Fourier Optics, 2nd ed., New York, McGraw-Hill, 1996.

49. Gorthi, S. S., and P. Rastogi, Piecewise polynomial phase approximation approach for the analysis of reconstructed interference fields in digital holographic interferometry, Journal of Opt.: Pure and Appl. Opt. 11, pp. 1-6, 2009.

50. Gorthi, S. S., and P. Rastogi, Simultaneous measurement of displacement, strain and curvature in digital holographic interferometry using high-order instantaneous moments, Opt. Exp. 17, pp. 17784-17791, 2009.

51. Grilli, S., P. Ferraro, S. D. Nicola, A. Finizio, G. Pierattini, and R. Meucci, Whole optical wavefields reconstruction by digital holography, Opt. Express 9, pp.294-302, 2001.

52. Gutmann, B., and H. Weber, Phase unwrapping with the branch-cut method: clustering of discontinuity sources and reverse simulated annealing, Appl. Opt. 38, pp. 5577–5793, 1999.

53. Gutmann, B., and H. Weber, Phase unwrapping with the branch-cut method: role of phase-field direction, Appl. Opt. 39, pp. 4802–4816, 2000.

54. He, W., Y. Cheng, L. Xia, and F. Liu., A new particle swarm optimization-based method for phase unwrapping of MRI data, Comp. Math. Mthd. Med., pp. 2012, 2012.

55. Huang, L., Q. Kemao, B. Pan, and A. K. Asundi, Comparison of Fourier transform, windowed Fourier transform, and wavelet transform methods for phase extraction from a single fringe pattern in fringe projection profilometry, Opt. Lasers Eng. 48, pp. 141-148, 2010.

56. Huang, M. J., and P. Sung, Regional phase unwrapping algorithm for photo elastic phase map, Opt. Exp. 18, pp. 1419-1429, 2010.

57. Huang, N. E., Z. Shen, S. R. Long, M. C. Wu, H. H. Shih, Q. Zheng, N. C. Yen, C. C. Tung, and H. H. Liu, The empirical mode decomposition and the Hilbert spectrum for nonlinear and non-stationary time series analysis, Proc. Roy. Soc. Lon. A 454, pp. 903 – 995, 1998.

58. Hung, Y. Y. and C. Y. Liang, Image-shearing camera for direct measurement of surface strains, Appl. Opt. 18, pp.1046-1051, 1979.

59. Hung, Y. Y., Shearography: A new optical method for strain measurement and non-destructive testing, Opt. Eng. 21, pp. 391–395, 1982.

60. Hung, Y. Y., Shearography: a novel and practical approach to non-destructive testing, J. Non-destructive Eval. 8, pp. 55-68, 1989.

61. Hung, Y. Y., Digital shearography versus TV-holography for non-destructive evaluation, Opt. Lasers Eng. 26, pp.421-436, 1997.

62. Hung, Y. Y., and H. P. Ho, Shearography: an optical measurement technique and applications, Mater. Sci. Eng. R 49, pp. 61–87, 2005.

63. Huntley, J. M. and H. O. Saldner, Temporal phase-unwrapping algorithm for automated interferogram analysis, Appl. Opt. 32, pp.3047-3052, 1993.

64. Huntley, J. M. and H. O. Saldner, Shape measurement temporal phase unwrapping: comparison of unwrapping algorithms, Meas. Sci. Technol. 8, pp.986-992, 1997.

65. Huntley, J. M., G. H. Kaufmann, and D. Kerr, Phase-shifted dynamic speckle pattern interferometry at 1 kHz, Appl. Opt. 38, pp.6556-6563, 1999.

66. Huntley, J. M., Automated analysis of speckle interferograms, (Ed. P. Rastogi), Digital speckle pattern interferometry and related techniques, New York, Wiley, 2001.

67. Judge, T. R. and P. J. Bryanston-Cross, A review of phase unwrapping techniques in fringe analysis, Opt. Lasers Eng. 21, pp.199-239, 1994.

68. Kai, L., and Q. Kemao, A generalized regularized phase tracker for demodulation of a single fringe pattern, Opt. Exp. 20, pp. 12579–12592, 2012.

69. Kai, L., and Q. Kemao, Improved generalized regularized phase tracker for demodulation of a single fringe pattern, Opt. Exp. 21, pp. 24385 – 24397, 2013.

70. Karout, S. A., M. A. Gdeisat, D. R. Burton, and M. J. Lalor., Two-dimensional phase unwrapping using a hybrid genetic algorithm, Appl. Opt., 46, pp. 730-743, 2007.

71. Kim, M. K., L. Yu, and C. J. Mann, Interference techniques in digital holography, J. Opt. A: Pure Appl. Opt. 8, pp.S518-S523, 2006.

72. Kim, K. S., H. Chang, S. W. Jung, T. H. Choi, W. J. Kim, J. G. Song, and A. Naseem, Determination of elastic modulus of thin materials by speckle interferometry, 17th World Conf. NDT, China, 2008.

73. Kreis, T., Digital holographic interference-phase measurement using the Fourier-transform method, J. Opt. Soc. Am. A 3, pp.847-855, 1986.

74. Kreis, T., M. Adams, and W. P. O. Jüptner, Methods of digital holography: a comparison, Proc. SPIE 3098, pp.224-233, 1997.

75. Kreis, T., Handbook of holographic interferometry: optical and digital methods, Weinheim, Wiley-VCH, 2005.

76. Kronrod, M. A., N. S. Merzlyakov, and L. P. Yaroslavski, Reconstruction of holograms with a computer, Sov. Phys. Technol. Phys. 17, pp.333-334, 1972.

77. Kulkarni, R., and P. Rastogi, Estimation of phase derivatives using discrete energy separation algorithm in digital holographic interferometry, Opt. Lett. 39, pp. 3722-3724, 2014.

78. Kulkarni, R., and P. Rastogi, Phase derivative estimation from a single interferogram using a Kalman smoothing algorithm, Opt. Lett. 40, pp. 3794-3797, 2015.

79. Kumar, U. P., N. Krishna Mohan, and M. P. Kothiyal, Time average vibration analysis using Hilbert transformation, Appl. Opt. 49, pp. 5777-5786, 2010.

80. Lai, S., B. King, and M. A. Neifeld, Wave front reconstruction by means of phase-shifting digital in-line holography, Opt. Commun. 173, pp.155-160, 2000.

81. Larkin, K. G., D. J. Bone, and M. A. Oldfield, Natural demodulation of two-dimensional fringe patterns. I. General background of the spiral phase quadrature transform, J. Opt. Soc. Am. A 18, pp. 1862 – 1870, 2001.

82. Larkin, K. G., Natural demodulation of two-dimensional fringe patterns. II. Stationary phase analysis of the spiral phase quadrature transform, J. Opt. Soc. America. A 18, pp. 1871 – 1881, 2001.

83. Latychevskaia, T. and H. W. Fink, Solution to the twin image problem in holography, Phys. Rev. Lett. 98, pp.233901(1)-233901(4), 2007.

84. Leendertz, J. A. and J. N. Butters, An Image-Shearing Speckle Pattern Interferometer for Measuring Bending Moments, J. Phys. E Scientific Instr. 6, pp.1107-1110, 1973.

85. Leith, E. N. and J. Upatnieks, Reconstructed wavefronts and communication theory, J. Opt. Soc. Am. 52, pp.1123-1130, 1962.

86. Leith, E. N. and J. Upatnieks, Wavefront reconstruction with continuous-tone objects, J. Opt. Soc. Am. 53, pp.1377-1381, 1963.

87. Liu, C., Z. Liu, F. Bo, Y. Wang, and J. Zhu, Super-resolution digital holographic imaging method, Appl. Phys. Lett. 81, pp.3143-3145, 2002.

88. Liu, C., Simultaneous measurement of displacement and its spatial derivatives with a digital holographic method, Opt. Eng. 42, pp.3443-3446, 2003.

89. Liu, G. and P. D. Scott, Phase retrieval and twin-image elimination for in-line Fresnel holograms, J. Opt. Soc. Am. A 4, pp.159-165, 1987.

90. Liu, Y. J., B. Chen, E. R. Li, J. Y. Wang, A. Marcelli, S. W. Wilkins, H. Ming, Y. C. Tian, K. A. Nugent, P. P. Zhu, and Z. Y. Wu, Phase retrieval in x-ray imaging based on using structured illumination, Phys. Rev. A 78, pp.023817(1)- 023817(5), 2008.

91. Løkberg, O., Electronic speckle pattern interferometry, Phys. Technol. 11, pp.16-22, 1980.

92. Løkberg, O., ESPI—the ultimate holographic tool for vibration analysis? J. Acoust. Soc. Am. 75, pp. 1783–1791, 1984.

93. Lyons, R. G., Understanding Digital Signal Processing, Prentice Hall PTR: Upper Saddle River, NJ, USA, 2001.

94. Ma, J., Z. Wang, B. Pan, T. Hoang, M. Vo, and L. Luu, kaji, Appl. Opt. 50, pp. 2425-2430, 2011.

95. Malacara, D., M. Servin, and Z. Malacara, Interferogram Analysis for Optical Testing, New York, Marcel Dekker, 1998.

96. Malacara D., Optical shop testing, New Jersey, John Wiley & Sons, 2007.

97. Maragos, P., J.F. Kaiser and T.F. Quatieri, Energy Separation in Signal Modulations with Application to Speech Analysis, IEEE trans. Sign. Procs. 41, pp. 3024-3051, 1993.

98. Marklund, O., Robust fringe density and direction estimation in noisy phase maps, J. Opt. Soc. Am. A 18, pp.2717-2727, 2001.

99. Marroquin, J. L., R. R. Vera, and M. Servin, Local phase from local orientation by solution of a sequence of linear systems, J. Opt. Soc. Am. A 15, pp.1536-1544, 1998.

100. Miao, J., D. Sayre, and H. N. Chapman, Phase retrieval from the magnitude of the Fourier transforms of nonperiodic objects, J. Opt. Soc. Am. A 15, pp.1662-1669, 1998.

101. Micó, V., J. García, Z. Zalevsky, and B. Javidi, Phase-shifting Gabor holography, Opt. Lett. 34, pp.1492-1494, 2009.

102. Molin, N. E., Optical methods for acoustics and vibration measurements, in Handbook of Acoustics, (Ed. T. Rossing) New York, Springer, pp. 1101–1123, 2007.

103. Moore, A. J. and F. M. Santoyo, Phase demodulation in the space domain without a fringe carrier, Opt. Lasers Eng. 23, pp.319-330, 1995.

104. Nakadate, S., T. Yatagai, and H. Saito, Digital speckle-pattern shearing interferometry, Appl. Opt. 19, pp. 4241-4246, 1980.

105. Nakadate, S., Vibration measurement using phase-shifting time-average holographic interferometry, Appl. Opt. 25, pp. 4162-4167, 1986.

106. Nakajima, N., Phase retrieval using the logarithmic Hilbert transform and the Fourier series expansion, JOSA A 5, pp. 257-262, 1988.

107. Novak M., J. Millerd, N. Brock, M. North-Morris, J. Hayes, and J. C. Wyant, Analysis of a micropolarizer array-based simultaneous phase-shifting interferometer, Appl. Opt. 44, pp. 6861-6868, 2005.

108. Ozaktas, H. M., Z. Zalevsky, and M. A. Kutay, The fractional Fourier transform with applications in optics and signal processing, Singapore, Wiley, 2001.

109. Pan, B., K. Qian, H. Xie, and A. Asundi, Two-dimensional digital image correlation for in-plane displacement and strain measurement: a review, Meas. Sci. Technol. 20, pp.062001(1)-062001(17), 2009.

110. Pan, B., A. Asundi, H. Xie, and J. Gao, Digital image correlation using iterative least squares and pointwise least squares for displacement field and strain field measurements, Opt. Lasers Eng. 47, pp.865-874, 2009.

111. Pedrini, G., I. Alexeenko, W. Osten, and H. J. Tiziani, Temporal phase unwrapping of digital hologram sequences, Appl. Opt. 42, pp.5846-5854, 2003.

112. Pedrini, G., W. Osten, and M. E. Gusev, High-speed digital holographic interferometry for vibration measurement, Appl. Opt. 45, pp.3456-3462, 2006.

113. Pryputniewicz, R. J., and K. A. Stetson, Measurement of vibration pattern using electro-optic holography, Proc. SPIE 1162, pp. 456–468, 1989.

114. Qian, K., S. H.,Soon, and A. Asundi, Phase-shifting windowed Fourier ridges for determination of phase derivatives, Opt. Lett. 28, pp. 1657-1659, 2003.

115. Qian, K., Windowed Fourier transform for fringe pattern analysis, Appl. Opt. 43, pp.2695-2702, 2004.

116. Qian, K. and S. H. Soon, Two-dimensional windowed Fourier frames for noise reduction in fringe pattern analysis, Opt. Eng. 44, pp.075601-075609, 2005.

117. Qian, K., Two-dimensional windowed Fourier transform for fringe pattern analysis: principles, applications and implementations, Opt. Lasers Eng. 45, pp.304-317, 2007.

118. Quan, C., C. J. Tay, X. Kang, X. Y. He, and H. M. Shang, Shape measurement by use of liquid-crystal display fringe projection with two-step phase shifting, Appl. Opt. 42, pp.2329-2335, 2003.

119. Quan, C., C. J. Tay, and L. Chen, Fringe-density estimation by continuous wavelet transform, Appl. Opt. 44, pp.2359-2365, 2005.

120. Quan, C., C. J. Tay, F. Yang, and X. He, Phase extraction from a single fringe pattern based on guidance of an extreme map, Appl. Opt., 44, pp. 4814-4821, 2005.

121. Quan, C., C. J. Tay, and H. Chen, Temporal phase retrieval from a complex field in digital holographic interferometry, Opt. Lett. 32, pp.1602-1604, 2007.

122. Quan, C., C. J. Tay, and W. Chen, Determination of displacement derivative in digital holographic interferometry, Opt. Commun., 282, pp. 809–815, 2009.

123. Quan, C., H. Niu, and C. J. Tay, An improved windowed Fourier transform for fringe demodulation, Opt. Laser Technol. 42, pp. 126- 131, 2010.

124. Rajshekhar, G., Gorthi, S. S., and P. Rastogi, Adaptive window Wigner-Ville-distribution-based method to estimate phase derivative from optical fringes, Opt. Lett. 34, pp. 3151-3153, 2009.

125. Rajshekhar, G., and P. Rastogi, Application of complex-lag distributions for estimation of arbitrary order phase derivatives in digital holographic interferometry, Opt. Lett. 36, pp. 3738-3740, 2011.

126. Rastogi, P. K., Measurement of curvature and twist of a deformed object by electronic speckle-shearing pattern interferometry, Opt. Lett. 21, pp. 905-907, 1996.

127. Rastogi, P. K., Digital speckle pattern interferometry and related techniques, Chichester, John Wiley & Sons, 2001.

128. Rastogi, P. K., Digital Optical Measurement Techniques and Applications, Artech House, 2015.

129. Robinson, D. W., Phase unwrapping methods, in Interferogram Analysis: Digital Fringe Pattern Measurement Techniques, (Ed. D. W. Robinson, G. T. Reid), Bristol, Institute of Physics, pp. 194–229, 1993.

130. Rowe, S. H. and W. T. Welford, Surface topography of non-optical surfaces by projected interference fringes, Nature (London) 216, pp.786-787, 1967.

131. Samala, P., F. Wright, K. W. Long, and L. X. Yang, Determination of Whole Field Residual Strain Using 3D-DSPI and Increments Hole Drilling, J. Mater. Manuf. - SAE 2006 Trans., pp.624 – 628, 2006.

132. Schnars, U. and W. Jüptner, Direct recording of holograms by a CCD target and numerical reconstruction, Appl. Opt. 33, pp.179-181, 1994.

133. Schnars, U. and W. Jueptner, Digital holography: digital hologram recording, numerical reconstruction, and related techniques, Berlin, Springer, 2005.

134. Schwider, J., R. Burrow, K. E. Elssner, J. Grzanna, R. Spolaczyk, and K. Merkel, Digital wave-front measuring interferometry: some systematic error sources, Appl. Opt., 22. pp. 3421-3432. 1983.

135. Sciammarella, C. A., and T. Kim, Determination of strains from fringe patterns using space-frequency representations, Opt. Eng. 42, pp. 3182–3193, 2003.

136. Sciammarella, C. A., and T. Kim, Frequency modulation interpretation of fringes and computation of strains, Exp. Mech. 45, pp. 393–403, 2005.

137. Servin, M., J. L. Marroquin, and F. J. Cuevas, Demodulation of a single interferogram by use of a two-dimensional regularized phase-tracking technique, Appl. Opt. 36, pp. 4540-4548, 1997.

138. Servin, M., J. L. Marroquin, D. Malacara, and F. J. Cuevas, Phase unwrapping with a regularized phase-tracking system, Appl. Opt. 37, pp.1917-1923, 1998.

139. Servin, M., J. L. Marroquin, and F. J. Cuevas, Fringe-follower regularized phase tracker for demodulation of closed-fringe interferograms, J. Opt. Soc. Am A 18, pp. 689-695, 2001.

140. Shaked, N. T., Y. Zhu, M. T. Rinehart, and A. Wax, Two-step-only phase-shifting interferometry with optimized detector bandwidth for microscopy of live cells, Opt. Express 17, pp.15585-15591, 2009.

141. Shakher, C., R. Kumar, S. K. Singh, and S. A. Kazmi, Application of wavelet filtering for vibration analysis using digital speckle pattern interferometry, Opt. Eng. 41, pp. 176 – 180, 2002.

142. Sharma, A., G. Sheoran, Z. A. Jaffery, and Moinuddin, Improvement of signal-to-noise ratio in digital holography using wavelet transform, Opt. Lasers Eng. 46, pp. 42 – 47, 2008.

143. Sharpe, Jr. W. N., Springer handbook of experimental solid mechanics, Springer, 2008.

144. Shinpaugh, K. A., R. L. Simpon, A. L. Wicks, S. M. Ha, and J. L. Fleming, Signal-processing techniques for low signal-to-noise ratio laser Doppler velocimetry signals, Exps. in Fluids 12, pp. 319-328, 1992.

145. Soedel, W., Vibrations of Shells and Plates, 3rd ed., Marcel Dekker Inc., 2004.

146. Steinchen, W., G. Kupfer, P. Mackel, and F. Vossing, Determination of strain distribution by means of digital shearography, Measurement 26, pp. 79-90, 1999.

147. Steinchen, W., and L. Yang, Digital shearography: theory and application of digital speckle pattern shearing interferometry, Bellingham, SPIE press, 2003.

148. Stephenson, P., D. R. Burton, and M. J. Lalor, Data validation techniques in a tiled phase unwrapping algorithm, Opt. Eng. 33, pp.3703-3708, 1994.

149. Ströbel, B., Processing of interferometric phase maps as complex-valued phasor images, Appl. Opt. 35, pp.2192-2198, 1996.

150. Sucerquia, J. G., W. Xu, S. K. Jericho, P. Klages, M. H. Jericho, and H. J. Kreuzer, Digital in-line holographic microscopy, Appl. Opt. 45, pp.836-850, 2006.

151. Sucerquia, J. G., W. Xu, M. H. Jericho, and H. J. Kreuzer, Immersion digital in-line holographic microscopy, Opt. Lett. 31, pp.1211-1213, 2006.

152. Takeda, M., H. Ina, and S. Kobayashi, Fourier-transform method of fringe-pattern analysis for computer-based topography and interferometry, J. Opt. Soc. Am. 72, pp.156-160, 1982.

153. Takeda, M. and K. Mutoh, Fourier transform profilometry for the automatic measurement of 3-D object shapes, Appl. Opt. 22, pp.3977-3982, 1983.

154. Takeda, M., Spatial-carrier fringe-pattern analysis and its applications to precision interferometry and profilometry: an overview, Ind. Metrol. 1, pp.79-99, 1990.

155. Tasgetiren, M. F., P.N. Suganthan, and Q.K. Pan, An ensemble of discrete differential evolution algorithms for solving the generalized traveling salesman problem, Appl. Math. Comp. 215, pp. 3356–3368, 2010.

156. Tay, C. J., S. L. Toh, H. M. Shang and Q. Y. Lin, Direct determination of second-order derivatives in plate bending using multiple-exposure shearography, Opt. Laser Technol. 26, pp. 91-98, 1994.

157. Tay, C. J., C. Quan, and L. Chen, Phase retrieval with a three-frame phase-shifting algorithm with an unknown phase shift, Appl. Opt. 44, pp.1401-1409, 2005.

158. Tay, C. J., and Y. Fu, Determination of curvature and twist by digital shearography and wavelet transforms, Opt. Lett. 30, pp. 2873-2875, 2005.

159. Tay, C. J., C. Quan, W. Sun, and X. Y. He, Demodulation of a single interferogram based on continuous wavelet transform and phase derivative, Opt. Commun. 280, pp. 327-336, 2007.

160. Tian, C., Y. Yang, D. Liu, Y. Luo, and Y. Zhuo, Demodulation of a single complex fringe interferogram with a path-independent regularized phase-tracking technique, Appl. Opt. 49, pp. 170-179, 2010.

161. Timoshenko, S. P., and S. Woinowsky-Krieger, Theory of Plates and Shells, 2nd ed., pp. 63–72, New York, McGraw-Hill, 1959.

162. Trusiak, M., M. Wielgus, and K. Patorski, Advanced processing of optical fringe patterns by automated selective reconstruction and enhanced fast empirical mode decomposition, Opt. Lasers Eng. 52, pp. 230-240, 2014.

163. Vikhagen, E., TV holography: spatial resolution and signal resolution in deformation analysis, Appl. Opt. 30, pp.420-425, 1991.

164. Wagner, C., S. Seebacher, W. Osten, and W. Jüptner, Digital recording and numerical reconstruction of lensless Fourier holograms in optical metrology, Appl. Opt. 38, pp.4812-4820, 1999.

165. Wang, J. and I. Grant, Electronic speckle interferometry, phase-mapping, and nondestructive testing techniques applied to real-time, thermal loading, Appl. Opt. 34, pp.3620-3627, 1995.

166. Wang, J. and A. Asundi, Strain contouring with Gabor filters: filter bank design, Appl. Opt. 41, pp.7229-7236, 2002.

167. Wang, Y., X. Gao, X. Xie, S. Wu, Y. Liu, and L. Yang, "Simultaneous dual directional strain measurement using spatial phase-shift digital shearography," Opt. Laser Eng. doi:10.1016/j.optlaseng.2015.12.009, (in press) 2016.

168. Watkins, L. R., S. M. Tan, and T. H. Barnes, Determination of interferometer phase distributions by use of wavelets, Opt. Lett. 24, pp.905-907, 1999.

169. Wong, W. O., K. T. Chan, and T. P. Leung, Contrast and sensitivity of the vibration fringes in time-averaged electronic speckle pattern interferometry: effect of variations of force level, Opt. Laser Technol. 29, pp. 179-185, 1997.

170. Wong, W. O., K. T. Chan, and T. P. Leung, Quantitative vibration amplitude measurement with time-averaged digital speckle pattern interferometry, Opt. Laser Technol. 30, pp. 317-324, 1998.

171. Xie, X., N. Xu, J. Suna, Y. Wang, and L. Yang, Simultaneous measurement of deformation and the first derivative with spatial phase-shift digital shearography, Opt. Commun. 286, pp. 277- 281, 2013.

172. Xu, W., M. H. Jericho, I. A. Meinertzhagen, and H. J. Kreuzer, Digital in-line holography of microspheres, Appl. Opt. 41, pp.5367-5375, 2002.

173. Xu, W., M. H. Jericho, H. J. Kreuzer, and I. A. Meinertzhagen, Tracking particles in four dimensions with in-line holographic microscopy, Opt. Lett. 28, pp.164-166, 2003.

174. Yamaguchi, I. and T. Zhang, Phase-shifting digital holography, Opt. Lett. 22, pp.1268-1270, 1997.

175. Yamaguchi, I., J. Kato, S. Ohta, and J. Mizuno, Image formation in phase-shifting digital holography and applications to microscopy, Appl. Opt. 40, pp.6177-6186, 2001.

176. Yamaguchi, I., J. I. Kato, and H. Matsuzaki, Measurement of surface shape and deformation by phase-shifting image digital holography, Opt. Eng. 42, pp.1267-1271, 2003.

177. Yamaguchi, I., T. Ida, M. Yokota, and K. Yamashita, Surface shape measurement by phase-shifting digital holography with a wavelength shift, Appl. Opt. 45, pp.7610-7616, 2006.

178. Yang, L. X., and A. Ettemeyer, Strain measurement by 3D-Electronic Speckle Pattern Interferometry: Potentials, Limitation and Applications, Opt. Eng. 42, pp. 1257 – 1266, 2003.

179. Yang, L. X., and Y. Y. Hung, Digital shearography for nondestructive evaluation and application in automotive and aerospace industries, J. Holo. Speck. 1, pp. 69-79, 2004.

180. Yang L. X., Recent Developments of Digital Shearography for NDT, Mater. Eval. 64, pp. 703 – 709, 2006.

181. Yang, L. X., P. Zhang, S. Liu, P.R. Samala, M. Su, and H. Yokota, Measurement of Strain Distributions in Mouse Femora with 3D-Digital Speckle Pattern Interferometry, Opt. Lasers Eng. 45, pp. 843 – 851, 2007.

182. Yang, L. X., M. Schuth, D. Thomas, Y.H. Wang, and F. Voessing, Stroboscopic Digital Speckle Pattern Interferometry for Vibration Analysis of Microsystem, Opt. Lasers Eng. 47, pp. 252 – 258, 2009.

183. Yang, L. X., X. Xie, L. Zhu, S. Wu, and Y. Wang, Review of electronic speckle pattern interferometry (ESPI) for three dimensional displacement measurement, Chin. Journ. Mech. Eng. 27, pp. 1-13, 2014.

184. Yang, X., Q. Yu, and S. Fu, Combined method for obtaining fringe orientations of ESPI, Opt. Commun. 273, pp. 60-66, 2007.

185. Yang, X., Q. Yu, S. Fu, An algorithm for estimating both fringe orientation and fringe density, Opt. Commun. 274, pp. 286-292, 2007.

186. Yang, X., Q. Yu, and S. Fu, Determination of skeleton and sign map for phase obtaining from a single ESPI image, Opt. Commun. 282, pp. 2301–2306, 2009.

187. Yang, X., X. Sun, Q. Yu, and S. Fu, Direct ESPI phase estimating from only two interferograms, Opt. Commun. 290, pp. 63-68, 2012.

188. Zhang, Y., Q. Lü, and B. Ge, Elimination of zero-order diffraction in digital off-axis holography, Opt. Commun. 240, pp.261-267, 2004.

189. Zhong, J. and J. Weng, Dilating gabor transform for the fringe analysis of 3-d shape measurement, Opt. Eng. 43, pp. 895–899, 2004.

190. Zhong, J. and H. Zeng, Multiscale windowed Fourier transform for phase extraction of fringe patterns, Appl. Opt. 46, pp.2670-2675, 2007.

191. Zhou, S., and Z. Sun, Using ensemble method to improve the performance of genetic algorithm, Proc. CIS 2005, LNAI 3801, pp. 255 – 260, 2005.

192. Zhu Y. K., G.Y. Tian, R.S. Lu and K. Zhang, A review of optical NDT technologies, Sensors 11, pp. 7773-7798, 2011.

193. Zou, J. M., I. Vartanyants, M. Gao, R. Zhang, and L. A. Nagahara, Atomic resolution imaging of a carbon nanotube from diffraction intensities, Science 300, pp.1419-1421, 2003.

APPENDIX

LIST OF PUBLICATIONS DURING PH.D. PERIOD

Journal papers

1. **B. Deepan**, C. Quan, Y. Wang, and C. J. Tay, Multiple-image encryption by space multiplexing based on compressive sensing and the double-random phase-encoding technique, Applied Optics, 53, pp.4539-4547, 2014.

2. **B. Deepan**, C. Quan, and C. J. Tay, Determination of phase derivatives from a single fringe pattern using Teager Hilbert Huang transform, Optics Communications, 359, pp.162-170, 2016.

3. **B. Deepan**, C. Quan, and C. J. Tay, A derivative based simplified phase tracker for a single fringe pattern demodulation, Optics and Lasers in Engineering, 83, pp.83-89, 2016.

4. **B. Deepan**, C. Quan, and C. J. Tay, Determination of slope, curvature, and twist from a single shearography fringe pattern using derivative-based regularized phase tracker, Optical Engineering, 55, pp. 121707(1)-121707(6), 2016.

5. **B. Deepan**, C. Quan, and C. J. Tay, Quantitative vibration analysis using a single fringe pattern in time-average speckle interferometry, Applied Optics, 55, pp.5876-5883, 2016.

Conference papers

6. **B. Deepan**, C. Quan, and C. J. Tay, Ensemble of hybrid genetic algorithm for two-dimensional phase unwrapping, International Conference on Optics in Precision Engineering and Nanotechnology (icOPEN2013). International Society for Optics and Photonics, pp. 87691N-87691N, 2013.

7. C. Quan, **B. Deepan,** W. Chen, and C. J. Tay, Phase retrieval and phase derivative determination in digital holography, Advancement of Optical Methods in Experimental Mechanics, Volume 3. Springer International Publishing, pp. 241-250, 2014.

8. **B. Deepan,** C. Quan, and C. J. Tay, Compressive sensing for digital holographic interferometry, International Conference on Experimental Mechanics 2013 and the Twelfth Asian Conference on Experimental Mechanics, International Society for Optics and Photonics, pp. 923419-923419, 2014.

9. **B. Deepan**, C. Quan, and C. J. Tay, Phase retrieval using compressive sensing in digital holographic interferometry, 16th International Conference on Experimental Mechanics (ICEM16), July 7-11, 2014, Cambridge, UK.

10. **B. Deepan**, C. Quan, and C. J. Tay, Phase retrieval from a single fringe pattern using Teager-Hilbert-Huang transform, International Conference on Experimental Mechanics 2014, International Society for Optics and Photonics, pp. 93020Q-93020Q, 2015.

11. **B. Deepan,** C. Quan, and C. J. Tay, Estimation of phase derivatives in digital holographic interferometry using discrete higher order image demodulation algorithm (DHODA), International Conference on Optics in Precision Engineering and Nanotechnology (icOPEN2015). International Society for Optics and Photonics, April 14-16, 2015, Singapore.

12. **B. Deepan**, C. Quan, and C. J. Tay, A novel method for mode shape visualization and amplitude measurement of vibration using time average electronic speckle pattern interferometry, SEM XIII International Congress and Exposition on Experimental and Applied Mechanics, June 6-9, 2016, Orlando, USA.

13. C. Quan, **B. Deepan**, and C. J. Tay, Displacement and its derivatives measurement from a single fringe pattern in coherent optical techniques, The 6th International Conference on Manipulation, Manufacturing and Measurement on the Nanoscale, July 18 – 22, 2016, Chongqing, China.